

**EXPERIMENTAL STUDIES OF SOLID-STATE
REACTIONS IN NANOSCALE SYSTEMS**

by

Brian G. Kelly

A dissertation submitted to the Faculty of the University of Delaware in partial fulfillment of the requirements for the degree of Doctor of Philosophy in Physics

Summer 2016

© 2016 Brian G. Kelly
All Rights Reserved

ProQuest Number: 10191710

All rights reserved

INFORMATION TO ALL USERS

The quality of this reproduction is dependent upon the quality of the copy submitted.

In the unlikely event that the author did not send a complete manuscript and there are missing pages, these will be noted. Also, if material had to be removed, a note will indicate the deletion.



ProQuest 10191710

Published by ProQuest LLC (2016). Copyright of the Dissertation is held by the Author.

All rights reserved.

This work is protected against unauthorized copying under Title 17, United States Code
Microform Edition © ProQuest LLC.

ProQuest LLC.
789 East Eisenhower Parkway
P.O. Box 1346
Ann Arbor, MI 48106 - 1346

**EXPERIMENTAL STUDIES OF SOLID-STATE
REACTIONS IN NANOSCALE SYSTEMS**

by

Brian G. Kelly

Approved: _____
Edmund R. Nowak, Ph.D.
Chair of the Department of Physics and Astronomy

Approved: _____
George H. Watson, Ph.D.
Dean of the College of Arts and Sciences

Approved: _____
Ann L. Ardis, Ph.D.
Senior Vice Provost for Graduate and Professional Education

I certify that I have read this dissertation and that in my opinion it meets the academic and professional standard required by the University as a dissertation for the degree of Doctor of Philosophy.

Signed:

Karl M. Unruh, Ph.D.
Professor in charge of dissertation

I certify that I have read this dissertation and that in my opinion it meets the academic and professional standard required by the University as a dissertation for the degree of Doctor of Philosophy.

Signed:

Matthew F. DeCamp, Ph.D.
Member of dissertation committee

I certify that I have read this dissertation and that in my opinion it meets the academic and professional standard required by the University as a dissertation for the degree of Doctor of Philosophy.

Signed:

Edmund R. Nowak, Ph.D.
Member of dissertation committee

I certify that I have read this dissertation and that in my opinion it meets the academic and professional standard required by the University as a dissertation for the degree of Doctor of Philosophy.

Signed:

Timothy Mueller, Ph.D.
Member of dissertation committee

ACKNOWLEDGMENTS

This thesis and the education behind it has been an incredible and long journey, and it would have not been possible without the help and support of many people I will forever be grateful for.

First and foremost, I would have neither started nor completed my work at the University of Delaware without the support of my parents, Brian and Kathy, or my sisters, Amanda and Mary Kate. I owe them the curiosity, motivation, and dedication that brought me to graduate school and allowed me to complete it. I'd also like to thank my extended family for the support and kindness I needed so often and they willingly and repeatedly provided in my time here.

I'd like to thank the many teachers that led me down the path to study Physics. From my first class with Dan DeForest at Burr and Burton Academy, to the entire faculty of the Physics department at Drew University, I would not have continued in this field were it not for the enthusiasm of those who taught me. I'd like to especially thank Dr. Robert Fenstermacher for teaching me what it meant to study Physics, and Dr. David McGee for my first experience working in a research laboratory.

I'd like to thank Dr. Karl Unruh for advising me for six and a half years. His guidance and patience were responsible for any competence I gained as a researcher in my time at the University of Delaware, and I'll always be grateful for his support. I'd also like to recognize the rest of my committee, Dr. Timothy Mueller, Dr. Edmund Nowak, and especially Dr. Matthew DeCamp, who I'm grateful to have collaborated with for the last few years.

I'd like to recognize all the staff of the Department of Physics and Astronomy, especially Robert Schmidt, Tom Reid, Tom Reilly, and Derrick Allen, as well as Gerald Poirier. Their knowledge and helpfulness cannot be overstated, and without them I, like most graduate students, would have been hopelessly lost.

It is impossible to list all the colleagues I should thank, but I would like to offer special thanks to the other 2009 Drew University Physics majors, Todd Navarre and Kyle Nugent, as well as the students before and after us who we shared the undergraduate experience with. I'd like to thank fellow Drew and UDel alumni Evan Kimberly and Dr. Laura Vanderhoef, who helped me bridge the gap between my undergraduate and graduate education. I'd like to thank Dr. Seth Meiselman, Kevin Haughey, and Jamy Moreno for study groups and staying up late, Dr. Ryan Stearrett and Paul Parsons for getting up early, everyone I shared a lab with for mitigating my hermit tendencies, and all the graduate students in the Physics Department who kept me sane. I hope to thank everyone who has been so important to me in person, and to never forget how much I owe to those around me.

Finally, I'd like to thank the DPA, the DOE ARPA-E program, the NSF, the APS at Argonne National Lab, and the NIH, who funded my studies and research.

TABLE OF CONTENTS

LIST OF TABLES	ix
LIST OF FIGURES	x
ABSTRACT	xvi

Chapter

1	INTRODUCTION	1
2	THEORETICAL BACKGROUND	5
2.1	Diffusion	5
2.1.1	Fick's First Law	6
2.1.2	Fick's Second Law	6
2.1.3	Expanding Fick's Laws to the Nanoscale	8
2.2	Size dependence of the lattice parameter	8
2.3	Periodic Composition effects in XRD	9
2.3.1	Low Angle Signals	9
2.3.2	Diffraction around the Bragg angle	10
2.4	Activation Energies	12
2.4.1	Extracting activation energies from isothermal measurements ...	12
3	EXPERIMENTAL TECHNIQUES	14
3.1	X-Ray Diffraction	14
3.1.1	Lattice Structure	14
3.1.2	Measurement Geometries	15
3.1.3	Peak shape effects	18
3.1.3.1	Temperature	19
3.1.3.2	Finite Size	19
3.1.4	Scherrer Analysis	20
3.1.5	Analysis Software	20
3.2	Thermogravimetric Analysis	21
3.2.1	Analyzing Isothermal Measurements	21

3.2.2	Properly performing DSC/TGA measurements	23
3.2.3	Temperature Corrections	24
3.3	Pt and Pt/Ni Particle Preparation	30
3.3.1	Seed Solution	30
3.3.2	Pt Cluster Synthesis	30
3.3.3	Ni addition to Pt clusters	32
3.4	As-Prepared Particles	32
3.4.1	Pt Clusters	33
3.4.2	Ni/Pt Nanocomposites	35
3.4.3	Pump-probe sample preparation	38
4	THE REDUCTION OF SAMARIUM AND COBALT OXIDES TO METALLIC SAMARIUM COBALT ALLOYS	49
4.1	Synthesis	49
4.1.1	Autocombustion	49
4.1.2	Calcination	50
4.2	Reduction	52
4.2.1	Reduction Pathway	52
4.2.2	Reduction Environments	53
4.2.3	Sample Sizes	54
4.3	TGA Measurements	55
4.3.1	Co ₃ O ₄ measurements	55
4.3.2	SmCoO ₃ measurements	61
4.3.2.1	SmCoO ₃ to Sm ₂ O ₃ +CoO	61
4.3.2.2	CoO to Co in the presence of Sm ₂ O ₃	66
5	INTER-GRAIN DIFFUSION IN PT AND PT/NI PARTICLES	74
5.1	Pt Sintering Measurements	74
5.1.1	Conventional Thermal Measurements	76
5.1.1.1	Experimental Conditions	77
5.1.1.2	Results	79

5.1.2	Laser-driven Sintering Measurements.....	84
5.1.2.1	Sample Preparation and Measurement Parameters	85
5.1.2.2	Results	87
5.1.2.3	Discussion.....	94
5.1.2.4	Lattice Parameter Changes in Air.....	96
5.2	Multilayer Ni/Pt diffusion	100
6	DIRECTIONS FOR CONTINUED WORK	105
	REFERENCES	107

LIST OF TABLES

Table 3.1:	Stated mass variation tolerances during DSC/TGA measurements under temperature ramps and room temperature changes. These values were provided by Matthew Reader at TA instruments.....	23
------------	--	----

LIST OF FIGURES

Figure 3.1: The two laboratory XRD geometries used in this work were a symmetric θ - 2θ geometry (a) and a grazing incidence geometry (b)......	16
Figure 3.2: Fixed source (pump-probe) scattering geometry. An area detector collects scattered photons over a large solid angle (angular resolution and range is set by the distance from the sample to the detector).	17
Figure 3.3: Sample output of an XRD spectrum collected by an area detector. This is a powder Pt sample, and the (111), (200), and (220) peaks are visible.	18
Figure 3.4: As-measured mass of a 10mg alumina sample during a series of isotherms from 100°C to 350°C.	25
Figure 3.5: Sample masses for each of the isotherms. Measurements were made in 50°C increments. Case temperature variations 0.5°C or greater were observed for each 10h isotherm.....	26
Figure 3.6: Case temperature dependence of the mass at each measurement isotherm. Error bars for each fit are smaller than the symbols.....	27
Figure 3.7: The mass offset of fits at each isothermal temperature. These offsets have been fit to a second order polynomial to quantify mass changes due to sample temperature. Changes in mass are plotted as a difference from the 100°C isotherm mass measurement to make the graph clear.	28
Figure 3.8: The as-measured and corrected mass data. The corrected data shows variations an order of magnitude smaller than the uncorrected.	29
Figure 3.9: A typical heating profile for 30nm Pt cluster synthesis. More rapid heating produced smaller clusters, although individual Pt grain sizes were independent of heating rate.....	31
Figure 3.10: As-prepared clusters of Pt nanoparticles. The presence of a large number of isolated Pt clusters suggests agglomeration of some clusters happened during drying, not in solution.....	33
Figure 3.11: Dynamic Light Scattering (DLS) measurements of as-prepared Pt particle sizes before (blue) and after (red) washing in water.	34
Figure 3.12: X-ray diffraction of as-prepared Pt nanoparticles.	35

Figure 3.13: As-prepared Pt/Ni nanoparticles. The Pt is in the fcc phase, while the Ni is hcp.....	36
Figure 3.14: Dark field (left) and bright field images of Pt clusters coated with Ni. Dark field images show much larger aligned domains in Pt clusters than the initial 5nm grains. Bright field imaging clearly shows Ni present between at least some Pt clusters.....	37
Figure 3.15: A monolayer of Pt nanoparticles at a water-oil interface. A glass crystalizing dish was used for this picture rather than the Teflon trough to make the effect easier to see.	39
Figure 3.16: Pt on a glass slide in the Teflon trough. The slide was dried in the trough for several hours before removing.	40
Figure 3.17: Optical microscope image of a Pt particle thin film.....	41
Figure 3.18: A sample used for AFM measurement. The clear areas in the middle were cleaned by scraping with a razor, and provided excellent contrast for film thickness measurements.....	42
Figure 3.19: A topological map of an as-prepared film of Pt nanoparticles. Black spaces signify no Pt coverage. A gap in coverage is circled in white.	43
Figure 3.20: AFM measured heights of a sample slide. The two peaks are the surface of the slide (narrow) and the surface of the Pt film (broad), while thicknesses are measured relative to the glass surface.	44
Figure 3.21: An example of testing for the concentration of Pt remaining in solution after making a “monolayer” film. Measurements were made at the initial concentration (black), 1/2, 1/4, 1/8, 1/16, and 1/32 (pink) concentrations. The dotted lines mark “slices” at the wavelengths used for the subsequent Pt concentration measurements.....	45
Figure 3.22: The absorption at 500, 550, 600, and 650nm of the remaining Pt solution after making a film using 7.5mL of ethanol.....	46
Figure 3.23: The measured ethanol dependence of the amount of Pt removed from the solution during the film-making process. Error bars are smaller than the symbols.....	47

Figure 4.1: Sm-Co-O oxide precursor, as-combusted and following a 2 hour calcination at 550°C and 750°C. The initial phase was dominated by Co ₃ O ₄ with some evidence of crystalline SmCoO ₃ , while the final phase contained only the two oxides. Reference peak position sticks are provided for the most intense peaks of each phase.	51
Figure 4.2: Molar ratio Sm:Co 2:17 precursor oxide, before (left) and after (right) a 700°C/2h calcination step. There is no obvious separation of the SmCoO ₃ and Co ₃ O ₄ phases of the material.	52
Figure 4.3: Sample cups and paddles for DSC measurements	55
Figure 4.4: The heating profile for an example Co ₃ O ₄ conversion measurement with an isotherm of interest at 190°C. The initial 300°C isotherm was in N ₂ , while the subsequent 100°C, 190°C, and 350°C steps were in forming gas.	56
Figure 4.5: The mass evolution of a Co ₃ O ₄ sample undergoing the above 190°C measurement sequence.	57
Figure 4.6: Selected sample conversion data for the Co ₃ O ₄ to Co reaction. Isothermal temperatures of 185°C, 190°C, 195°C, 200°C, 220°C and 250°C are shown.	58
Figure 4.7: The Arrhenius plot for the 10%, 20%, 30% and 40% isoconversional slices.	59
Figure 4.8: A selection of activation energies calculated from these isoconversional measurements. The first three average to an activation energy of 1.04 eV/atom. Higher percentages of conversion combine effects due to both reactions.	60
Figure 4.9: The temperature profile for a 300°C isotherm. A preliminary 300°C cleaning isotherm was performed in N ₂ , while the sample was under forming gas for the second 300°C and the 330°C isotherms.	62
Figure 4.10: The mass evolution during the described temperature sequence. The initial isotherm contained irreversible mass loss due to the cleaning of contaminants, while intermediate and complete conversion were seen in the subsequent FG isotherms.	63
Figure 4.11: The amount of conversion during 10h isotherms at 240°C, 250°C, 260°C, 270°C, 280°C, and 300°C. Time t=0 was set as the time at which T _{sample} =T _{isotherm} following the ramp from room temperature.	64

Figure 4.12: The time required to convert 10% to 40% of the SmCoO_3 sample to $\text{Sm}_2\text{O}_3+\text{CoO}$ as a function of the isothermal temperature.....	65
Figure 4.13: The calculated activation energy from each isoconversional slice for the SmCoO_3 to $\text{Sm}_2\text{O}_3+\text{CoO}$ transition.	66
Figure 4.14: The temperature profile to obtain a 395°C isotherm. In this measurement, an intermediate isotherm was used to complete the SmCoO_3 conversion, and the isotherm of interest was the final portion of the experiment.....	67
Figure 4.15: The measured mass evolution during a 395°C measurement. This isotherm did not provide sufficient energy to complete the conversion. The rapid mass increase at the end was overwhelmingly due to instrumental effects, but could also signify some oxidation on cooling.	68
Figure 4.16: Conversion during the 350°C preparatory isotherm for each measurement. No systematic variation was seen or expected in this data.	69
Figure 4.17: Conversion during the ramp from 350°C to the isotherm of interest.....	70
Figure 4.18: Conversion during the 10 hour isotherms. The lack of complete conversion in the 410°C isotherm is likely due to a miscalculation of the initial mass. This miscalculation would be systematic for every isotherm.	71
Figure 4.19: Isoconversional data for 10% to 40% of the conversion of CoO to Co metal as a function of the isothermal temperature.	72
Figure 4.20: The measured activation energy for the CoO to Co reduction reaction in this system. For comparison, bulk activation energies for this system in forming gas are $0.477\text{-}0.607\text{eV/atom}$ [74].....	73
Figure 5.1: Appropriate types of experiment for sintering measurements determined by excitation and measurement time.	76
Figure 5.2: The reflux temperature of a water/ethylene glycol mixture by relative amounts of constituent liquids [75].	77
Figure 5.3: A sample comparison of XRD spectra. These patterns are the result of 10min sintering measurements at the indicated temperatures.	78

Figure 5.4: Scherrer sizes of Pt particles following 10 minute sintering measurements.	80
Figure 5.5: Lattice Parameter of Pt particles following 10 minute sintering measurements.	81
Figure 5.6: The time-dependence of Pt nanoparticle sizes annealed at 122°C.	82
Figure 5.7: The time-dependence of Pt nanoparticle lattice parameters annealed at 122°C.	83
Figure 5.8: The change in lattice parameter of conventionally sintered Pt particles vs the inverse Scherrer size. The change in lattice parameter is relative to the bulk value of 3.8242Å [76]	84
Figure 5.9: Schematic of Pt nanoparticles in a capillary tube used for hybrid measurements. Incident photons that were not scattered by the polycarbonate tubing were absorbed in the top layer of Pt particles, causing sintering. Other particles sintered by indirect heating.	86
Figure 5.10: Integrated XRD data for the Pt (111) peak of select 75mJ/cm ² runs with fits to a Pearson VII lineshape.	88
Figure 5.11: Lattice parameter evolution for Pt sintering measurements. The sample irradiated for the longest time at the highest fluence is pictured along with the energy-dependent data for the lower fluences. The size of the most-sintered sample was calculated to be approximately 30nm using the bulk lattice parameter relationship.	89
Figure 5.12: Scherrer calculated particle size for Pt sintering measurements. Although the results at each fluence are monotonic, they do not appear to follow a consistent functional form. Error bars are smaller than the symbols.	90
Figure 5.13: Lattice parameter vs particle size for laser-driven sintering measurements. The lattice parameter is clearly not solely a function of particle size, and there is no obvious functional dependence.	91
Figure 5.14: A summary of the size dependence of the Pt lattice parameter measured by conventional and hybrid techniques. In all cases, error bars are smaller than the data markers.	93
Figure 5.15: The magnitude of the change from the bulk lattice parameter as a function of the inverse particle size.	94

Figure 5.16: The lattice parameter evolution of monolayer Pt clusters under repeated excitation.....	96
Figure 5.17: The Scherrer size evolution of monolayer Pt clusters under repeated excitation.	97
Figure 5.18: The variation in measured lattice parameter for samples stored in air after being mixed with water or ethanol as a function of time since drying.....	98
Figure 5.19: The variation in sample size over the same interval as the previous figure.	99
Figure 5.20: A sample temperature profile for an exploratory XRD diffusion measurement. XRD spectra were collected during the isothermal portions.....	101
Figure 5.21: Low temperature XRD signals from the Pt-Ni multilayer system.	102
Figure 5.22: XRD signals from the Pt-Ni multilayer system around the Bragg peaks.....	103

ABSTRACT

This work focuses on the size-dependence of select physical properties in several nanoscale metallic and oxide systems, including lattice parameter and grain size evolution during diffusion and sintering processes in platinum nanoparticles and nanoscale platinum/nickel systems as well as the activation energies of the oxidation/reduction reactions required to produce nanoscale Sm-Co alloys from Sm-Co-O precursors.

The activation energies of the reduction/oxidation reactions required to produce metallic Sm-Co alloys from Sm-Co-O have been examined via thermogravimetric analysis (TGA). Precursor oxides were synthesized via an autocombustion process and characterized by X-ray diffraction (XRD) and scanning electron microscopy (SEM). TGA measurements determined the activation energy of the reduction of SmCoO_3 to a nanoscale mixture of $\text{Sm}_2\text{O}_3+\text{CoO}$ was 1.29eV/atom, and the activation energy of the subsequent conversion of CoO to metallic Co was 2.11eV/atom, several times larger than the bulk reported value. The activation energy of the conversion of Co_3O_4 to CoO was found to be 1.04eV/atom, and though the activation energy of the subsequent CoO to metallic Co in the absence of Sm_2O_3 could not be quantified, it was determined to be much smaller than 1.04eV/atom, and by extension much smaller than the 2.11eV/atom measured for the same transition in the presence of Sm_2O_3 .

In addition, an *in-situ* optical pump/x-ray probe technique was used to study the evolution in the size and lattice parameter of aggregated single crystal Pt nanoparticles prepared by a seed-growth method. The as-prepared Pt particles were

characterized by XRD and transmission electron microscopy (TEM). Photo-excitation of the as-prepared particles resulted in a monotonic particle growth and a rapid increase in lattice parameter that transitioned from monotonic at low incident laser fluence to non-monotonic at high incident laser fluence. As a result, the lattice parameter of the Pt nanoparticles did not evolve with a simple inverse grain size dependence. This result was compared to conventional sintering measurements in which a more typical size and lattice parameter evolution was observed.

Chapter 1

INTRODUCTION

The study of the effects of finite size effects in materials properties has yielded a large number of interesting and unforeseen results. Well-characterized properties of materials frequently change when these materials are studied at the nanoscale. Normally stable metals, for example, can become extremely reactive, metals known by a characteristic color can change that color or become black, even a property as basic as the melting temperature of the material can change. As a result, not only must synthesis methods to create these materials be developed, the properties of the materials themselves must often be re-characterized.

Nanomaterials are useful in a wide range of fields. Nanoparticles have extensive applications in medical research, including biological detection [1], drug delivery [2], intracellular labeling [3], magnetic resonance imaging (MRI) [4], and more [5, 6]. There are also a number of applications spanning energy storage [7], data storage [8-10], semiconductor technology [11] and in the field of permanent magnets [12]. Nanoparticles have also been used as the building blocks for complicated nanocomposite materials [13-15]. However, many of the applications of nanomaterials depend on properties that can be strongly size and shape dependent, and can depend on long range inter-particle interactions [16-18].

As a result, the research into nanoscale materials is focused not solely on the synthesis of these materials, but also on characterization of the mechanical and chemical properties of the product. Extensive research has been performed into the

control of size and shape during nanoparticle synthesis [19-22] and the study of how the properties of these nanoparticles change due to size and orientation effects [23-26]. This thesis represents an effort to expand the understanding of two specific nanomaterial systems: platinum-containing nanoparticles and samarium-cobalt oxides.

The samarium-cobalt system is of interest primarily for magnetic applications. As members of the family of rare-earth (RE) permanent magnets [27], the SmCo_5 and $\text{Sm}_2\text{Co}_{17}$ phases of this system are candidates for use in exchange-coupled permanent magnets [14, 28]. The SmCo_5 phase has one of the largest anisotropies found in a RE-Co magnetic phase [29], while the $\text{Sm}_2\text{Co}_{17}$ phase is used in high-temperature applications due to its high Curie temperature [30]. As a result, efforts have been made using a variety of methods to synthesize these phases in nanoparticle form while maintaining the favorable magnetic properties of the bulk alloys [31-35]. One such method is the direct reduction of a $\text{Co}_3\text{O}_4/\text{SmCoO}_3$ oxide, mixed on the nanoscale, to the desired metallic magnetic phase via calciothermic methods [36]. This method should allow a one-step synthesis of nanoparticle alloys, but the energetics of the reactions are not well understood.

In this work, the oxidation/reduction reactions of the nanoscale $\text{Co}_3\text{O}_4/\text{SmCoO}_3$ precursor oxides to a metallic Sm-Co alloy are examined in an effort to improve this class of synthesis techniques. The synthesis of the precursor oxide is described in depth, as is the technique used to measure the energetics of individual steps of this oxidation/reduction reaction.

Platinum nanoparticles are of great interest, largely due to the use of these particles in medical and energy storage fields and the use of Pt alloys in magnetic applications [7, 12, 16, 37, 38]. The stability of Pt nanoparticles and the mechanisms

by which they sinter has been a topic of study for many years [39-42]. However, there are still questions and disagreements as to the mechanisms by which these nanoparticles sinter [43-47], and the way in which certain physical properties, such as shape and inter-atomic spacing, change upon grain growth are still not well understood [48-50]. There is also evidence that the method of preparation of these nanoparticles can strongly influence the evolution of these material properties [51, 52].

In this work, Pt nanoparticles are synthesized via a grain-growth technique and sintered using two different heating techniques. In an attempt to avoid confusion or comparison with systems that differ drastically in synthesis and measurement methods, as much detail as possible is provided. This work specifically examines the evolution of the Scherrer grain size and the lattice parameter of these Pt nanoparticles. In addition, preliminary results of an investigation into the diffusion of Pt and Ni in a multilayer structure, as well as synthesis of core/shell Pt/Ni structures are described.

This thesis contains six chapters. In chapter two, many of the theoretical treatments used in examinations of the properties outlined above are described, including the bulk formulae governing diffusion and sintering and the theoretical justification for the extraction of activation energies from oxidation/reduction experiments. Chapter three contains important experimental details, such as the synthesis techniques for the Pt, Pt/Ni and Sm-Co-O samples used in this work.

Chapters four and five contain the experimental results and analysis, and represent the largest portion of this work. In chapter four, the activation energies for three oxidation/reduction reactions are measured; the reduction of Co_3O_4 to Co, the reduction of SmCoO_3 to a nanoscale mixture of Sm_2O_3 and CoO, and the reduction of CoO to Co when mixed at the nanoscale with Sm_2O_3 . In chapter 5, Pt nanoparticles are

sintered in two ways, by conventional uniform heating and by an optical pump technique using an ultrafast laser. The evolution in the lattice parameter and grain size of the Pt nanoparticles is tracked as a function of sintering time, temperature, and incident energy. In addition, preliminary results of intermetallic diffusion in a bimetallic Pt/Ni multilayer system are presented.

The final chapter contains a description of the ongoing research in these projects, as well as a selection of related projects of some interest. These focus on the synthesis and testing of diffusion in bimetallic systems, as well as the synthesis of magnetic alloys, and may be appropriate research for a future student.

Chapter 2

THEORETICAL BACKGROUND

The following sections briefly describe some of the standard models and rules that describe the processes of diffusion and phase transformations in bulk materials. Also shown are assumptions inherent in these models that do not apply to nanoscale systems, as well as methods to extract some of these properties from the laboratory measurements.

2.1 Diffusion

Diffusion, and by extension sintering, in bulk systems is typically expressed using Fick's laws [53]. These formulae provide a simple but powerful set of guidelines to diffusion on the macroscale, namely that atoms diffuse from areas of high concentration to areas of low (the 1st law) and the rate of diffusion is proportional to the gradient of the atomic concentration (the 2nd law). For the special case of one-dimensional diffusion, these laws are written as follows:

$$J = -D \frac{\partial \phi}{\partial x}$$

And

$$\frac{\partial \phi}{\partial t} = D \frac{\partial^2 \phi}{\partial x^2}$$

Where $\phi = \phi(x, t)$ is the position- and time-dependent concentration and D is the bulk diffusion constant. For completeness, both these results are derived in the following sections, and further information may be found in chapter 12 of Reif's book.

2.1.1 Fick's First Law

Fick's first law is the result of examining a random walk problem in the context of a non-uniform concentration. Assume a three-dimensional concentration profile $\phi = \phi(x, y, z)$, where particles move with velocity v and the change in concentration in the x direction can be written

$$\delta\phi = \lambda \frac{\partial\phi}{\partial x}$$

Consider the number of particles passing through a two dimensional plane in the y - z axis.

$$J_{L \rightarrow R} = \frac{1}{6} v \phi \lambda$$

$$J_{R \rightarrow L} = \frac{1}{6} v (\phi + \delta\phi) \lambda$$

$$J = J_{L \rightarrow R} - J_{R \rightarrow L}$$

$$J = -\frac{1}{6} v \delta\phi \lambda$$

$$J = -\frac{1}{6} v \left(\frac{\partial\phi}{\partial x} \right) \lambda^2$$

$$J \equiv -D \frac{\partial\phi}{\partial x}$$

2.1.2 Fick's Second Law

Combine Fick's first law and a mass conservation condition.

$$J \equiv -D \frac{\partial\phi}{\partial x}$$

$$\frac{\partial\phi}{\partial t} + \frac{\partial J}{\partial x} = 0$$

$$\frac{\partial \phi}{\partial t} - \frac{\partial}{\partial x} \left(D \frac{\partial \phi}{\partial x} \right) = 0$$

To simplify this relationship use a variable substitution commonly known as the Boltzmann transformation. Consider the variable ξ , a function of x and t .

$$\xi = \frac{x}{2\sqrt{t}}$$

$$\frac{\partial \xi}{\partial x} = \frac{1}{2\sqrt{t}}$$

$$\frac{\partial \xi}{\partial t} = \frac{-\xi}{2t}$$

Substituting ξ into Fick's Second Law using the chain rule,

$$\frac{\partial \phi}{\partial \xi} \left(\frac{-\xi}{2t} \right) - \frac{1}{4t} \frac{\partial}{\partial \xi} \left(D \frac{\partial \phi}{\partial \xi} \right) = 0$$

This yields an expression that is only a function of ξ ,

$$-2\xi \frac{d\phi}{d\xi} = \frac{d}{d\xi} \left(D \frac{d\phi}{d\xi} \right)$$

This substitution has two results. First, it simplifies the expression, allowing for a straightforward description of the concentration. Second, there is a trivial result illuminated here: Fick's second law must hold for

$$\frac{d\phi}{d\xi} = 0$$

This condition is met for the relationship

$$x \propto \sqrt{t}$$

This is the same relationship expected from classical random displacement calculations, the product of the "random walk" class of problems.

2.1.3 Expanding Fick's Laws to the Nanoscale

It is important to recognize the breakdown in these expressions in nanoscale systems. For systems where the concentration profile is not continuous, such as core-shell or multilayer bimetallic systems, the spatial derivatives of the concentration profile are ill defined, and these expressions are poor predictors of observable behavior. They also break down when the diffusion constant is a function of concentration, as is possible in systems where new phase formation occurs.

2.2 Size dependence of the lattice parameter

An example of a bulk behavior extending unpredictably to small sizes is the size-dependence of the lattice parameter of metals. The lattice parameter of a metal is a size-independent property in a bulk system. However, this property changes noticeably at the nanoscale due to surface stresses. These stresses are a result of the large surface area to volume ratio in small particles, and is important at sizes 100s of nanometers or less. The lattice parameter of a small particle is commonly written with a $1/d$ dependence [54], a result often referred to as the Laplace equation.

$$\frac{a - a_0}{a_0} = -\frac{4\sigma}{3Bd}$$

In this equation, a is the lattice parameter of the small particle, a_0 the bulk lattice parameter, σ the surface stress, B the bulk modulus and d the diameter of the particle. Results with a similar functional form have been described for nanoscale particles, nanowires, two-dimensional films and multilayered thin films [55-58]. Although the details of these results differ, all share approximately the same $1/d$ size dependence of the lattice parameter on particle size. In addition, none allow for non-monotonic evolution with increasing particle size, behavior which as has been observed in metals including Ni, Fe, W, and Cu [59, 60]. This non-monotonic behavior is typically

observed in systems where size-reduction is accomplished by destructive milling techniques, and is likely highly dependent on the synthesis method of the sample being measured.

2.3 Periodic Composition effects in XRD

X-ray diffraction (XRD) exploits symmetries in the crystal structure of a material to determine properties of that material. An incident x-ray beam constructively interferes at specific angles set by the structure of the crystal lattice. The angles of constructive interference are given by Bragg's law.

$$n\lambda = 2d \sin(\theta)$$

Here, n is an integer, λ the incident wavelength, d the spacing between symmetry planes in the lattice, and θ the incident angle between the x-ray and the lattice planes. This technique is widely used to determine the lattice parameter of bulk materials as well as nanocrystalline samples, and this technique is discussed in depth in chapter three. This technique is complicated, however, in the case of a multilayer structure with a well-defined periodicity. In addition to the normal Bragg diffraction from the lattice, two additional effects are seen. These are a low-angle effect due to elemental interfaces, and additional peaks near the Bragg peaks due to the compositional modulation.

2.3.1 Low Angle Signals

The origin of the low angle signal is constructive interference from reflections off inter-layer interfaces. This signal is not linked to the internal crystal structure of either constituent element, but rather the distance between these interfaces. The angles of these signals are again given by Bragg's law. However, rather than the crystal

lattice spacing d , the distance of interest is the length of the compositional modulation. The same analysis used to determine the spacing of the crystalline lattice can therefore be used to determine the compositional modulation.

As diffusion begins and the interfaces blur, softening the edges of the composition profile, the highest order peaks rapidly are suppressed. Although this barely changes the most intense, lowest angle diffraction peaks, the effect is visible very early in the diffusion process. It is a far earlier indicator of diffusion than the Bragg peaks, although it is not sensitive to new phase formation.

2.3.2 Diffraction around the Bragg angle

Along with the low angle peaks, a second new feature is visible when performing diffraction on multilayers. This is the presence of sidebands around the Bragg peaks. Phenomenologically, these bands are the result of irregular spacing of crystalline lattice planes due to the presence of differently spaced atomic layers, i.e. multilayers of different atomic composition. The signal is highly dependent on both the periodicity of the structure, and the lattice spacing of each constituent element.

A full derivation for this effect can be found in reference [61]. The magnitude of the scattered radiation due to this effect can be written

$$g(k) = \sum_n \frac{2\pi\mathcal{F}}{d_0} \delta\left(k - \frac{2\pi n}{d_0}\right) - \frac{2\pi\mathcal{F}}{d_0} \sum_n \left[\left(\frac{\epsilon k}{\beta} - \frac{\Delta\mathcal{F}}{\mathcal{F}_0}\right) * \delta\left(k - \frac{2\pi n}{d_0} - \beta\right) + \left(\frac{\epsilon k}{\beta} + \frac{\Delta\mathcal{F}}{\mathcal{F}_0}\right) * \delta\left(k - \frac{2\pi n}{d_0} + \beta\right) \right]$$

In this expression, k is the scattering vector along the direction of the composition modulation, β is the periodicity of the composition modulation given by

$$c(x) = c_0 + A\sin(\beta x)$$

The position dependent atomic scattering factor is given by

$$\mathcal{F}(x) = \mathcal{F}_0 + \Delta\mathcal{F}\sin(\beta x)$$

Certain parameters have been defined as follows:

$$\mathcal{F}_0 \equiv c_0\mathcal{F}_1 + (1 - c_0)\mathcal{F}_2$$

$$\Delta\mathcal{F} \equiv A(\mathcal{F}_1 - \mathcal{F}_2)$$

Scattering factors of the component materials are given by \mathcal{F}_1 and \mathcal{F}_2 .

This modulation leads to a position-dependent lattice spacing

$$d(x) = d_0(1 + \epsilon * \sin(\beta x))$$

In this case, ϵ is the strain parameter

$$\epsilon = AW\eta$$

In this expression, the lattice expansion due to compression is defined $\eta = \frac{1}{a} \frac{\partial a}{\partial c}$, and W is a parameter set by the elastic properties of the material.

This result represents normal scattering at the Bragg condition (the first term), as well as scattering at antisymmetric satellites at $\pm\beta$, the periodicity of the lattice. This result means sideband positions can be used as an indicator of layer thicknesses in multilayer systems. The intensity of sidebands is a function of ϵ and $\Delta\mathcal{F}$. As $\Delta\mathcal{F}$ is proportional to the difference in scattering factors between layers and ϵ is a function of lattice expansion, these sideband intensities indicate similarities of the lattice parameters, and by extension the amount of intermetallic diffusion, in a multilayer system.

2.4 Activation Energies

In this work, the energy required to reduce certain Sm- and Co- containing oxides was determined using a series of isothermal measurements. The temperature dependence of the rate of conversion from the initial oxide to the final phase was measured analyzed using a method derived below.

2.4.1 Extracting activation energies from isothermal measurements

To begin, assume two conditions. First, the rate of conversion of a system is dependent on both the temperature and amount already converted in that system.

$$\frac{\partial \alpha}{\partial t} = \Phi(T, \alpha)$$

Second, this dependence can be written as the product of independent functions.

$$\Phi(T, \alpha) = k(T)f(\alpha).$$

From these assumptions,

$$\frac{\partial \alpha}{\partial t} = k(T)f(\alpha)$$

And separating variables and integrating from a state of 0 conversion to the final state yields

$$\int_0^{\alpha} \frac{1}{f(\alpha)} d\alpha = k(T) \int_0^{t_{\alpha}} dt$$

$$\int_0^{\alpha} \frac{1}{f(\alpha)} d\alpha = t_{\alpha}k(T)$$

$$F(\alpha) - F(0) = t_{\alpha}k(T)$$

$F(x)$ is the integrated function $\frac{1}{f(x)}$ and t_{α} is the time elapsed to reach an amount of conversion α . The conversion time t_{α} can then be isolated.

$$t_{\alpha} = \frac{F(\alpha) - F(0)}{k(T)}$$

For a set amount of conversion α , the time t_{α} required to reach that conversion is inversely proportional to the function $k(T)$. Set a functional form for k such that k depends on the activation energy E and a scaling factor A .

$$k(T) = Ae^{-\frac{E}{kT}}$$

$$t_{\alpha} = \left(\frac{F(\alpha) - F(0)}{A} \right) e^{\frac{E}{kT}}$$

$$\log(t_{\alpha}) = \log\left(\frac{F(\alpha) - F(0)}{A}\right) + \frac{E}{kT} \log(e)$$

Therefore, by measuring the time to achieve a set amount of conversion (t_{α}) at different temperatures (T) and plotting the logarithm of the time as a function of the inverse temperature (an Arrhenius plot), the slope of the data is proportional to the activation energy. The y-intercept of this data can be used to determine information about the $F(\alpha)$ function, the conversion-dependent portion of the general conversion relation, although that analysis is not performed here.

It is helpful to note that the activation energy analysis does not assume or require any exact values for sample masses or amounts of conversion. The importance of this result will become clear in chapter and four.

Chapter 3

EXPERIMENTAL TECHNIQUES

This chapter details the most important experimental techniques that are referenced in chapters 4 and 5. A brief theoretical background and certain important sample preparation techniques are presented for X-ray diffraction (XRD) and thermogravimetric analysis (TGA).

3.1 X-Ray Diffraction

X-ray diffraction (XRD) is a widely applicable method for analysis and characterization of ordered crystalline materials. It is used on a variety of drastically different timescales with different sources and detection methods, even in the measurements detailed here, but the basic principle is identical in any regime. In general terms, an incident x-ray scatters from a sample volume, and at certain angles portions of the beam scattering from different locations constructively interfere. The pattern of angles and intensities of observed constructive interference is a fingerprint of the crystalline lattice, and provides useful information in identifying crystalline phases and various effects on the lattice.

3.1.1 Lattice Structure

Materials are grouped by their crystalline lattice structure into space groups, categories of crystalline structures with characteristic patterns of XRD peaks. The angular position of each peak depends on the lattice spacing, and by extension the material, but materials with the same crystalline structure will have similar patterns. Observation of an XRD pattern combined with prior knowledge of the composition of

a sample often allows direct determination of the phase of the material present in the sample.

Determination of these space groups is done by examining the angles at which x-rays are coherently diffracted and the strength of those diffractions. These angles must satisfy the Bragg condition for coherent reflection. In crystallographic systems, the reflection planes are planes of symmetry in the crystallographic structure. The angle and relative intensity of the scattered radiation can be calculated by knowing the atomic positions of each atom present in the material, coordinates which are well known for most common structures.

Most of the experiments presented here focused on elemental Pt with a face-centered-cubic (fcc) crystal structure and Ni with either a fcc or hexagonal close-packed (hcp) crystal structure. Multilayer samples used fcc Ni, while bimetallic nanoparticles were made with hcp Ni.

3.1.2 Measurement Geometries

The measurement geometry is tailored to the sample being measured. One geometry in this work is a coupled $\theta/2\theta$ measurement with identical incident and reflected angles, generally known as a Bragg-Brentano scattering geometry (figure 3.1a). This is appropriate for bulk samples, either powder or single crystal, and allows for the greatest angular scanning range in a standard laboratory XRD.

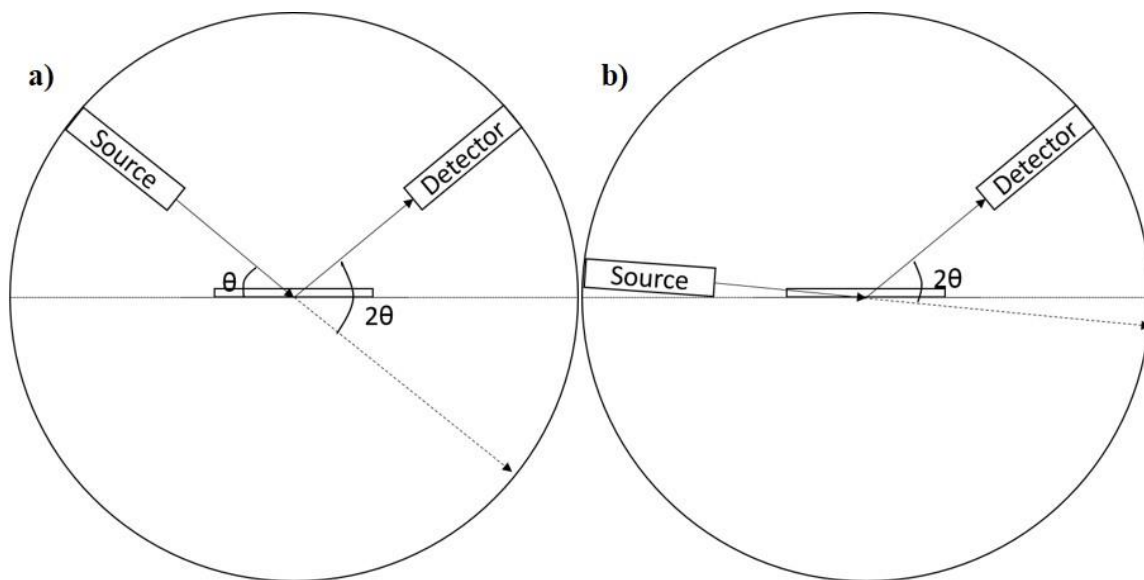


Figure 3.1: The two laboratory XRD geometries used in this work were a symmetric θ - 2θ geometry (a) and a grazing incidence geometry (b).

An alternate geometry (figure 3.1b) fixes the incident angle at a small value and only sweeps the detector. This method, called grazing incidence, is appropriate for thin samples where the penetration depth of a standard $\theta/2\theta$ measurement would be much greater than the sample thickness. The angular range of this measurement is half that of the symmetric measurement range.

The third geometry used in this work involved a stationary source and sample and a fixed area detector, shown in figure 3.2. The angular range is determined by the size of the detector and the detector distance from the sample. Depending on the transparency of the substrate, 50% or more of the scattered x-rays can be collected, vastly improving the signal to noise ratio compared to a standard Bragg-Brentano measurement. This method was only used at the APS synchrotron.

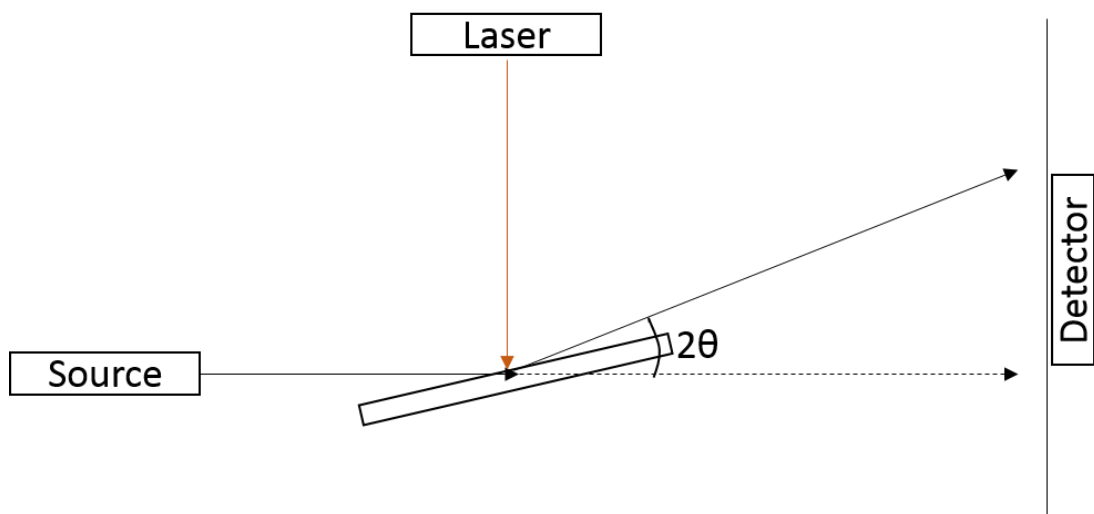


Figure 3.2: Fixed source (pump-probe) scattering geometry. An area detector collects scattered photons over a large solid angle (angular resolution and range is set by the distance from the sample to the detector).

A typical 2-D diffraction spectrum as acquired at the APS is shown in Fig 3.3. These surface images were subsequently processed into a 1-D form by performing a radial integration. The center pixel was calculated using a CeO_2 standard sample. Background subtraction proved difficult, primarily due to ablating material causing a non-uniform background, but systematic effects due to binning and integration were subtracted. As the illuminated sample volume is well-controlled and small, this geometry is useful for pump-probe style measurements, where near-uniform excitation can be achieved over the measurement volume.

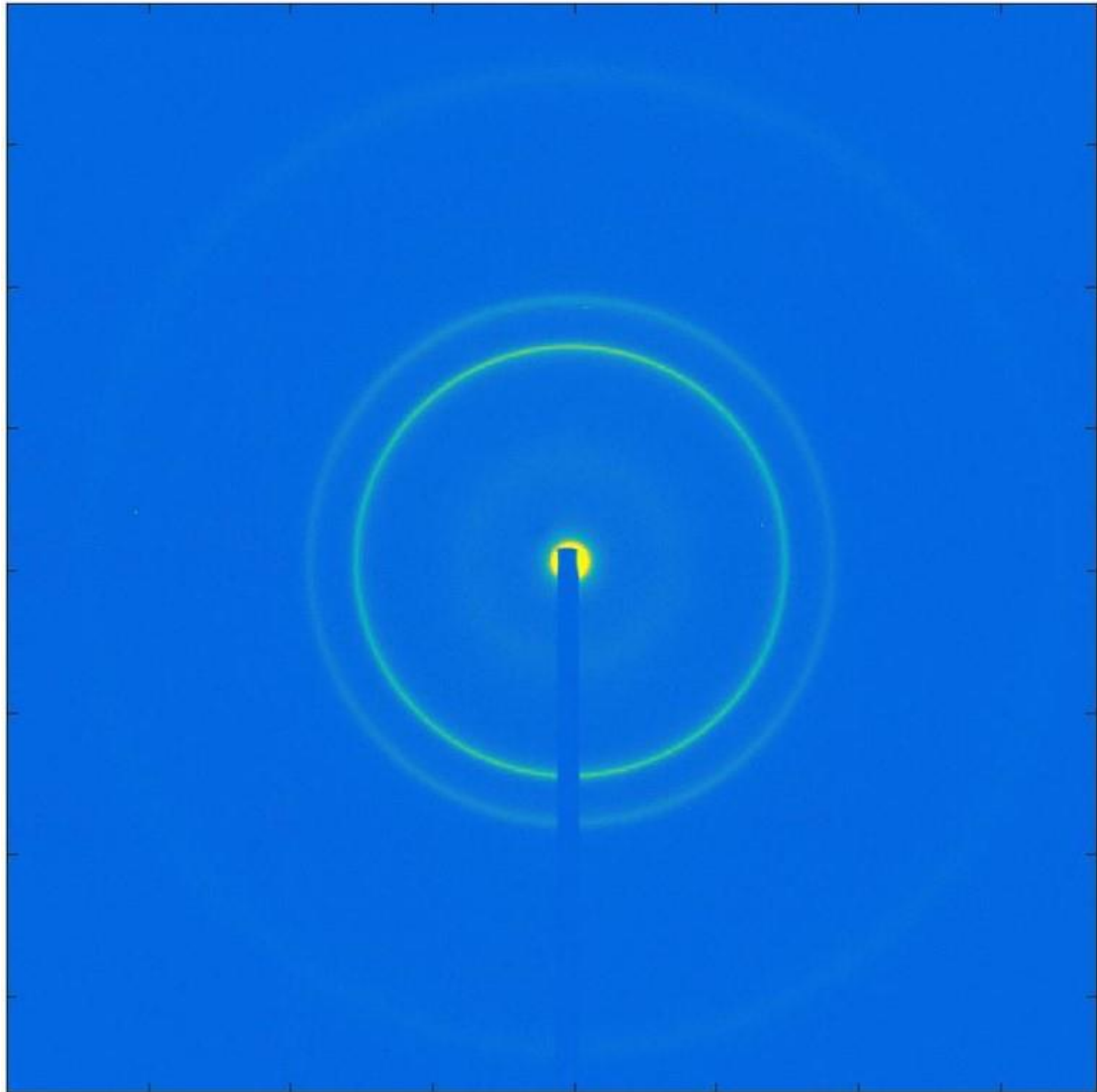


Figure 3.3: Sample output of an XRD spectrum collected by an area detector. This is a powder Pt sample, and the (111), (200), and (220) peaks are visible.

3.1.3 Peak shape effects

There are several geometric effects that alter the observed XRD signal of a sample. Of special importance in these experiments are effects due to heating and particle sizes, as well as the instrumental effects that contribute to line broadening.

3.1.3.1 Temperature

At elevated temperatures the increased atomic kinetic energy of the material causes the lattice to expand with a shift in peak positions to smaller diffraction angles. The corresponding lattice parameter shift can be used to infer sample temperature if the thermal expansion coefficient of the material is known.

3.1.3.2 Finite Size

The second effect seen when examining nanomaterials is a finite size effect. When the size of the crystalline domains of a material are 10s of nanometers or smaller, increased surface stress due to small particle sizes leads to shifted and broadened diffraction peaks, which may result in higher or lower diffraction angles. The magnitude and direction of the shift can be used to calculate the amount and nature of the stress.

In this work, we calculate the lattice parameter of nanoscale particles using Bragg's law and knowledge of the crystal structure of the particles being examined. Bragg's law allows direct calculation of the d-spacing of lattice planes from the diffraction angle. As most of our work used metals in an FCC structure, we obtained lattice parameters using the relationship

$$d_{hkl} = \frac{a}{\sqrt{h^2 + k^2 + l^2}}$$

Similar relationships can be obtained for other crystal structures by examining the geometry of the unit cell.

The second effect is line broadening. Grain size can be directly calculated from the peak width by applying the Scherrer formula.

$$D = \frac{K\lambda}{B\cos(\theta)}$$

Here, K is a Scherrer shape factor, λ the incident x-ray wavelength, B is the full width at half the maximum of the diffraction peak, and θ the Bragg angle of the peak.

Assuming constant K , λ , and θ , the peak width is simply inversely proportional to the grain diameter. In practice, changing particle sizes will cause changes in both the B and θ parameters, but λ is always constant, and K is generally assumed to be constant as well.

3.1.4 Scherrer Analysis

Both of these analyses suffer from a fundamental limitation when trying to determine particle size of a material. XRD peak broadening and position, while colloquially generally attributed to “particle size”, are a function of the coherent scattering length of a material, i.e. the distance over which the crystalline structure is aligned. This is commonly referred to as the “grain size” of the material. If the particles being measured are single crystals, then these sizes are identical. In the case where particles are polycrystalline, though, these values can be drastically different. Alternate characterization methods such as SEM or TEM are required to determine if a particle is polycrystalline.

3.1.5 Analysis Software

Most XRD analysis was performed using the proprietary PDXL Rietveld fitting package from Rigaku or standard fitting routines in Origin. A Pearson VII function was used to fit the lineshape.

$$I(2\theta) = I_{max} \frac{w^{2m}}{[w^2 + \left(\frac{1}{2^m} - 1\right) (2\theta - 2\theta_0)^2]^m}$$

In this formula, I is the intensity of the scattered radiation, w is a fitting parameter to vary the width of the peak, and m is a shape factor for the lineshape. This function can be used to fit lineshapes from Lorentzian ($m=1$) to Gaussian (large m). Instrumental effects were subtracted using automatic PDXL deconvolution routines with a measured Si standard spectrum.

3.2 Thermogravimetric Analysis

This work was performed using a DSC/TGA instrument capable of both differential scanning calorimetry (DSC) and differential thermal analysis (TGA) measurements. Primary use was of the TGA function. In this measurement, differential mass readings were made between a sample pan and an empty reference pan, and changes in the differential mass are recorded as a function of the temperature. These measurements were used to study the thermodynamics and kinetics of a series of conversions at different temperatures based on the isoconversional analysis detailed in Ch. 2. As a reminder, the relationship between conversion time and sample temperature was as follows:

$$\log(t_\alpha) = \log\left(\frac{F(\alpha) - F(0)}{A}\right) + \frac{E}{kT} \log(e)$$

3.2.1 Analyzing Isothermal Measurements

This work discusses the activation energies of three distinct oxidation/reduction reactions; Co_3O_4 to Co metal, SmCoO_3 to a nanoscale mixture of Sm_2O_3 and CoO, and CoO to Co metal in the presence of Sm_2O_3 . Although the temperatures used in these measurements were different, the analysis was identical. In

each case, a series of isothermal measurements were made at varying temperatures, and fractional mass changes were recorded as a percent of total conversion, α .

Although the relationship between conversion time t_α and temperature T is relatively straightforward, two parameters must be measured carefully to perform this analysis: the beginning mass of the material, and an appropriate time $t=0$ corresponding to the start of the transformation. Although simple in concept, these are deceptively difficult to accurately measure in real-world measurements.

Accurate calculation of the initial mass, and by extension the amount of conversion of a sample, was challenging due to relaxation and variations in the balance over the length of a measurement. In this work, the initial mass was calculated using extended isotherms at elevated temperature for stability. In the case of the Co_3O_4 transition, the initial oxide mass was measured at 100°C , and the final metallic Co mass was measured at 350°C . The amount of conversion was calculated using both these values. In the SmCoO_3 to $\text{Sm}_2\text{O}_3+\text{CoO}$ conversion, the initial mass was not measured. Instead, the final mass was measured at 330°C after the conversion was completed. The initial mass was calculated via stoichiometric arguments. In the CoO to Co conversion, the opposite was true. The initial mass was measured at 350°C , and the final mass was calculated using stoichiometric arguments.

Assigning a time $t=0$ was similarly challenging. Although it would seem logical to set the beginning of the isotherm of interest as time 0, such a determination would neglect any conversion occurring during the ramp portion of the measurement. An alternate method was to set $t=0$ to correspond to a time when the sample mass varied outside a set tolerance, but the beginning of the “isotherm” was then at a lower temperature, effectively overestimating the heat delivered to the system. There was no

perfect method for setting this parameter. The approach used in this work depended on the system being analyzed, as the specifics of the temperature sequences used varied. The uncertainties inherent in this determination were conservatively estimated, and further minimized by focusing on the analysis of conversions that occur at long times t_a .

3.2.2 Properly performing DSC/TGA measurements

Due to the high degree of accuracy and stability required for these measurements, special care was taken to isolate measured signals from any external influence. Stated tolerances for the TA Instruments Q600 used in this work are listed in table 3.1.

CONDITION	MASS TOLERANCE
ROOM TEMPERATURE CHANGES	<50 μ g/ $^{\circ}$ C
RAMP FROM 50$^{\circ}$C TO 1000$^{\circ}$C	<50 μ g
RAMP FROM 50$^{\circ}$C TO 1500$^{\circ}$C	<100 μ g

Table 3.1: Stated mass variation tolerances during DSC/TGA measurements under temperature ramps and room temperature changes. These values were provided by Matthew Reader at TA instruments.

As most of the measurements of interest were isotherms, mass variations during temperature ramps were often unimportant. However, changes of room temperature alone were a significant source of mass fluctuations during isotherms. To correct for this instability, a series of isothermal measurements of Al_2O_3 , an inert powder, were performed in N_2 atmosphere. Temperature-dependent mass variations in this inert sample were analyzed to determine systematic fluctuations.

In the following sections “temperature” and “sample temperature” will often be used interchangeably, and refer to the temperature measured at the sample pan. The other temperature measured and used is labeled “case temperature”. This is a diagnostic temperature measurement collected in the DSC system. It is a measure of the temperature of the electronics of the system, and coupled to both the sample temperature and the room temperature.

3.2.3 Temperature Corrections

A 10mg alumina sample was used to measure mass changes due to sample and case temperature fluctuations at a series of 6 isothermal temperatures from 100°C to 350°C. These measurements were performed in inert N₂ atmosphere. A plot of the temperature sequence is shown in figure 3.4. To ensure a clean sample, the alumina was first heated to 1000°C then cooled to room temperature in constant N₂ flow. A series of 10 hour isotherms were separated by rapid (20°C/min) ramping steps, and the sample mass, sample temperature, and case temperature were recorded every 10 seconds throughout the measurement.

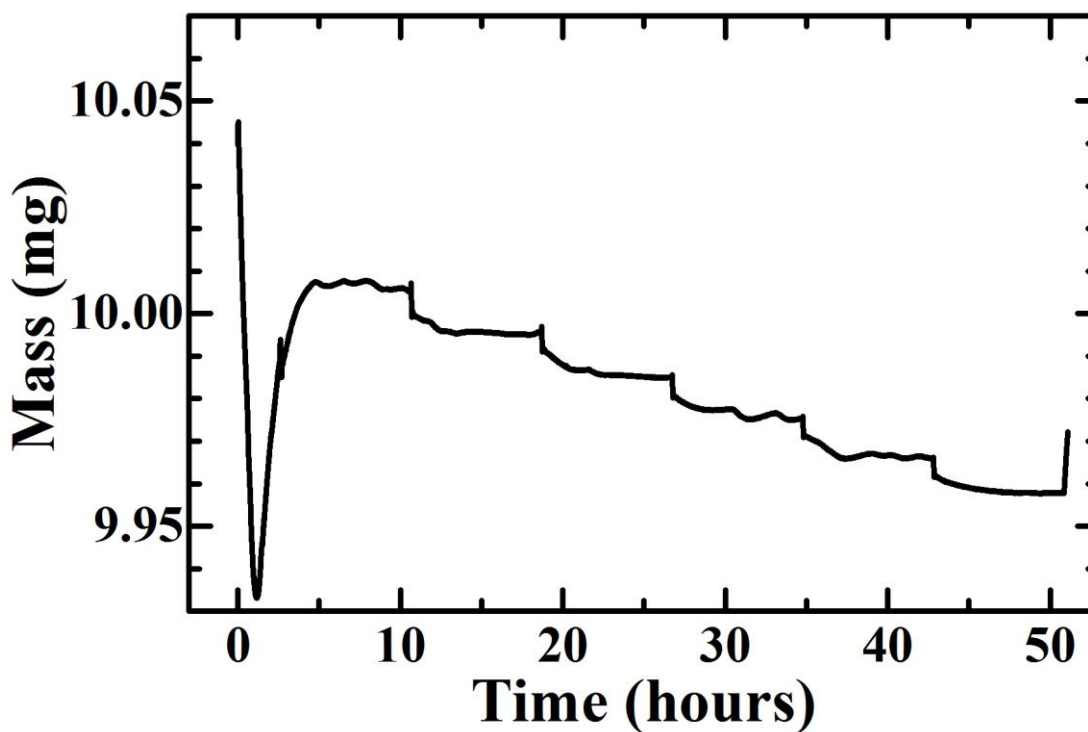


Figure 3.4: As-measured mass of a 10mg alumina sample during a series of isotherms from 100°C to 350°C.

The temperature dependence of the mass reading was determined in two steps. First, case temperature variations were examined and corrected. Then, systematic variations due to sample temperature changes were examined.

To determine case temperature dependence, mass measurements during each isotherm were plotted as a function of the case temperature. In each case, increasing case temperatures were strongly correlated to decreasing mass measurements (figure 3.5). This dependence was determined in each case with a simple linear fit to the mass data, yielding case temperature dependence from $-7.92\mu\text{g}/^\circ\text{C}$ to $-9.39\mu\text{g}/^\circ\text{C}$, and an average of $-8.55\mu\text{g}/^\circ\text{C}$. The slopes obtained from the fits did not systematically vary,

suggesting differences in slope were not temperature-dependent, but rather were random error.

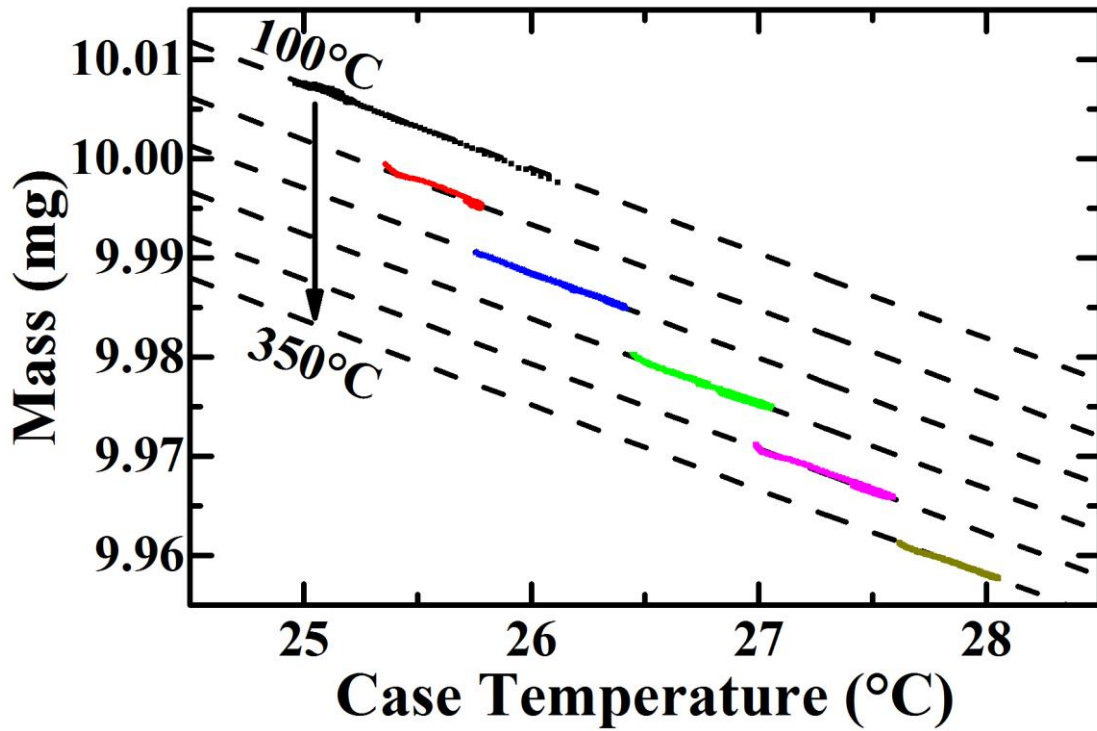


Figure 3.5: Sample masses for each of the isotherms. Measurements were made in 50°C increments. Case temperature variations 0.5°C or greater were observed for each 10h isotherm.

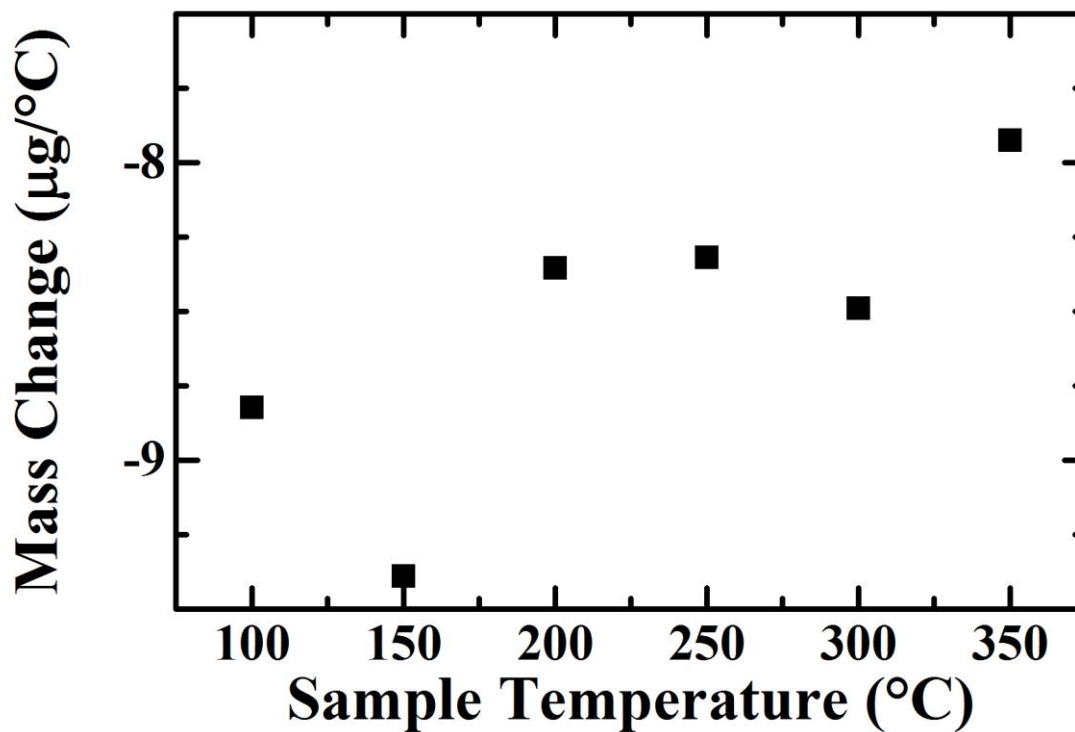


Figure 3.6: Case temperature dependence of the mass at each measurement isotherm. Error bars for each fit are smaller than the symbols.

Based on this observation, each isotherm was re-fit using this average case temperature dependence. The linear offset between the fits was used to determine the sample temperature effects on the mass measurement (figure 3.6). This offset was fit to a quadratic and provided a functional form for the sample temperature correction (figure 3.7). This quadratic may not have been a good fit at temperatures well above 350°C, but this range was sufficient for the measurements in this work.

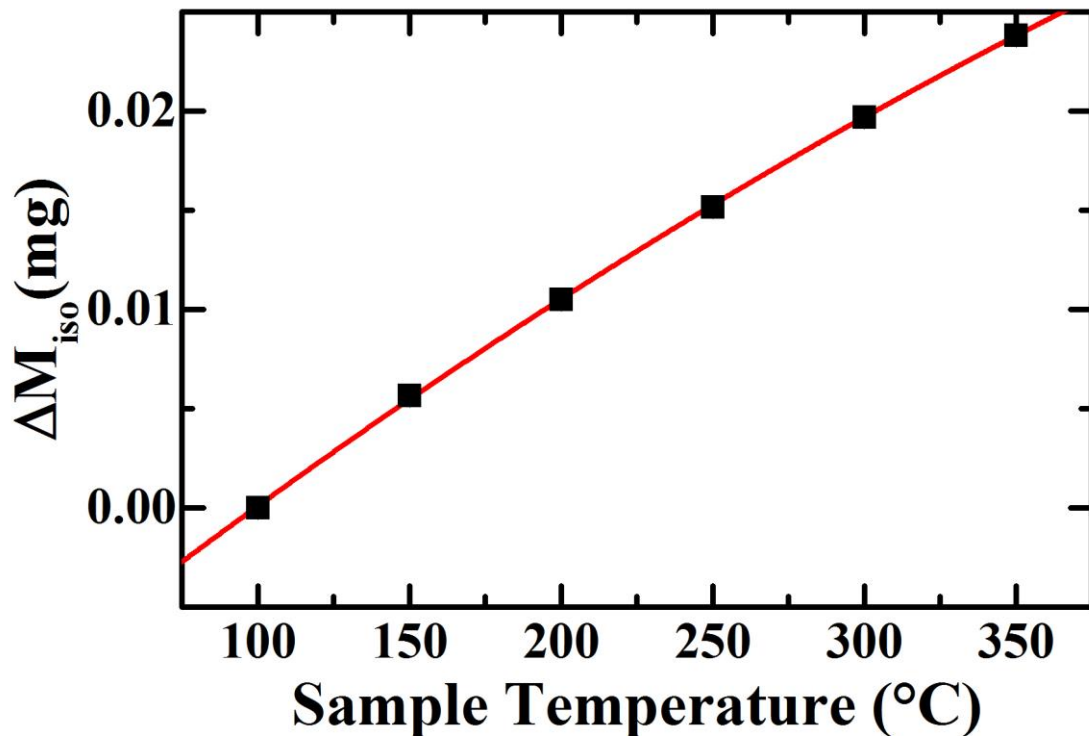


Figure 3.7: The mass offset of fits at each isothermal temperature. These offsets have been fit to a second order polynomial to quantify mass changes due to sample temperature. Changes in mass are plotted as a difference from the 100°C isotherm mass measurement to make the graph clear.

The correction factors were added to the as-measured sample mass, and an additional scalar factor was subtracted from the corrected mass measurement to match the measured sample mass to the room temperature measurement (figure 3.8). This simple sum of corrections stabilized the isothermal portions of the measurements quite well. The as-measured signal contained a 0.4% variation in mass over the 250°C measurement window, as well as 0.04% variations due to room temperature changes during isothermal measurements. After applying the linear correction, both these effects were reduced by a factor of 10. The mass measurements during the temperature ramps were also improved. Further improvements to specifically the ramping portions

may be possible, but we focused on the isotherms due to the nature of the isoconversional measurements of interest.

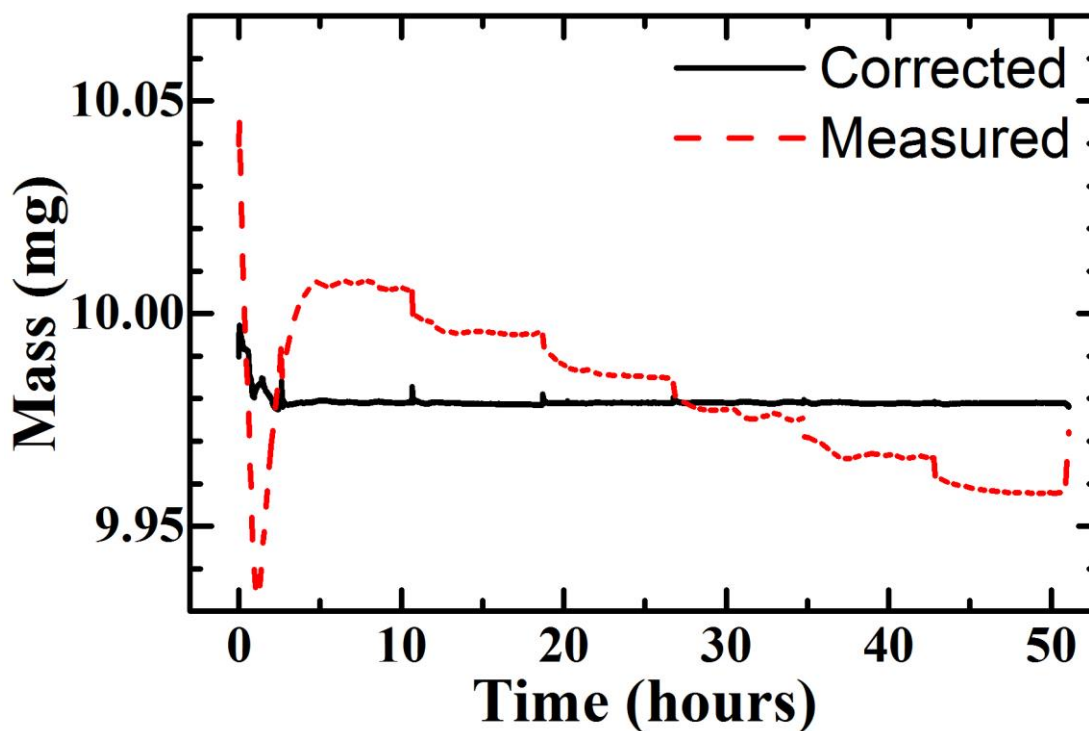


Figure 3.8: The as-measured and corrected mass data. The corrected data shows variations an order of magnitude smaller than the uncorrected.

This correction was implemented for isothermal measurements where the case temperature effect was seen, specifically those measuring the SmCoO_3 sequence of transitions. The Co_3O_4 to Co transition did not appear to be influenced by this effect, so no correction was made to those measurements.

3.3 Pt and Pt/Ni Particle Preparation

The platinum samples used for these measurements were synthesized via a seed-growth method modified from the one used by Bigall et al [62]. Nickel shells were added by a subsequent reduction step in the presence of sintered Pt clusters. While the seed solution was stable over several months, every other solution used in this procedure was prepared as close to the time of synthesis as possible.

3.3.1 Seed Solution

A dilute solution of 5nm platinum seeds was prepared by the addition of 36mL of a 3.86 mM Dihydrogen Hexachloroplatinate (IV) (H_2PtCl_6) aqueous solution to 464mL of boiling deionized water. After 1 minute, 11mL of a 33.8mM Trisodium Citrate ($\text{Na}_3\text{C}_6\text{H}_5\text{O}_7$)/2.60mM Citric Acid ($\text{C}_6\text{H}_8\text{O}_7$) aqueous solution was added, followed 30 seconds later by 5.5mL of a 21.2mM Sodium Borohydride (NaBH_4)/33.8mM Trisodium Citrate/2.60mM Citric Acid aqueous solution. After boiling for 10 minutes, the seed solution was cooled and stored at room temperature until needed.

3.3.2 Pt Cluster Synthesis

To synthesize the platinum nanoclusters, 3.6mL of the seed solution was added to 87mL deionized water at room temperature. 10.5mg of platinum was added in the form of 0.135mL of 0.4M Chloroplatinic Acid (H_2PtCl_6) solution, quickly followed by 1.5mL of a 33.8mM Trisodium Citrate/71.0mM L-ascorbic Acid ($\text{C}_6\text{H}_8\text{O}_7$) solution. The solution was heated to 100°C at a rate of approximately 4°C/min, held at reflux for 30 minutes, and quenched with ice water or allowed to naturally cool to room temperature, as shown in figure 3.9. The solution was centrifuged at 10,000 RPM for 10 minutes and re-suspended in water. This process was repeated 3 times.

After each iteration, as much supernatant as possible was removed via pipette and replaced by deionized water. After this cleaning, the particles were stored in a solution suitable for the ultimate use of the particles. Particles to be used for Pt/Ni synthesis or to be stored for long term were suspended in triethylene glycol (TEG) ($C_6H_{14}O_4$), particles to be used for microscopy were placed in ethanol, and particles to be deposited on monolayers or used for x-ray diffraction measurements were stored in water.

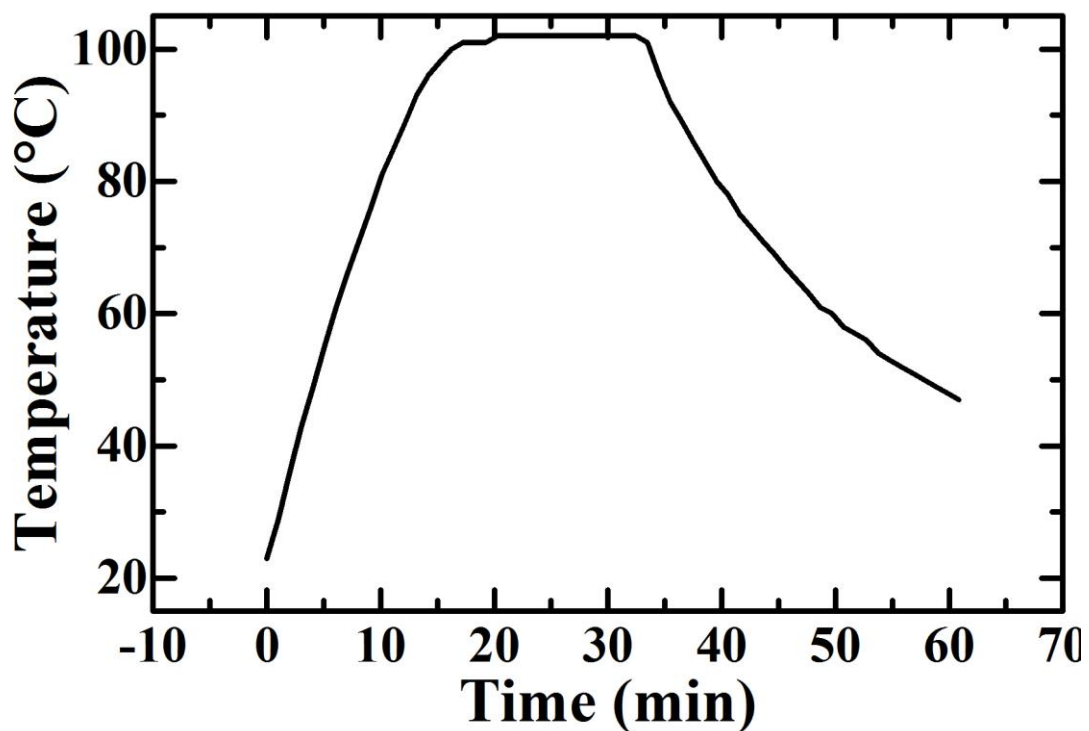


Figure 3.9: A typical heating profile for 30nm Pt cluster synthesis. More rapid heating produced smaller clusters, although individual Pt grain sizes were independent of heating rate.

3.3.3 Ni addition to Pt clusters

Ni was added to the Pt clusters via polyol reduction reaction at high temperature. As-washed Pt nanoclusters in TEG were heated above 230°C. This temperature was not strictly necessary to reduce the Ni ions to Ni metal, but was essential to create the hexagonal close packed (hcp) phase of Ni rather than the magnetic face centered cubic (fcc) phase. This temperature also began to sinter the Pt nanocluster core, an advantageous side effect. Upon reaching sufficient temperature, Ni acetate was added as a powder in a 1-1 molar ratio with the Pt present in the solution. The TEG reduced the dissolved Ni ions to metallic Ni, which plated on the Pt clusters. After 5 minutes the reaction vessel was removed from the heat source and cooled naturally to room temperature. The particles were cleaned by washing in ethanol or TEG in the same method as the Pt nanoclusters, and were dried or suspended in TEG or ethanol for later measurements.

3.4 As-Prepared Particles

As-prepared Pt clusters and Pt/Ni nanostructures were analyzed by XRD and transmission electron microscopy (TEM) before sintering or diffusion measurements were performed.

3.4.1 Pt Clusters

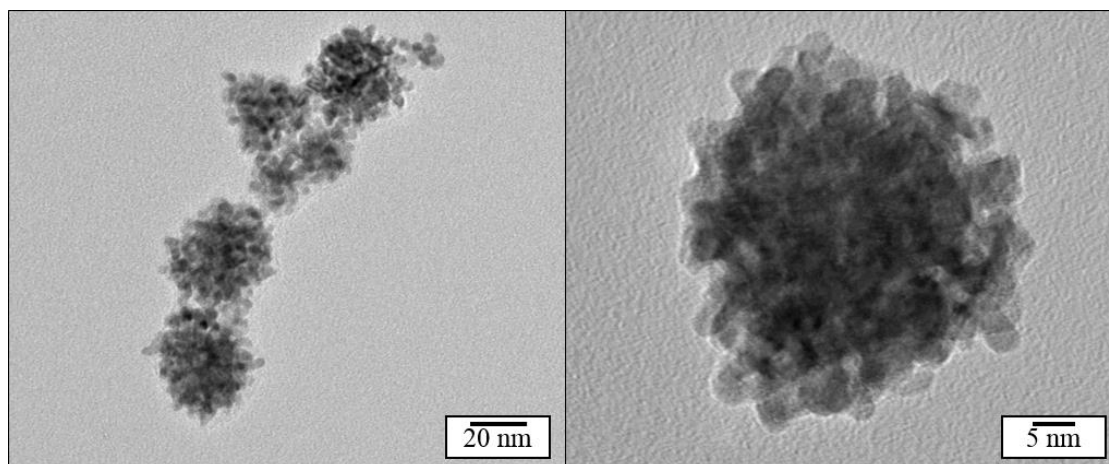


Figure 3.10: As-prepared clusters of Pt nanoparticles. The presence of a large number of isolated Pt clusters suggests agglomeration of some clusters happened during drying, not in solution.

The platinum clusters were 25 to 40 nanometers large and were composed of 4 to 5nm grains. TEM measurements (figure 3.10) showed some agglomeration of the Pt clusters. Dynamic light scattering (DLS) measurements were performed on washed and unwashed Pt clusters, shown in figure 3.11. The unwashed radius of ~20nm matches fairly well with TEM images of individual clusters, and the very small peak is due to un-agglomerated particles or remaining seeds from the initial solution. The washed sample, in comparison, produces a far larger size in DLS. As there was no evidence for an overwhelming majority of 50nm+ radius clusters in the TEM images of the washed sample, this size increase is likely due to agglomeration in solution due to the washing procedure. XRD analysis of these as-prepared clusters was also performed (figure 3.12).

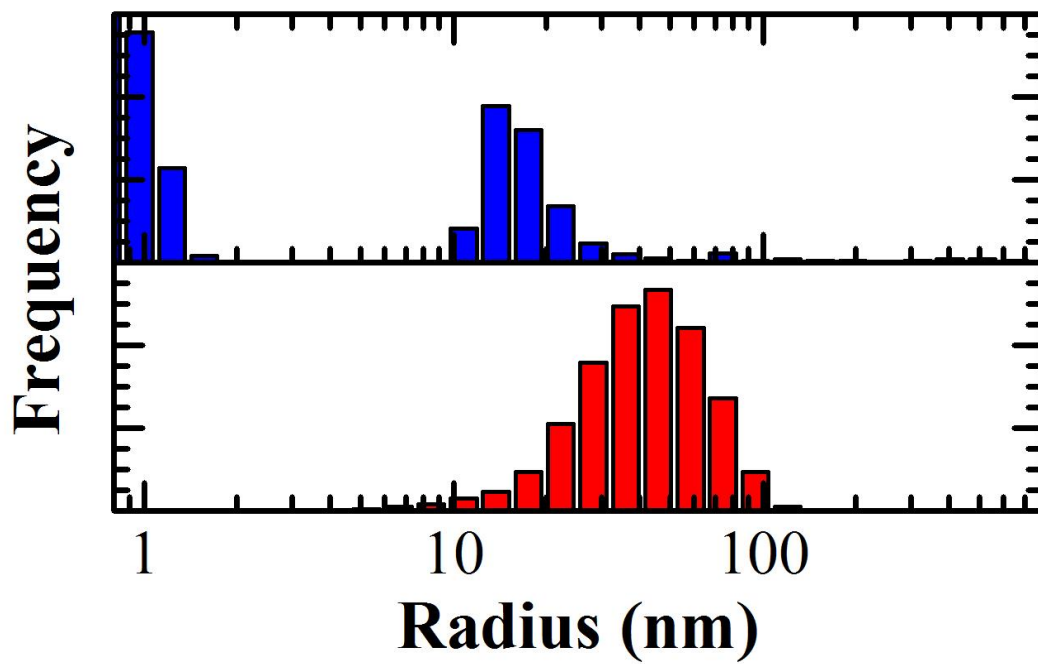


Figure 3.11: Dynamic Light Scattering (DLS) measurements of as-prepared Pt particle sizes before (blue) and after (red) washing in water.

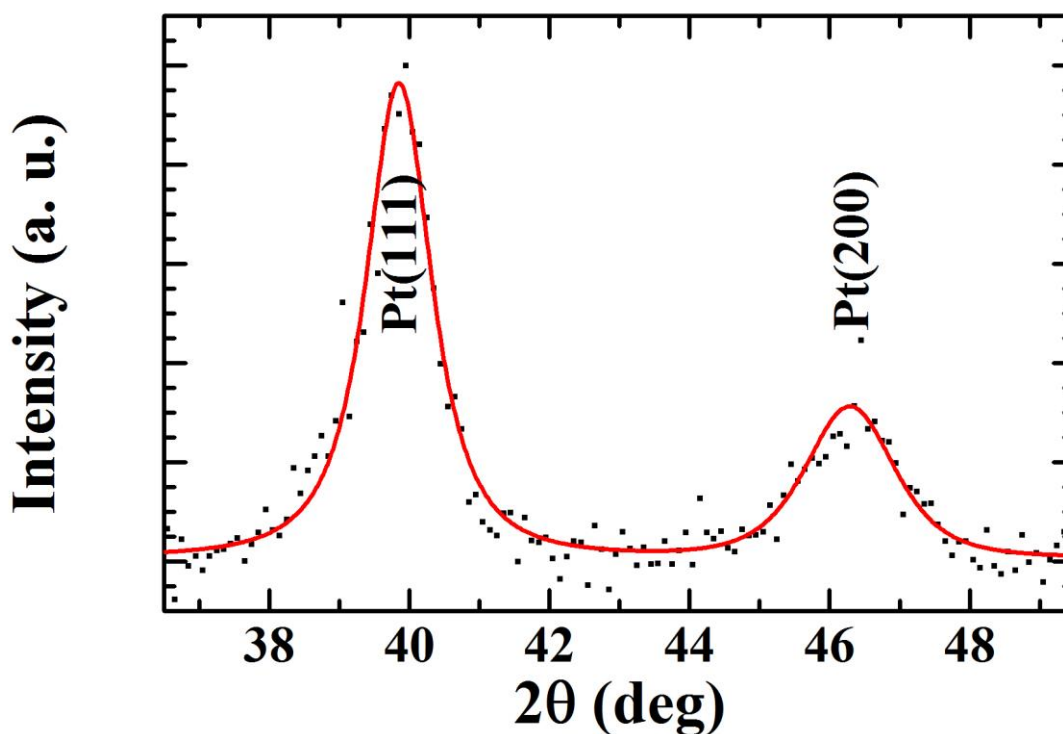


Figure 3.12: X-ray diffraction of as-prepared Pt nanoparticles.

The XRD measurements revealed only the presence of pure elemental Pt, although a monolayer of oxide around the surface of the clusters or gains would not be visible in the XRD measurements. Scherrer analysis of the clusters yielded 7-8nm grain sizes, matching those observed in TEM, confirming the single-grain nature of the particles and the polycrystalline nature of the larger cluster.

3.4.2 Ni/Pt Nanocomposites

The as-prepared Ni/Pt nanocomposites were examined by XRD and TEM. XRD, shown in figure 3.13, revealed no evidence of alloying in this system, but clearly shows the hcp phase of Ni present. The powder did not interact with the

magnetic stir bar during synthesis, suggesting the absence of significant amounts of the fcc phase.

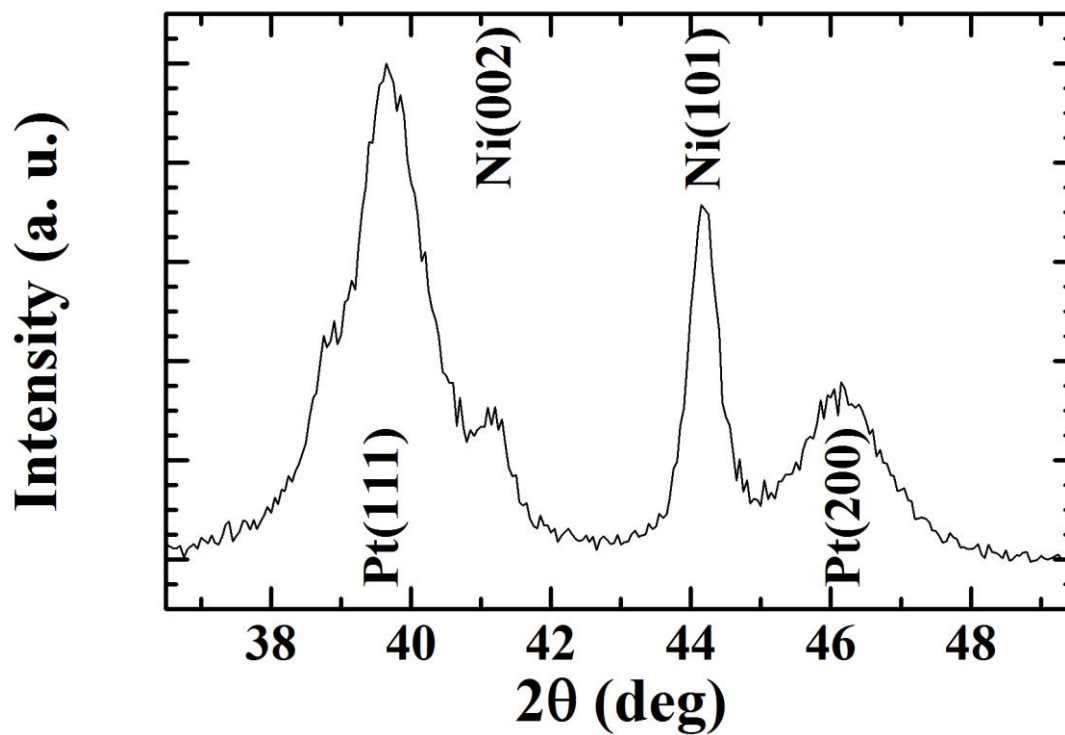


Figure 3.13: As-prepared Pt/Ni nanoparticles. The Pt is in the fcc phase, while the Ni is hcp.

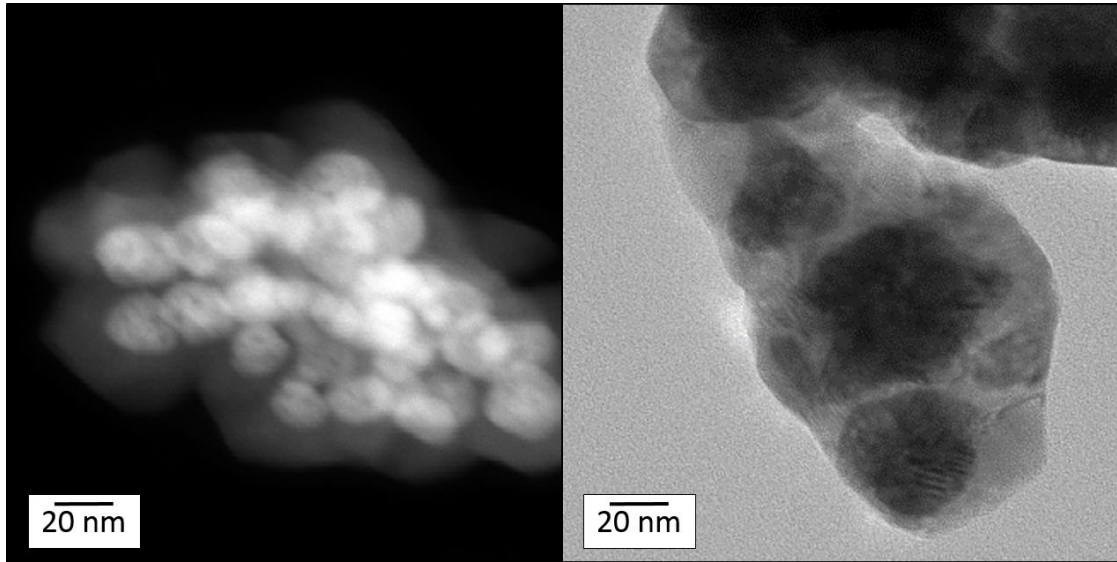


Figure 3.14: Dark field (left) and bright field images of Pt clusters coated with Ni. Dark field images show much larger aligned domains in Pt clusters than the initial 5nm grains. Bright field imaging clearly shows Ni present between at least some Pt clusters.

Figure 3.14 shows TEM images of the Pt/Ni structure. The material was not core-shell, but instead was a collection of agglomerated Pt clusters surrounded by a network of Ni. At these temperatures, the depositing Ni formed a network containing several Pt clusters, rather than distinct shells about single clusters. The dark field images may suggest a large number of the Pt cores are quasi-aligned, although this is not obvious from XRD measurements.

The large, agglomerated nature of the Pt/Ni composite is attributed to two main factors. First, as seen in the Pt cluster size data, there is significant agglomeration during the washing procedure. As the Pt clusters are agglomerated in-solution in larger groups, it is not surprising that the added Ni coats these agglomerates, rather than individual isolated clusters. A second cause is the high temperature of the reaction. As

temperatures at 230°C or above are required to synthesize the non-magnetic hcp Ni phase, during the synthesis process any individual core-shell structures that do form will likely sinter together, producing the connected networks seen here.

Unfortunately, without the addition of extra surfactants there was no way to synthesize separated Pt/Ni core/shell particles via this approach. The standard synthesis technique of slowing down the reduction of Ni to create smaller particles led to the fcc phase of Ni, rather than the desired hcp phase. Investigation of lower temperature synthesis of hcp Ni and the synthesis of hcp Ni core/fcc Pt shell particles is an ongoing project.

3.4.3 Pump-probe sample preparation

Pump-probe measurements required a special sample preparation procedure. Due to the large surface area required for measurements of irreversible processes, samples for these studied were deposited with large surface areas on glass slides. The deposition of large, uniform surfaces of nanoparticles has been widely studied [63-66]. One such technique exploits surface charge effects in metallic nanoparticles to drive the samples to a liquid-liquid interface [67], a technique widely used for a variety of metallic films [68, 69]. For this work a modified method developed for gold nanoparticle films was used [70].

After the synthesis and subsequent washing of Pt nanoparticles as detailed above, the particles were concentrated by a factor of three in deionized water. A standard glass microscope slide was cleaned by washing with ethyl alcohol and acetone. Cleaned glass slides were stored in ethanol and dried before use. 10mL of the metal nanoparticle aqueous solution was poured over the cleaned glass slide in a custom made Teflon trough. This trough contained channels cut into the bottom

covering an area slightly larger than the glass slide, and a hole in the center to allow liquids to drain without removing the glass slide. On top of the water solution, 10mL of hexanes were added. The immiscible hexanes formed a liquid-liquid interface with the water. Finally, 5mL of ethanol was dripped into the trough over 10 minutes. During this addition, the metal particles accumulated at the interface, forming a film-like assembly. An example of this assembly is shown in figure 3.15. The film in this figure was made in a crystallizing dish rather than the Teflon trough to allow for a clearer picture.

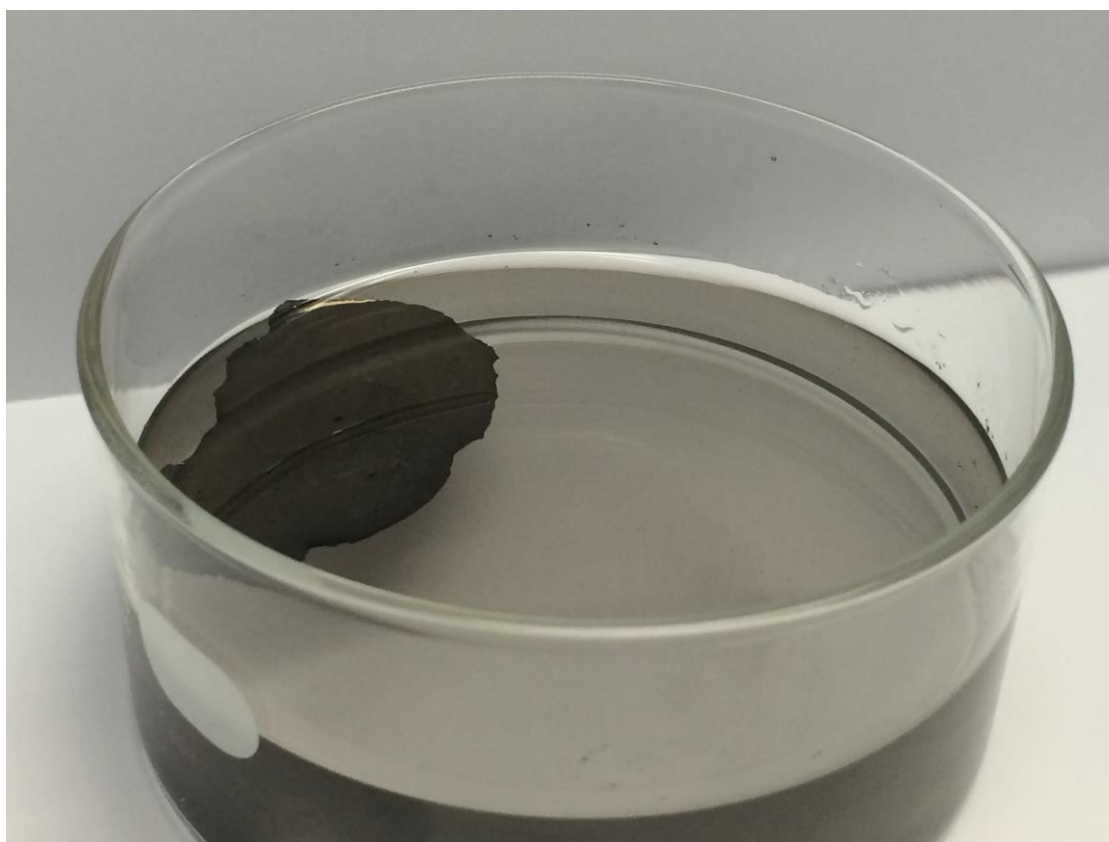


Figure 3.15: A monolayer of Pt nanoparticles at a water-oil interface. A glass crystallizing dish was used for this picture rather than the Teflon trough to make the effect easier to see.

After adding the full 5mL nearly the entire interface was covered by particles. The water/ethanol mixture and hexanes were drained through the hole in the bottom of the trough. As the solution drained, the film was pulled onto the slide by surface tension effects at the water/hexanes interface. The layer of particles remained on the surface of the glass slide with a thin layer of water, which dried, depositing the particles on the glass (figure 3.16).



Figure 3.16: Pt on a glass slide in the Teflon trough. The slide was dried in the trough for several hours before removing.

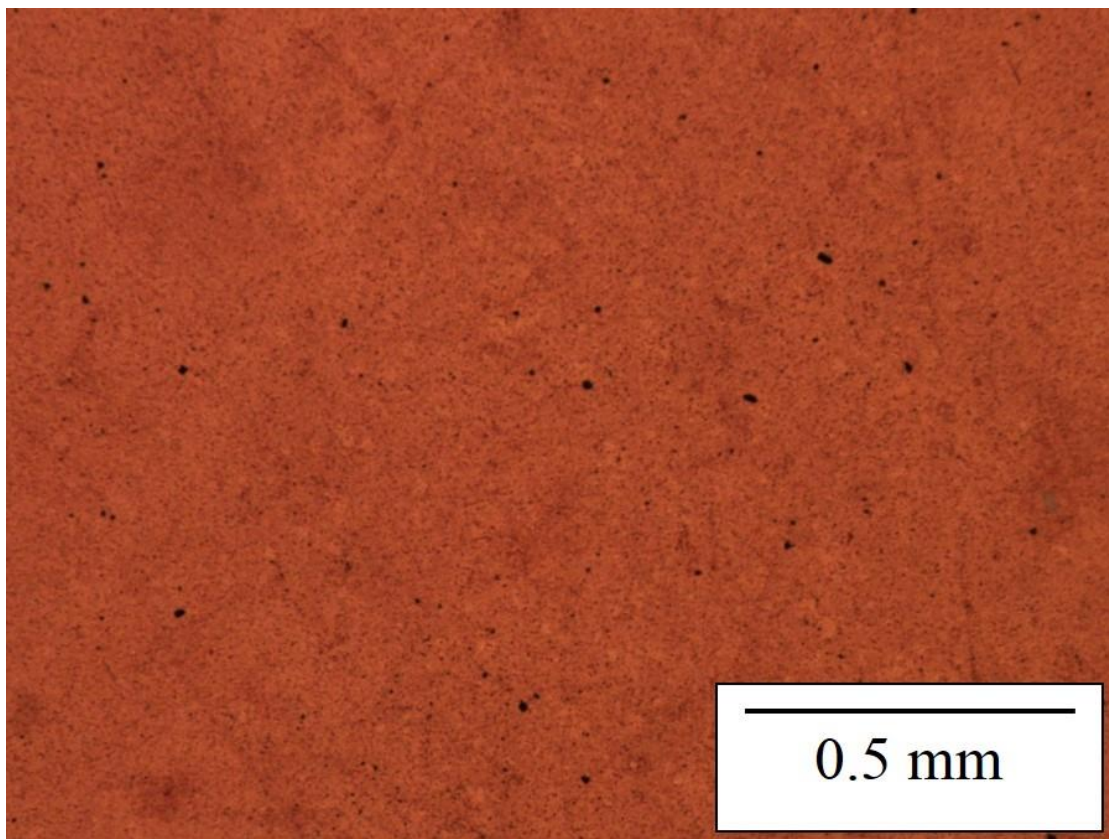


Figure 3.17: Optical microscope image of a Pt particle thin film.

Once the film dried, optical microscopy was used to check for large cracks in the film surface (figure 3.17). Although some cracks are visible on the surface of the slide due to the final water drying step, the overall coverage was quite dense and well suited to pump-probe measurements, in which measurement areas are only 100s of microns on a side.

Atomic Force Microscopy (AFM) measurements were used to test the thickness and uniformity of the film. To create a sharp edge suitable for measuring thickness, a razor was scraped across the surface of the film and displaced particles were removed using compressed air (figure 3.18).

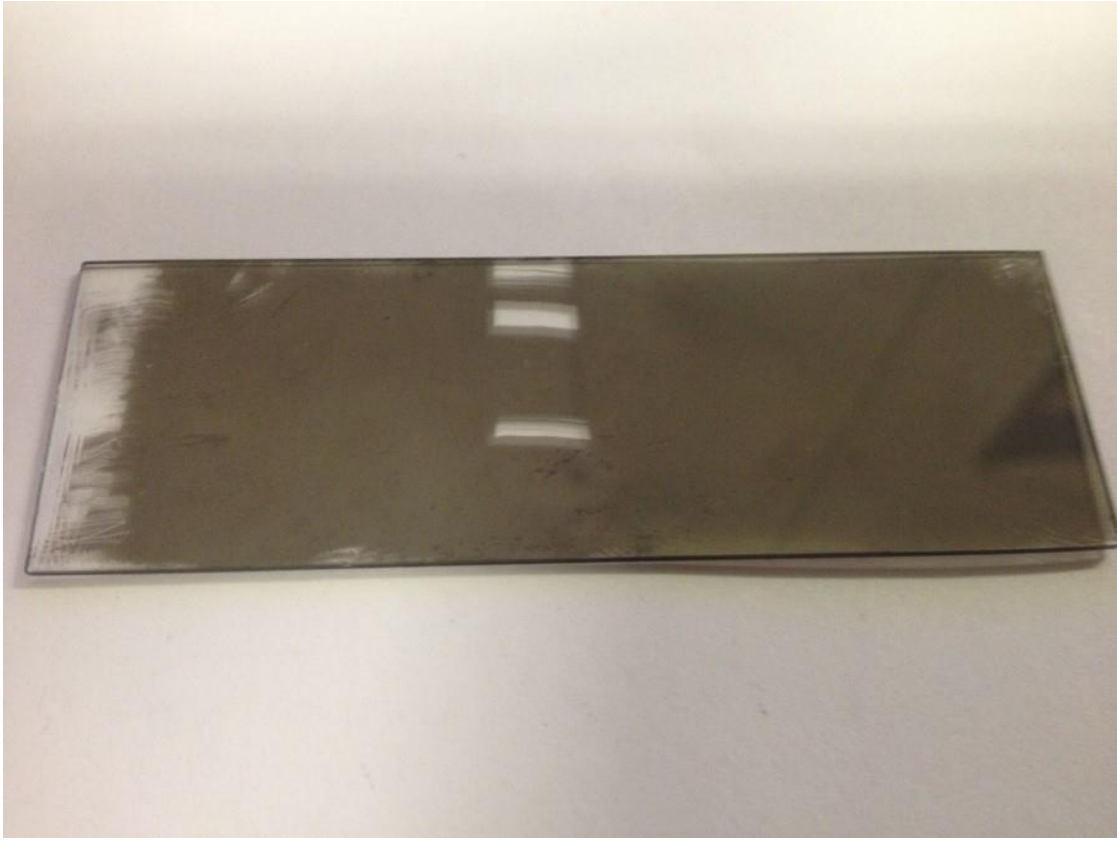


Figure 3.18: A sample used for AFM measurement. The clear areas in the middle were cleaned by scraping with a razor, and provided excellent contrast for film thickness measurements.

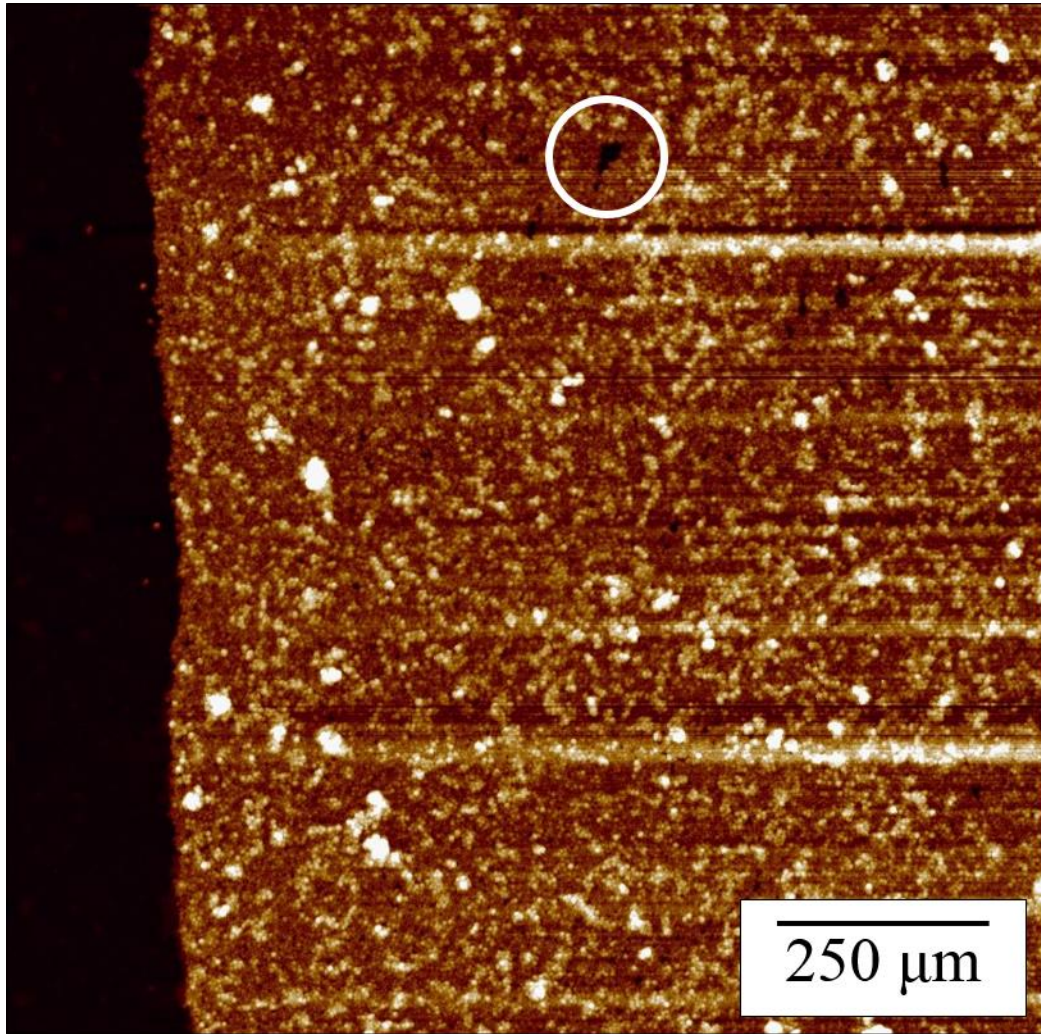


Figure 3.19: A topographical map of an as-prepared film of Pt nanoparticles. Black spaces signify no Pt coverage. A gap in coverage is circled in white.

These measurements were used to check two properties of the film: spacing between particles and thickness of the film. AFM imaging (figure 3.19) showed the particles were densely deposited. Several gaps are visible in the film, with average dimensions far less than the spot size of pump-probe XRD measurements. Streaks in

the image were artifacts of the AFM measurement and were not indicative of sample thickness variations.

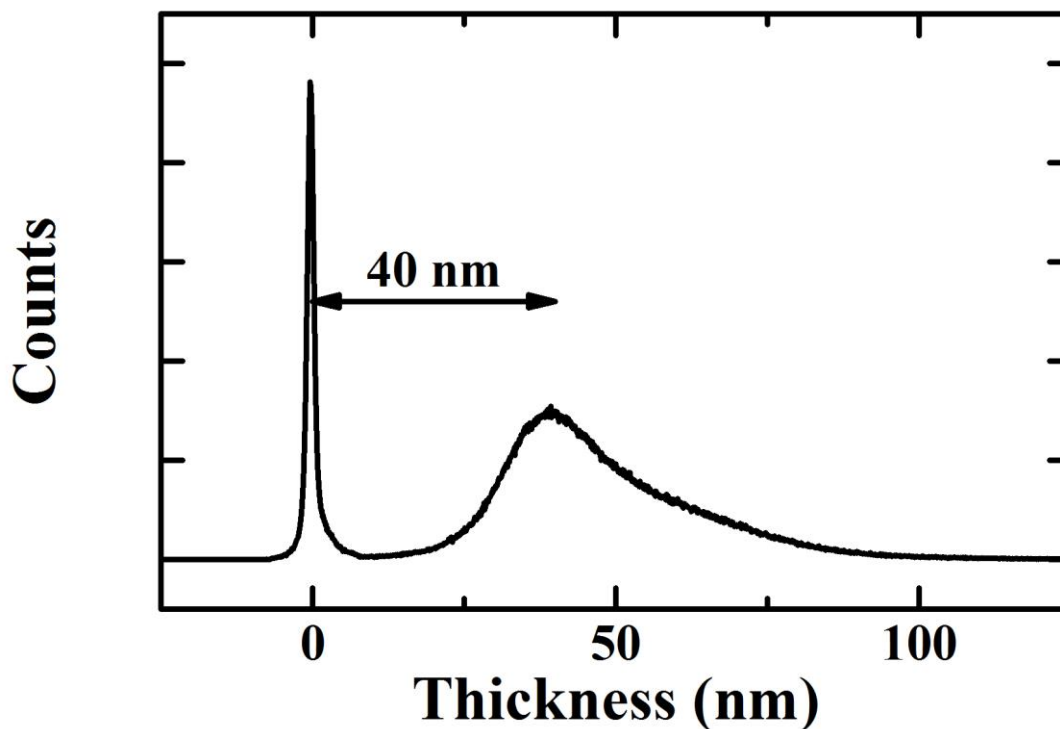


Figure 3.20: AFM measured heights of a sample slide. The two peaks are the surface of the slide (narrow) and the surface of the Pt film (broad), while thicknesses are measured relative to the glass surface.

Sample heights measured from the same field of view (figure 3.20) showed two distinct peaks. The narrow peak was the surface of the glass slide. The second, much broader peak, was the height of the surface of the Pt particles. The thickness of the film was approximately 40nm, corresponding to roughly a monolayer of Pt particles. The tail on the right of the higher peak signified a non-uniform thickness, and there were likely portions of the film that were a bilayer rather than a monolayer.

The overwhelming majority of the surface area, though, was roughly a monolayer and would heat uniformly under laser excitation.

Although measurements of the effects of aging and solution pH on the film quality are ongoing, some basic measurements of the effect of changing the ethanol volume added have been performed. For these measurements, the amount of Pt in the film was quantified by measuring the amount remaining in solution after the synthesis process.

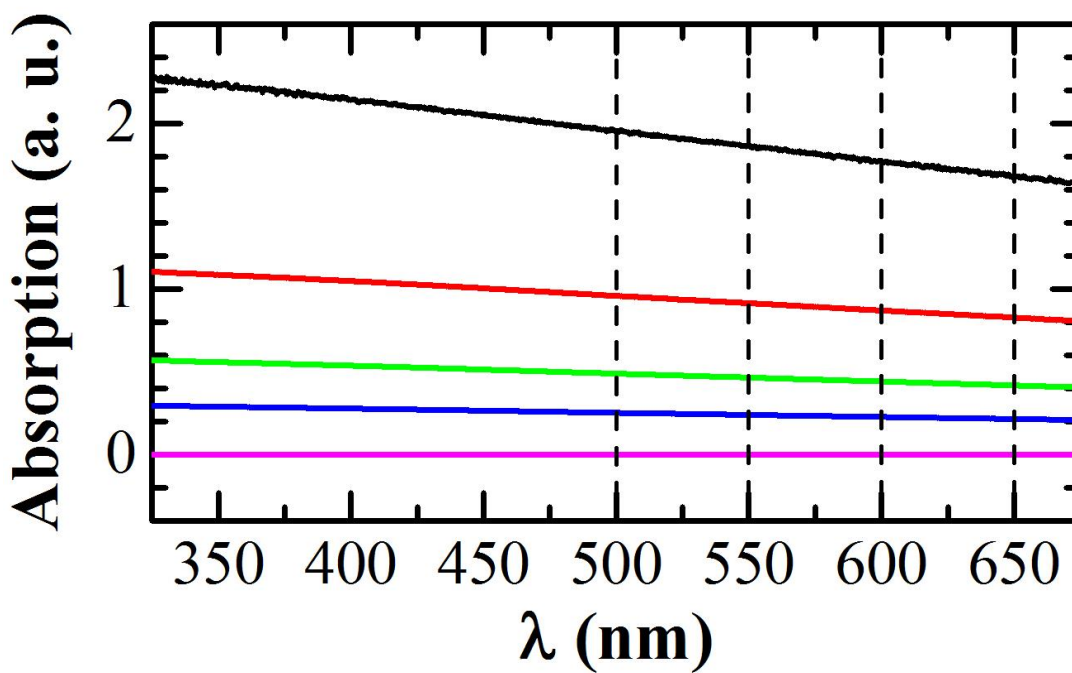


Figure 3.21: An example of testing for the concentration of Pt remaining in solution after making a “monolayer” film. Measurements were made at the initial concentration (black), 1/2, 1/4, 1/8, 1/16, and 1/32 (pink) concentrations. The dotted lines mark “slices” at the wavelengths used for the subsequent Pt concentration measurements.

To begin, a series of dilutions of the aqueous Pt solution were measured using ultraviolet-visible spectroscopy (UV-vis). These measurements determine the absorption of a liquid as a function of the wavelength of incident light, and in this case provide particle density information. The results of a sample series of dilutions are shown in figure 3.21. Using these dilutions as a calibration, the absorption of the remaining solution after making a monolayer film could be used to quantify the Pt remaining in solution. Calibration runs were performed for each batch of Pt particles used, to control for particle density fluctuations between synthesis batches.

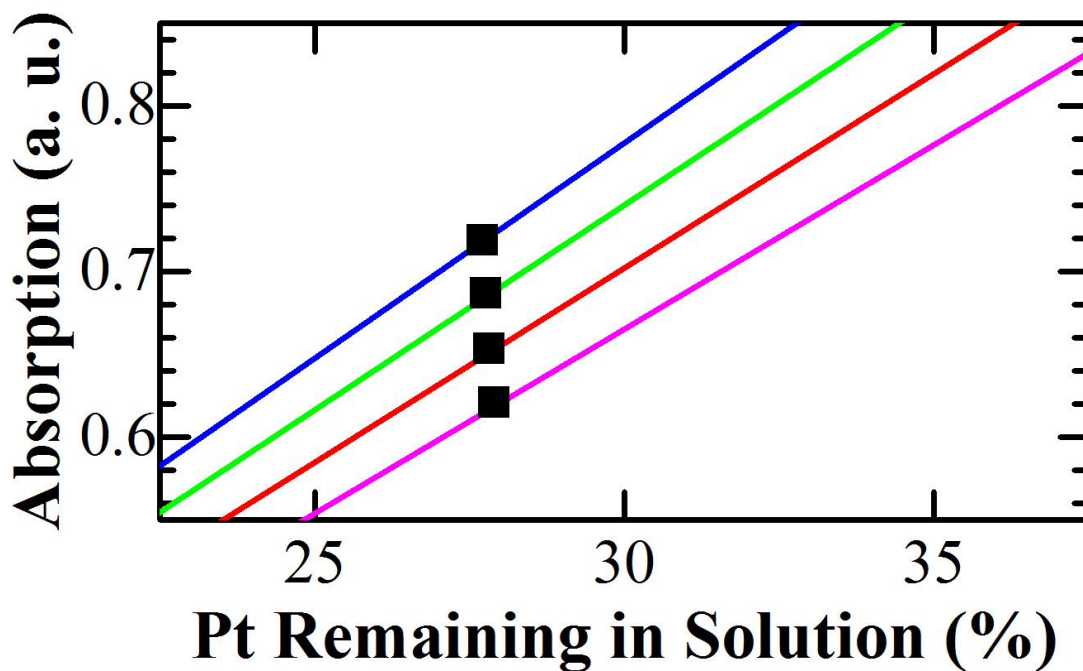


Figure 3.22: The absorption at 500, 550, 600, and 650nm of the remaining Pt solution after making a film using 7.5mL of ethanol.

The absorption at 500nm, 550nm, 600nm and 650nm was used to calculate the remaining Pt after film synthesis was completed (figure 3.22). This provided a large range of incident wavelengths to fit, while not approaching the lower wavelength ranges in which absorption from the water and cuvette dominate.

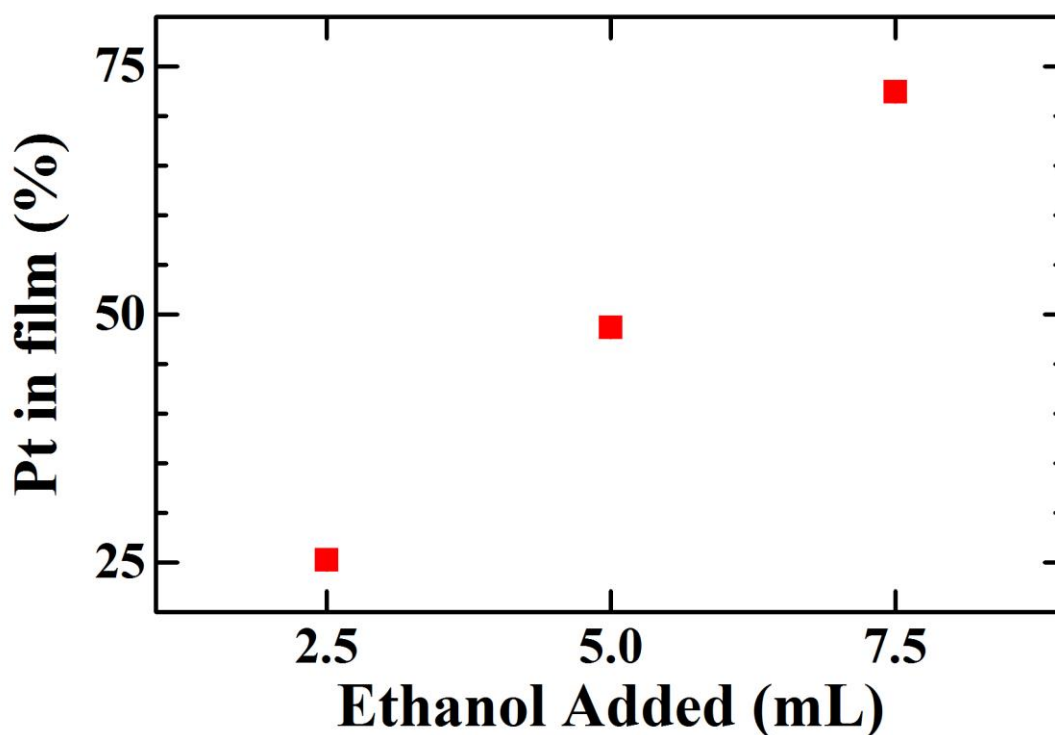


Figure 3.23: The measured ethanol dependence of the amount of Pt removed from the solution during the film-making process. Error bars are smaller than the symbols.

Three film synthesis runs were performed using 50%, 100% and 150% the normal amount of ethanol. In each case UV-vis measurements were performed on the remaining material, and the remaining Pt was calculated as described above. These measurements showed a clear correlation between the amount of ethanol used and the

amount of Pt in the film (figure 3.23). The amount of alcohol added is clearly a strong influence on the amount of Pt present in the film. Research to better understand the role of other properties of the Pt, such as the charge of the Pt clusters and the pH of the solution, is ongoing.

Chapter 4

THE REDUCTION OF SAMARIUM AND COBALT OXIDES TO METALLIC SAMARIUM COBALT ALLOYS

4.1 Synthesis

The work on Samarium Cobalt materials was split into two categories: preparation of the precursor with the desired properties, and subsequent reduction of those precursors. This work discusses the method used to synthesize the precursor, a discussion of the characterization of the material, and a discussion of the experiments used to test the energetics of the oxidation and reduction reaction used.

This experiment was performed with help from Ronald Cichocki, who performed selected TGA measurements and assisted in data analysis.

4.1.1 Autocombustion

This project focused on a bottom-up approach to synthesizing metallic nanoparticles from nanoscale precursor powders. In particular, the precursor consisted of a nanoscale mixture of Sm and Co oxides size-reduced to a sub-micron scale. These oxide particles were then reduced to form the metallic Sm and Co phases.

Autocombustion, a common technique used to produce large volumes of oxides [71-73], was a highly customizable route to synthesizing the desired metal oxides in a finely mixed form without additional mixing steps. The initial Sm to Co ratio set the stoichiometric balance for the rest of the process, and was typically varied from 2:17 to 4:17 Sm:Co, although 1:1, pure Sm, and pure Co precursors were also synthesized. Sm-rich precursors were commonly used when compared to the 2:17 and 1:5 desired final phases, as the reduction reactions were less efficient for Sm than Co.

For this process, Sm and Co nitrates were mixed in aqueous solution with citric acid, a fuel. The quantity of fuel was varied from 0.7 to 1.3 times the ideal (oxygen-neutral) amount, but generally run in a fuel-rich stoichiometry. Varying the amount of fuel controlled the temperature and speed of the reaction. The solution was heated in a quartz vessel over a hotplate set above 200°C. As water evaporated, the remaining solution formed a gel, and after a critical volume of water was removed the gel smoldered and ignited. The reaction front propagated through the entire gel and left a low-density ash behind. This ash consisted of crystalline Co_3O_4 and a small amount of SmCoO_3 in addition to an amorphous Sm-containing component, and included carbon-based residues that acted as a sticky contaminant.

4.1.2 Calcination

A subsequent calcination step at 700°C converted the amorphous component to SmCoO_3 and removed the remaining contaminants. The as-prepared ash was measured by XRD, as were the products of an intermediate and high-temperature calcination (figure 4.1). The product of the calcination step was a clearly defined combination of Co_3O_4 and SmCoO_3 . The exact composition was determined by the initial Sm:Co stoichiometric ratio. The oxides formed a low-density plate-like structures hundreds of microns large and several microns thick (figure 4.2).

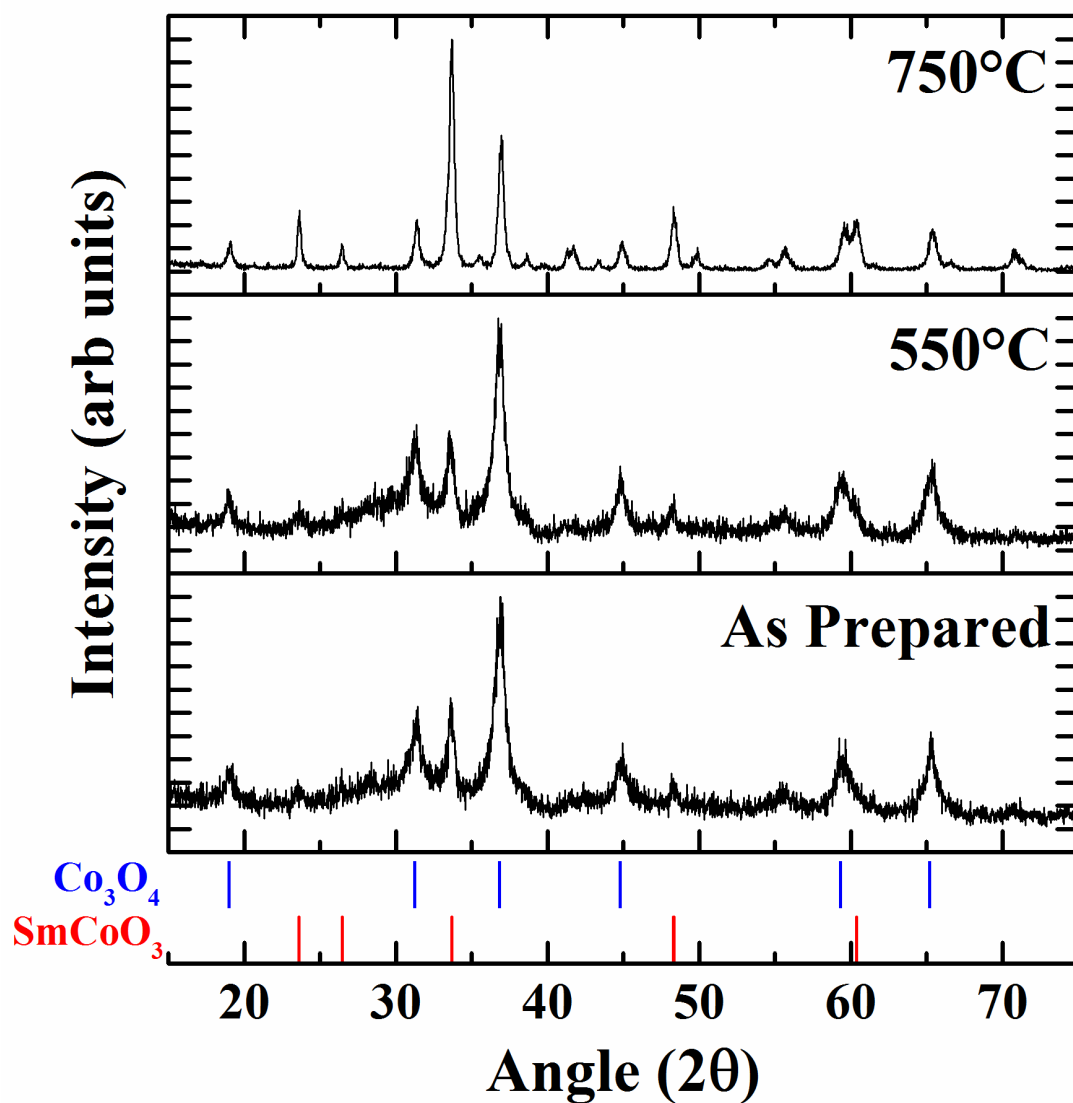


Figure 4.1: Sm-Co-O oxide precursor, as-combusted and following a 2 hour calcination at 550°C and 750°C. The initial phase was dominated by Co_3O_4 with some evidence of crystalline SmCoO_3 , while the final phase contained only the two oxides. Reference peak position sticks are provided for the most intense peaks of each phase.

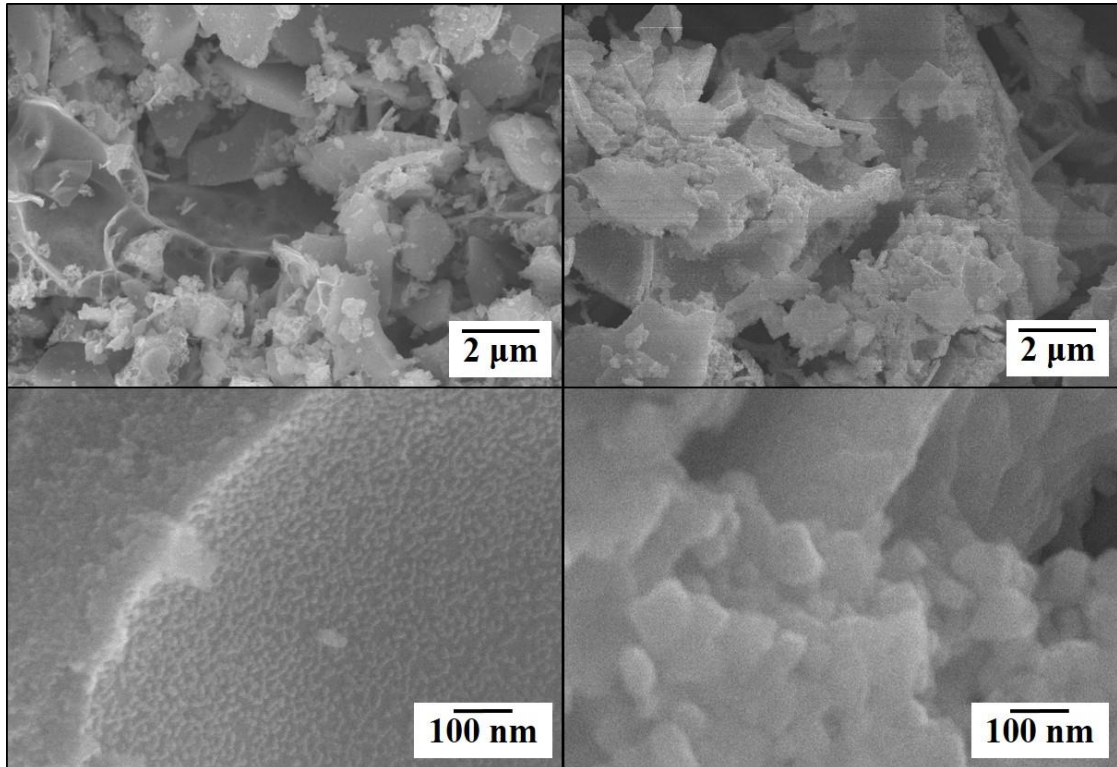


Figure 4.2: Molar ratio Sm:Co 2:17 precursor oxide, before (left) and after (right) a 700°C/2h calcination step. There is no obvious separation of the SmCoO_3 and Co_3O_4 phases of the material.

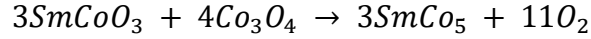
4.2 Reduction

The reduction of Sm-Co oxides to metallic Sm-Co alloys was measured via oxidation-reduction reactions. Many of the reductions were performed in-situ in a thermogravimetric analyzer (TGA) using forming gas as a reducing agent. Supporting measurements required a variety of other reduction techniques and environments.

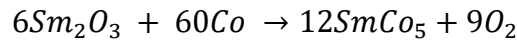
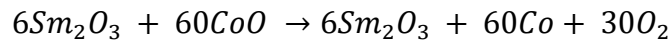
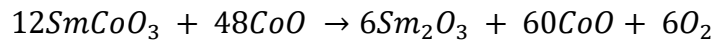
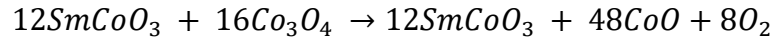
4.2.1 Reduction Pathway

The initial phase was a combination of SmCoO_3 and Co_3O_4 that could be tuned by the stoichiometric ratio of Sm and Co nitrates used for the autocombustion process. The reduction pathway for these oxides was studied primarily by DSC through

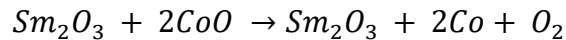
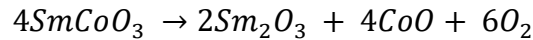
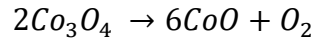
reduction in a variety of conditions, as well as XRD on the reduction products. The balanced stoichiometric equation for the reduction process when forming SmCo₅ was



Similar expressions could be written for any final Sm-Co alloy. There were several intermediate steps in the reduction of these oxides. The complete pathway by which the SmCo₅ alloy forms was



These reaction steps were measured individually in this work. To this end, pure SmCoO₃ and Co₃O₄ samples were synthesized via autocombustion, rather than a mixture. This simplified the examined reduction pathways. The measured reactions were as follows.



The first two reductions were measured using the pure Co₃O₄ precursor, while the second pair were measured using the pure SmCoO₃ precursor.

4.2.2 Reduction Environments

TGA measurements were performed in N₂ and 95%N₂/5%H₂ forming gas atmospheres. In each case the atmosphere was flowed at a constant rate of

100mL/min. Bulk lab gas lines were used to supply N₂ and a gas cylinder was used for the forming gas.

4.2.3 Sample Sizes

These measurements were performed on 10-50mg of powder oxide. The mass used depended on the density of the powder. The densest samples were purchased or ball-milled, while as-annealed samples were far less dense. Exploratory measurements were performed on varying masses of samples to examine mass dependence of our signals, but data sets to be explicitly compared using isoconversional analysis were taken using similar masses of powder. Samples were held in alumina pans for measurement (figure 4.3), and the same pan was used for repeated measurements to control for as many external influences as possible.



Figure 4.3: Sample cups and paddles for DSC measurements

4.3 TGA Measurements

The activation energy measurements for each of the conversions are described below. In every case, the explanation begins with the experimental details specific to that conversion, including the specific temperature sequence and range of isothermal temperatures. The results of the isoconversional measurements follow, and finally an analysis of the data including the calculated activation energy is given.

4.3.1 Co_3O_4 measurements

The reduction of Co_3O_4 to Co metal was studied in forming gas below 350°C . The conversions of Co_3O_4 to CoO and the subsequent CoO to Co metal could not be

separated, but estimations of the activation energies could be made by examining different regions of the conversion. In general, conversions below 25% corresponded to the initial $Co_3O_4 \rightarrow 3CoO + O$ conversion, although there was likely some conversion of CoO to Co before the initial step completed.

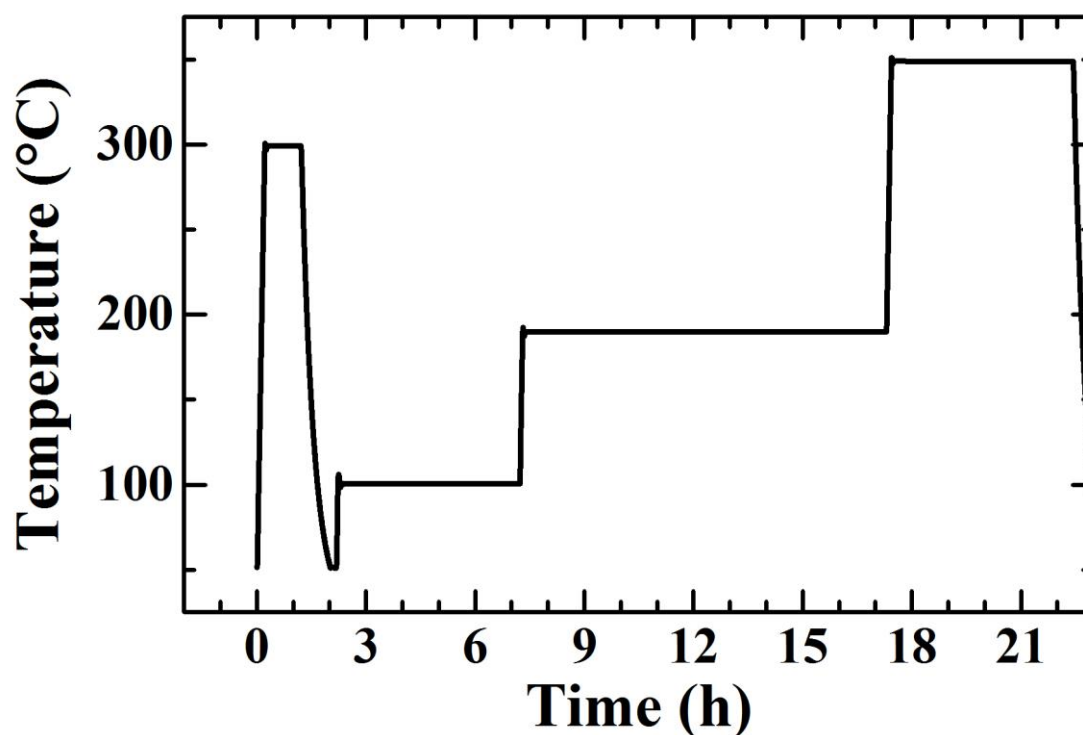


Figure 4.4: The heating profile for an example Co_3O_4 conversion measurement with an isotherm of interest at $190^\circ C$. The initial $300^\circ C$ isotherm was in N_2 , while the subsequent $100^\circ C$, $190^\circ C$, and $350^\circ C$ steps were in forming gas.

These measurements contained 4 distinct isotherms, and the heating profile is shown in figure 4.4. A preliminary $300^\circ C$ step in N_2 was used to clean organic contaminants and adsorbed water from the sample. Following a cooling step to room

temperature and atmospheric change to forming gas, an isotherm at 100°C for 5 hours was used to determine initial sample mass. The sample was then ramped at 20°C/min to the temperature of interest for a 10 hour isotherm. Following this, a 5 hour isotherm at 350°C was used to determine the final sample mass after complete conversion to Co metal. The mass evolution observed in this sequence is shown in figure 4.5.

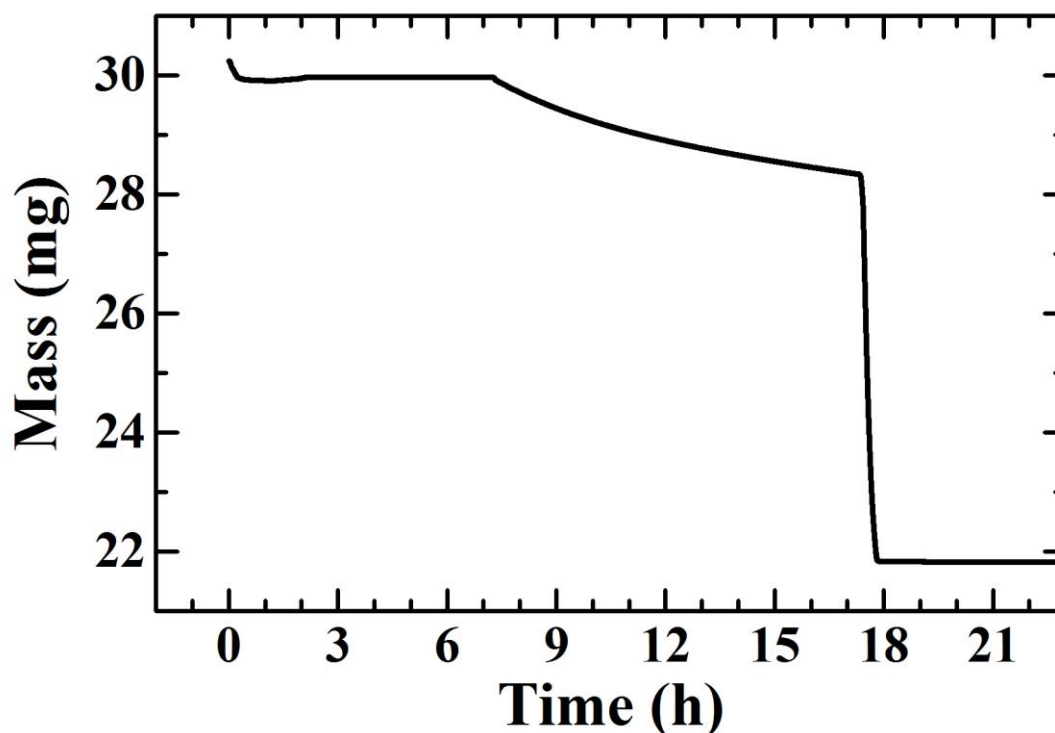


Figure 4.5: The mass evolution of a Co_3O_4 sample undergoing the above 190°C measurement sequence.

For the remainder of this section, the time $t=0$ refers to the beginning of the isotherm of interest. This time was chosen to be the time at which the sample temperature reached the temperature of interest. Although a small overshoot and

subsequent temperature oscillation was observed in each case, the time during which the temperature was unstable was small compared to the measured times.

Isoconversional measurements were taken at temperatures from 185°C to 250°C (figure 4.6). There was a clear two phase behavior in these samples.

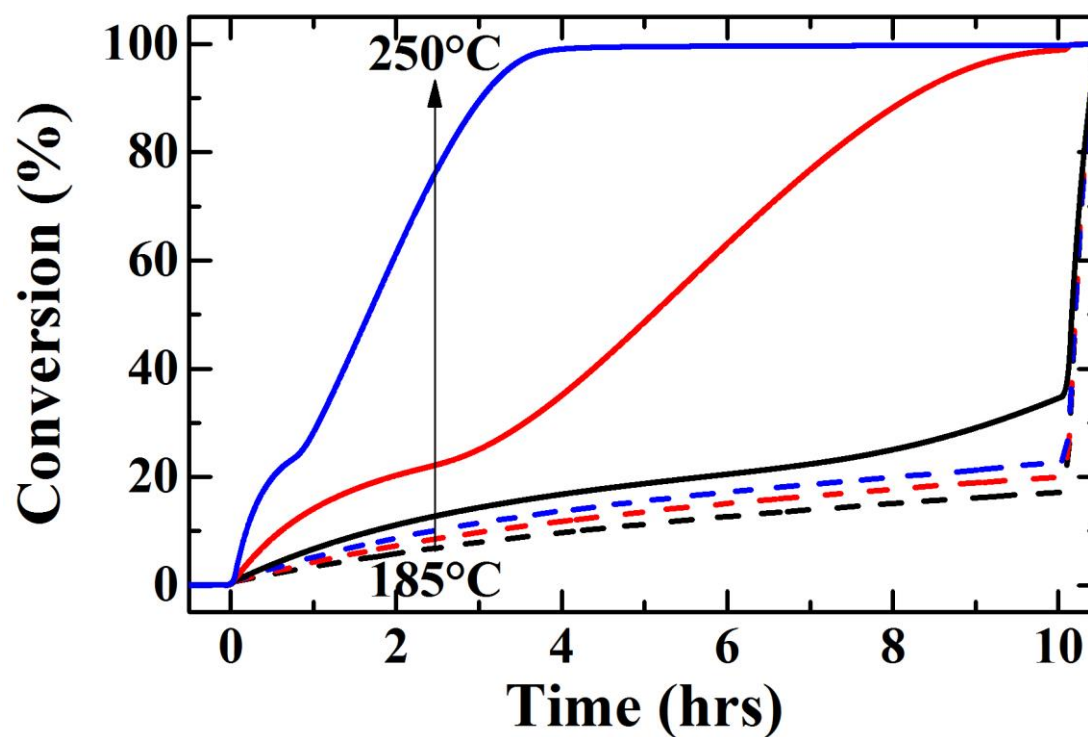


Figure 4.6: Selected sample conversion data for the Co_3O_4 to Co reaction. Isothermal temperatures of 185°C, 190°C, 195°C, 200°C, 220°C and 250°C are shown.

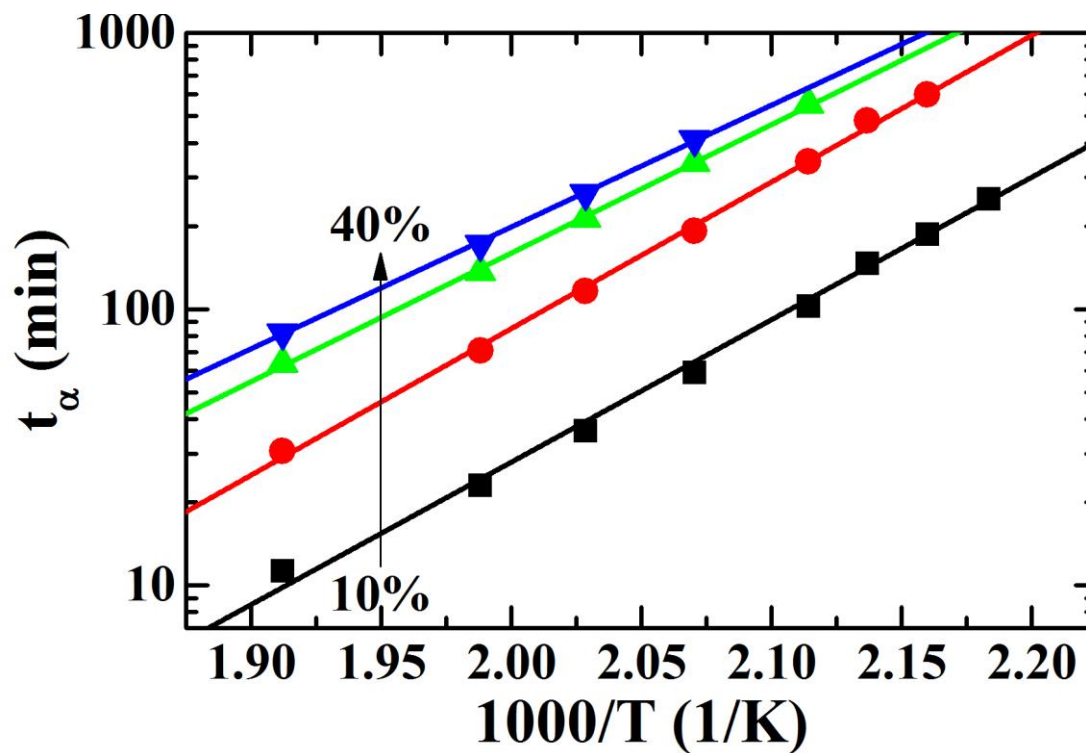


Figure 4.7: The Arrhenius plot for the 10%, 20%, 30% and 40% isoconversional slices.

From the conversion measurements, it is clear the second phase of conversion occurs at approximately 25% of the total conversion, as expected. Isoconversional analysis was performed in 5% increments starting at 10%. This data is shown in figure 4.7. The isoconversional plots change slope dramatically above 20%. To estimate the activation energy of the Co_3O_4 to CoO conversion, the energy calculated from the 10%, 15% and 20% conversions was averaged. This data and several higher conversions are shown in figure 4.8.

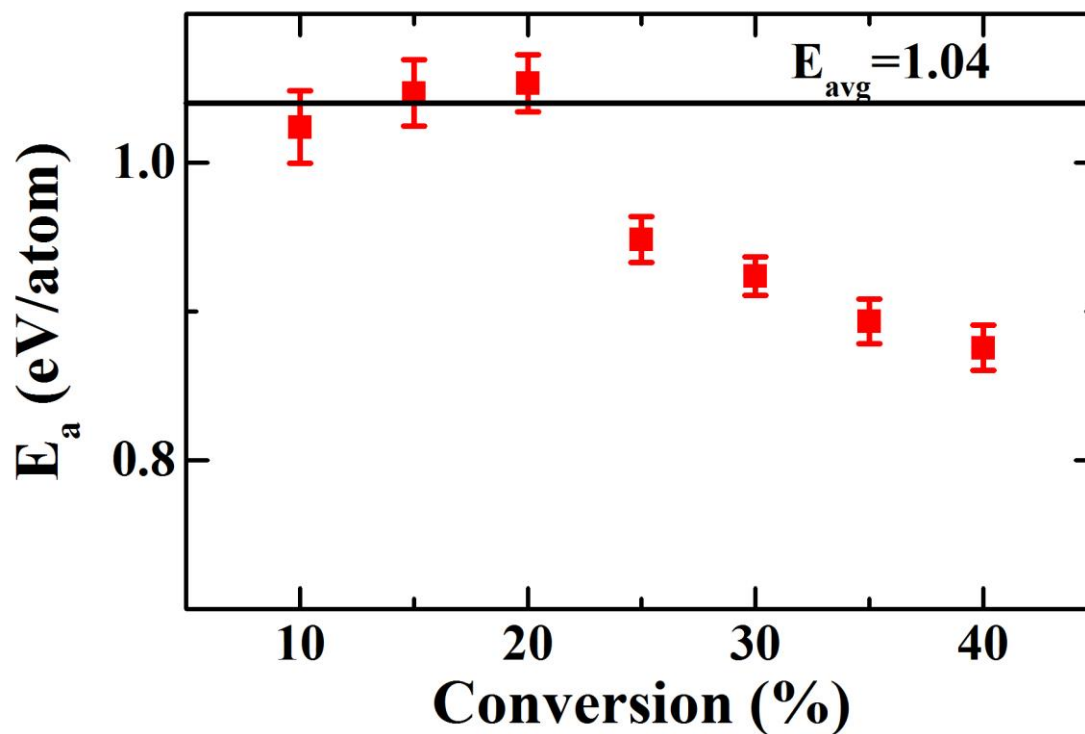


Figure 4.8: A selection of activation energies calculated from these isoconversional measurements. The first three average to an activation energy of 1.04 eV/atom. Higher percentages of conversion combine effects due to both reactions.

The activation energy for the nanoscale Co_3O_4 to CoO conversion was approximately 1.04 eV/atom. Although calculating the activation energy for the CoO to Co conversions was not possible from this data, it does appear to be significantly smaller than the activation energy for the initial reaction. For reference, the bulk activation energy for the CoO to Co transition is 0.477-0.607 eV/atom [74].

4.3.2 SmCoO₃ measurements

Two transitions in the SmCoO₃ system were examined in forming gas at temperatures below 500°C. The conversion from SmCoO₃ to Sm₂O₃+CoO occurred at temperatures between 150°C and 350°C, while the conversion of the CoO portion of the oxide to Co metal occurred above 350°C. Special care was taken to ensure the conversions were examined individually, and these transitions are analyzed independently in the following sections.

4.3.2.1 SmCoO₃ to Sm₂O₃+CoO

This transition was studied between the temperatures of 240°C and 300°C. A sample temperature sequence and mass evolution are shown in figures 4.9 and 4.10, respectively. Three separate isotherms were used in these measurements. The first isotherm lasted 5h at 300°C in N₂ atmosphere and served to clean the oxide. Following this isotherm, the temperature was lowered to 50°C and the atmosphere was changed to forming gas. The system remained at 50°C for several minutes to complete the change from a N₂ to a H₂ atmosphere. The system was then ramped directly to the temperature of interest, and held at that temperature for 10 hours. A final 5 hour isotherm at 330°C followed, and was used to measure the post-conversion mass.

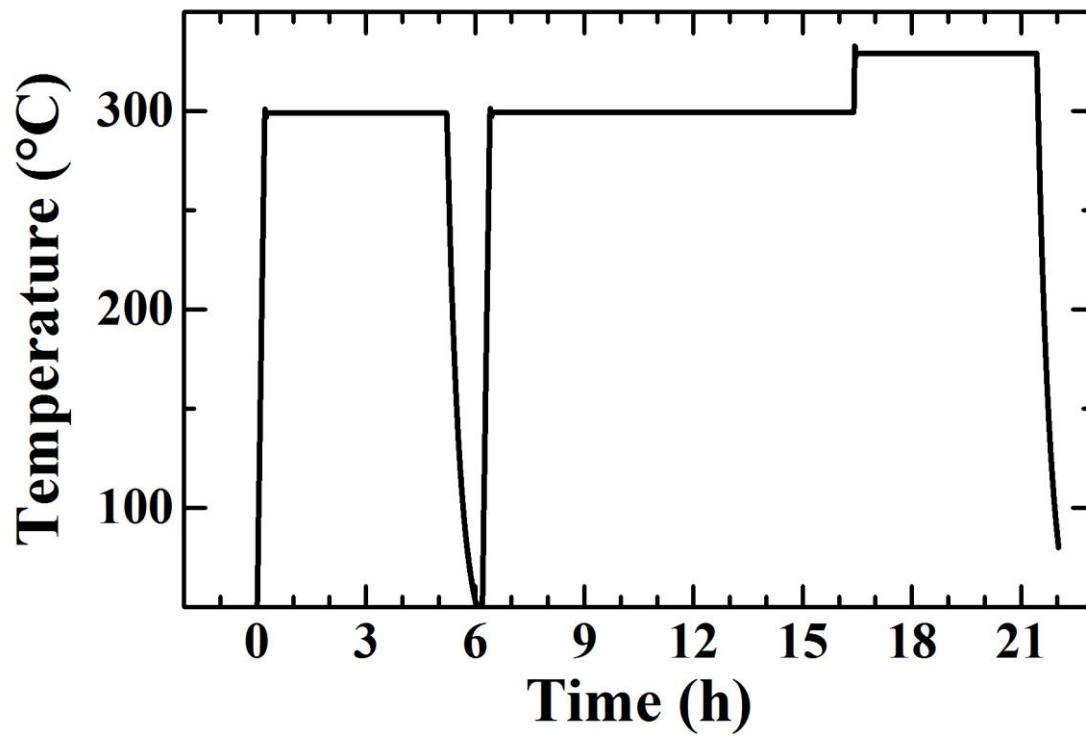


Figure 4.9: The temperature profile for a 300°C isotherm. A preliminary 300°C cleaning isotherm was performed in N₂, while the sample was under forming gas for the second 300°C and the 330°C isotherms.

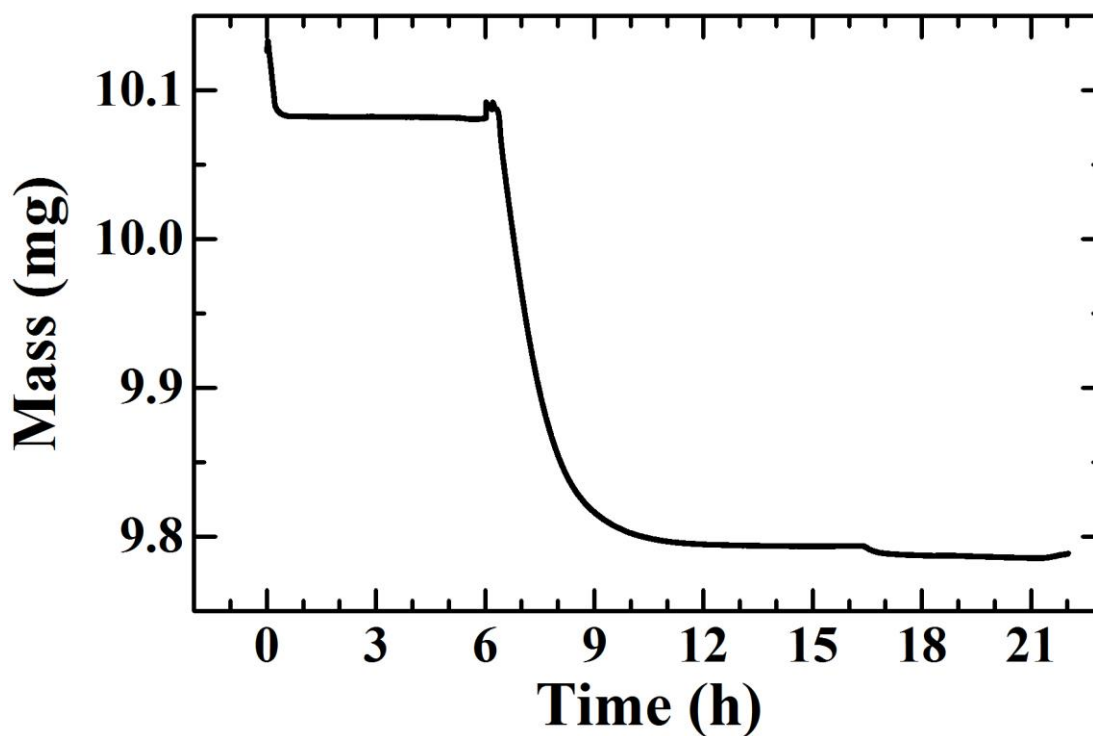


Figure 4.10: The mass evolution during the described temperature sequence. The initial isotherm contained irreversible mass loss due to the cleaning of contaminants, while intermediate and complete conversion were seen in the subsequent FG isotherms.

For consistency, for the remainder of this section and in the following figures the time $t=0$ refers to the beginning of the isotherm. The ramp, therefore, began at a time $t < 0$. In each case, the time $t=0$ was chosen as the time when the sample temperature reached the isotherm temperature. Although there is a slight overshoot of the temperature in each case, these fluctuations took less than 2 minutes.

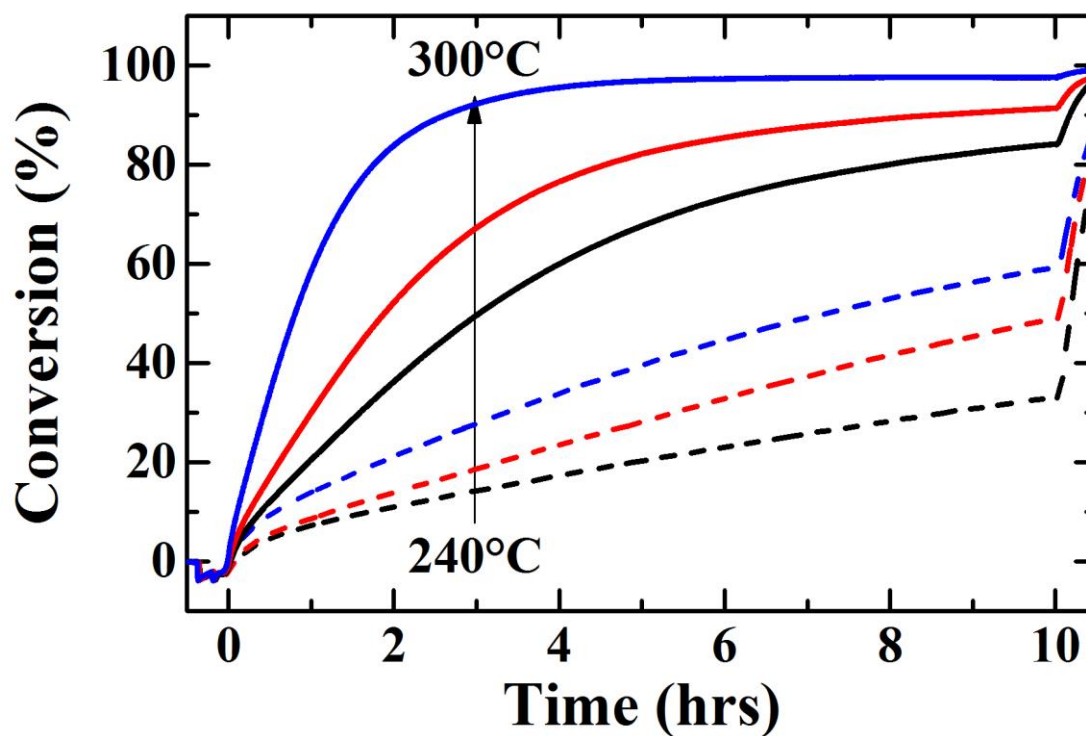


Figure 4.11: The amount of conversion during 10h isotherms at 240°C, 250°C, 260°C, 270°C, 280°C, and 300°C. Time $t=0$ was set as the time at which $T_{\text{sample}}=T_{\text{isotherm}}$ following the ramp from room temperature.

A 10 hour isotherm followed the ramp to the temperature of interest. The conversion (or equivalently, the mass loss) was qualitatively similar for each temperature as shown in figure 4.11. In this case, several of the chosen isotherms completed conversion during the 10 hour data run. A selection of isoconversional analysis plots is shown in figure 4.12, and the extracted activation energy for the SmCoO_3 to $\text{Sm}_2\text{O}_3+\text{CoO}$ conversion is shown in figure 4.13.

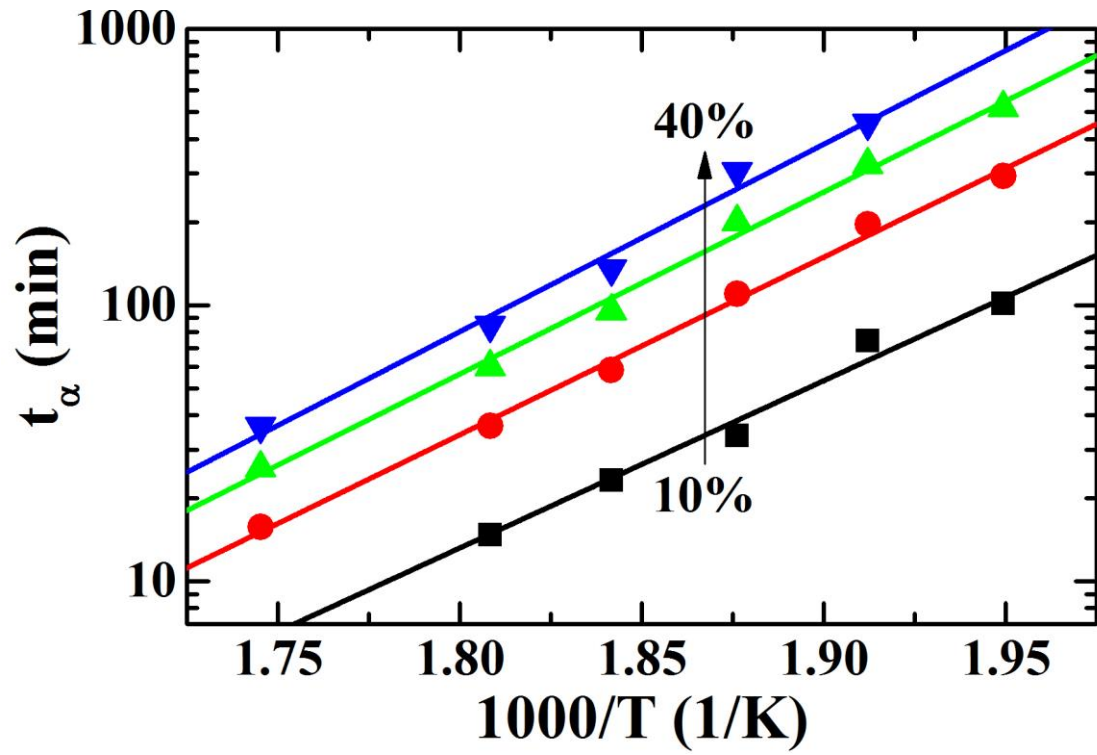


Figure 4.12: The time required to convert 10% to 40% of the SmCoO_3 sample to $\text{Sm}_2\text{O}_3+\text{CoO}$ as a function of the isothermal temperature.

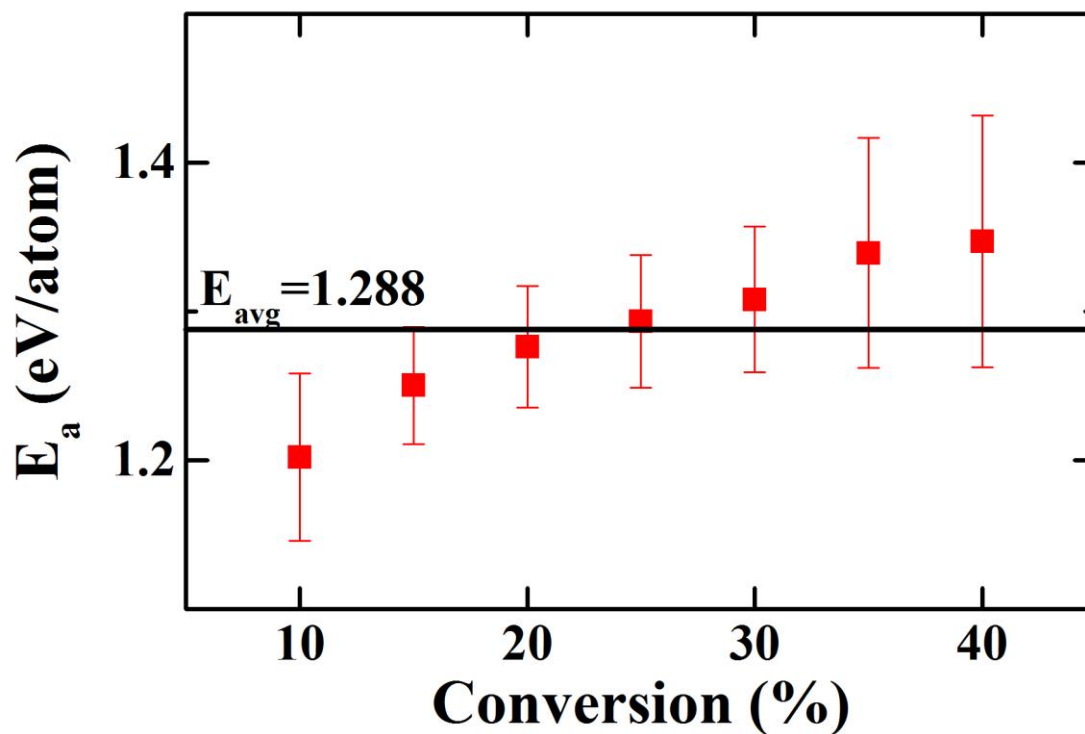


Figure 4.13: The calculated activation energy from each isoconversional slice for the SmCoO_3 to $\text{Sm}_2\text{O}_3 + \text{CoO}$ transition.

The activation energy when compared across each conversion was approximately 1.3eV/atom. There was a systematic increase in the fit E_a with conversion amount, in part due to uncertainties in selecting time 0.

4.3.2.2 CoO to Co in the presence of Sm_2O_3

This transition was studied between the temperatures of 350°C and 410°C. A sample temperature profile used is shown in figure 4.14, and the corresponding mass evolution in figure 4.15.

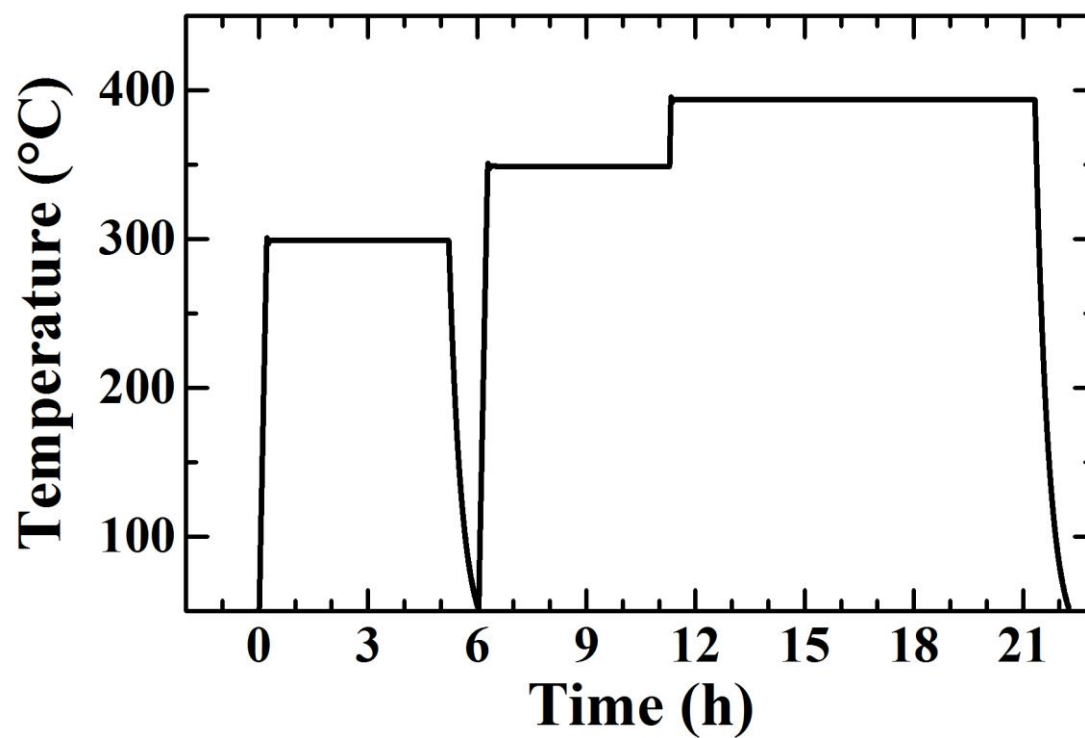


Figure 4.14: The temperature profile to obtain a 395°C isotherm. In this measurement, an intermediate isotherm was used to complete the SmCoO_3 conversion, and the isotherm of interest was the final portion of the experiment.

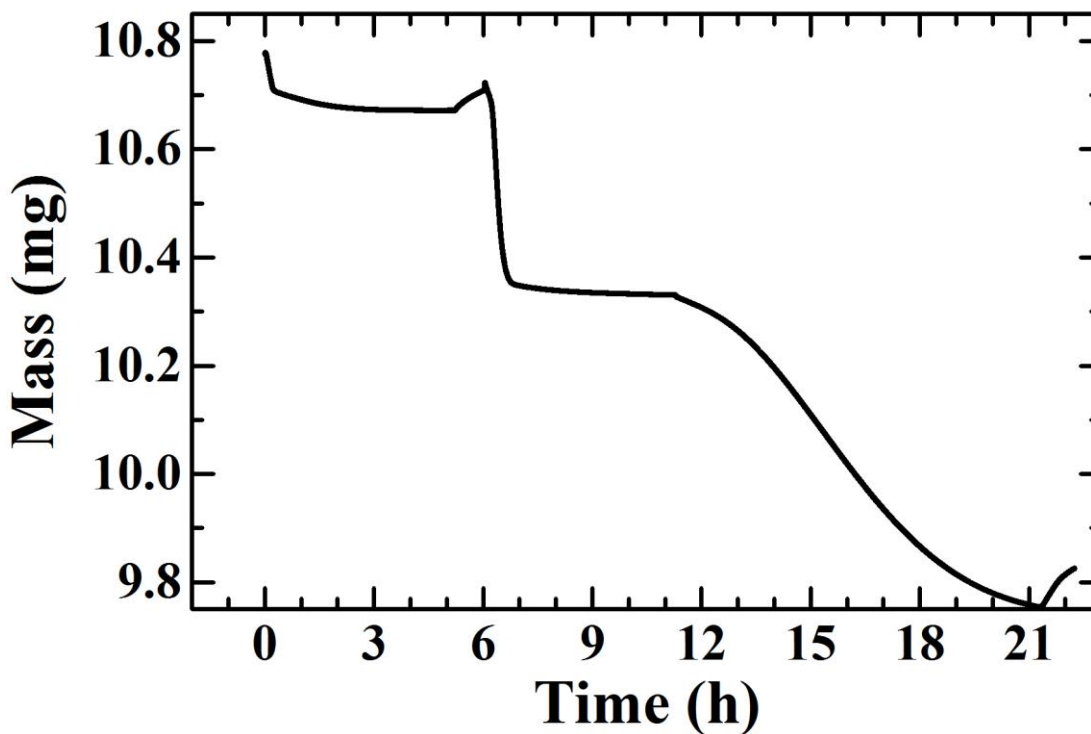


Figure 4.15: The measured mass evolution during a 395°C measurement. This isotherm did not provide sufficient energy to complete the conversion. The rapid mass increase at the end was overwhelmingly due to instrumental effects, but could also signify some oxidation on cooling.

Three distinct isotherms were again used in these measurements. The preliminary isotherm for cleaning the sample again 5 hours at 300°C, and the change from N₂ to a forming gas atmosphere was again at 50°C. Following the change in atmosphere the temperature in each case was raised to 350°C for 5h. This isotherm was designed to complete the transition of SmCoO₃ to Sm₂O₃ and CoO. The change of mass during this isotherm relative to the transition of interest is shown below. Note that for the remainder of this section, time t=0 will once again refer to the time assigned that value for purposes of the isoconversional measurement. In addition, the point of 0% conversion represents a pure Sm₂O₃+CoO phase, while 100% conversion

represents a complete reduction of the CoO oxide and no reduction of the Sm_2O_3 oxide. In this case, due to the presence of the 350°C isotherm, the time $t=0$ was determined to be the beginning of the measured mass change. This choice allows the inclusion of mass changes during the ramp from 350°C to the temperature of interest in the calculation.

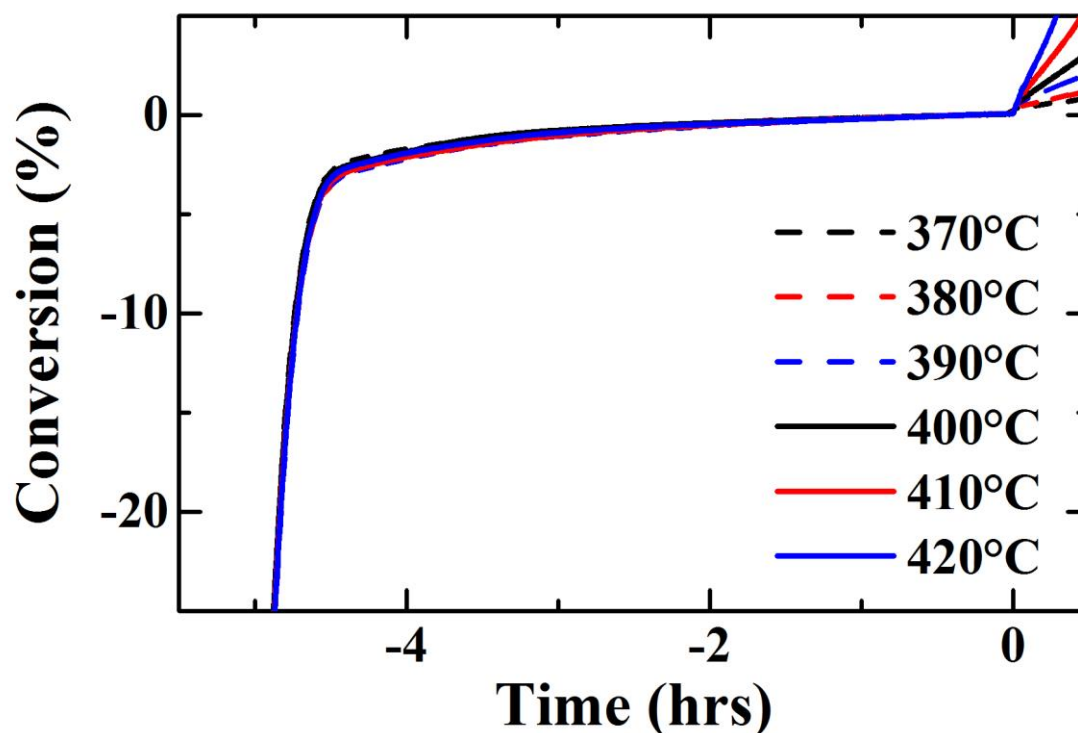


Figure 4.16: Conversion during the 350°C preparatory isotherm for each measurement. No systematic variation was seen or expected in this data.

In each case, during this isotherm the previous conversion rapidly finished. There was no systematic difference between the runs to this point, as shown in figure 4.16. There was the possibility of a slight amount of CoO converting to Co during this

isotherm. Although the temperature was chosen to produce the purest phase of $\text{Sm}_2\text{O}_3+\text{CoO}$ possible, some of the CoO may have converted before the isotherm began. As discussed in Chapter 2, this was not critical.

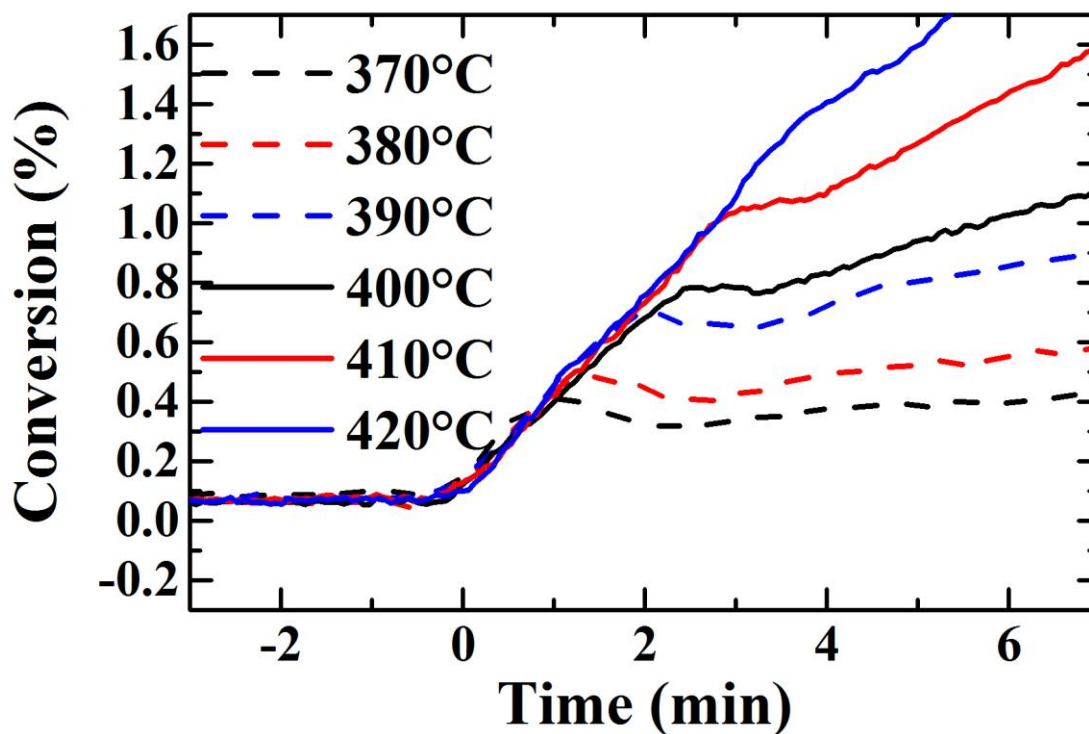


Figure 4.17: Conversion during the ramp from 350°C to the isotherm of interest.

The third isotherm in this sequence was the one at the temperature of interest. Following the 350°C isotherm, the sample was heated at 20°C/min to the desired temperature for a 10h isotherm. Selecting the time $t=0$ was done by assessing the end of the 350°C isotherm. As is shown in figure 4.17, the ramp to the final isothermal value was short, and conversion begins during the ramp in each case, so $t=0$ was assigned to the beginning of the mass change during the ramp.

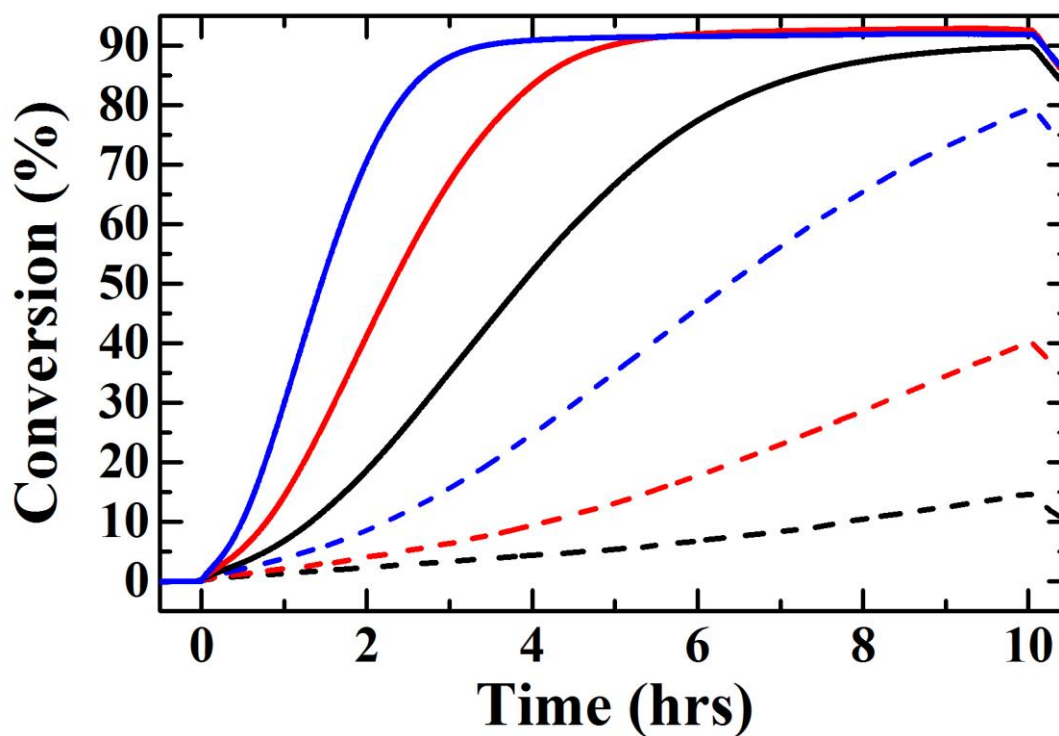


Figure 4.18: Conversion during the 10 hour isotherms. The lack of complete conversion in the 410°C isotherm is likely due to a miscalculation of the initial mass. This miscalculation would be systematic for every isotherm.

A summary of the six reactions is shown in figure 4.18. As detailed above, the amount of total conversion was calculated by assigning the average mass over the final 100 minutes of the 350°C isotherm to 0% conversion. Calculating the mass value that would be reached after full conversion set the 100% conversion value. As shown, the conversion of these samples never reached 100%. This is likely due to the error in assigning m_0 mentioned above, as the highest temperature isotherms seem to reach full conversion.

Isoconversional data for 10% to 40% total conversion is shown in figure 4.19. Activation energies extracted from this data are shown in figure 4.20. There is a slope

to the activation energy data likely indicative of errors in setting $t=0$, although other systematic errors could be contributing.

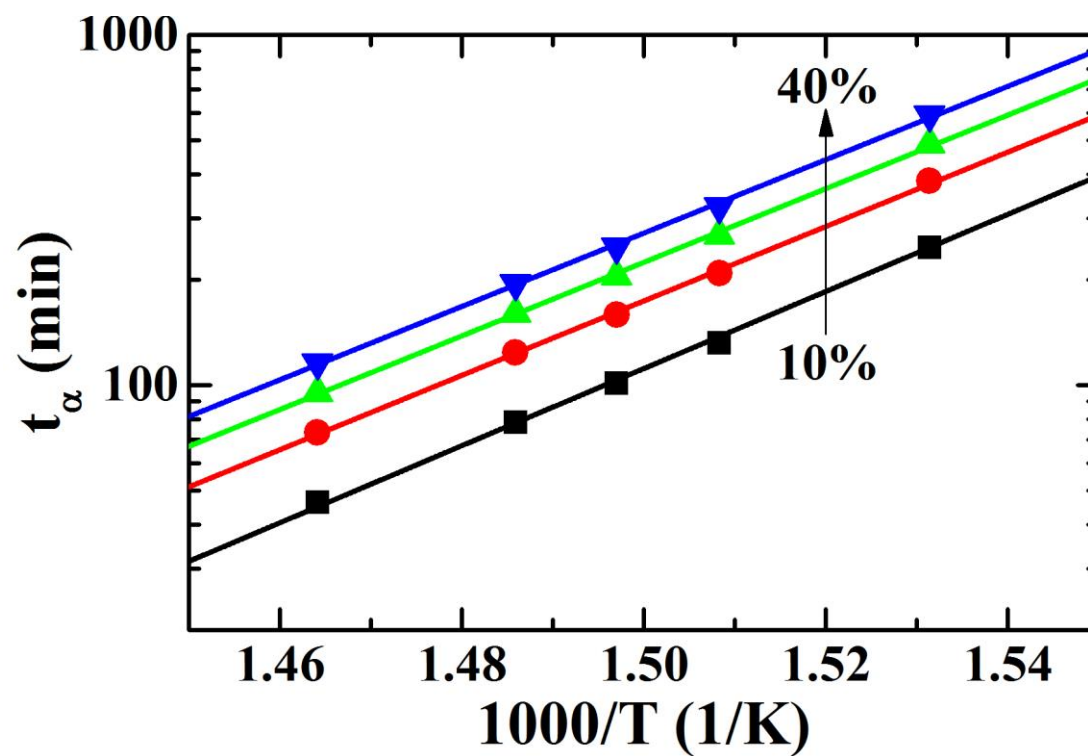


Figure 4.19: Isoconversional data for 10% to 40% of the conversion of CoO to Co metal as a function of the isothermal temperature.

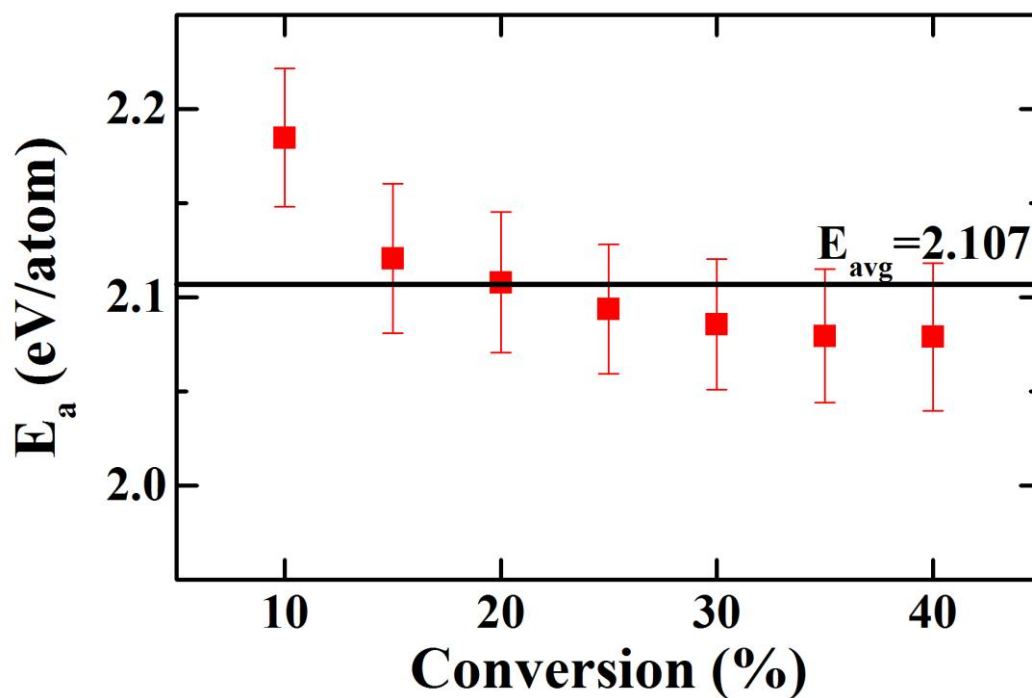


Figure 4.20: The measured activation energy for the CoO to Co reduction reaction in this system. For comparison, bulk activation energies for this system in forming gas are 0.477-0.607eV/atom [74]

A comparison must be made to the bulk value. The data taken here was several times larger than the bulk reported value of 0.477-0.607eV/atom [74]. There is a clear increase in the activation energy of the CoO to Co transition in this system when compared to the bulk. It is interesting to note that this bulk value of the CoO to Co activation energy is less than the Co_3O_4 to CoO activation energy, as shown above.

INTER-GRAIN DIFFUSION IN PT AND PT/NI PARTICLES

In this section, Pt and Pt/Ni sintering and diffusion measurements including initial synthesis and sample preparation procedures are described. Particular attention is given to the sample preparation technique information. Examinations of the results of these measurements reveal that subtle differences in the preparation of these particles can yield drastic behavioral differences in the subsequent experiments.

This work was performed with the assistance of Ronald Cichocki and Jie Ren, who aided in the synthesis and measurement of Pt and Pt/Ni nanoparticles and the Pt monolayer films.

5.1 Pt Sintering Measurements

Pt sintering has been examined both at the University of Delaware and at the Advanced Photon Source at Argonne National Laboratory. The UD measurements examined conventional sintering measurements, while the APS experiments were performed using a hybrid pump-probe style experiments. A general schematic for the definitions of these terms is shown in figure 5.1. More specifically, “conventional” sintering measurements refer to a style of measurement characterized by long excitation times followed by long measurement times. In this variety of measurement, samples are heated approximately uniformly and cool slowly to a stable equilibrium. Measurements can be performed in-situ or ex-situ, but the time resolution for collected data is low. This is appropriate for probing equilibrium or large volume effects. This is in contrast to the “true pump-probe” style mentioned in figure 5.01, a technique in which a sample is excited very quickly, and the properties of the sample are measured during the cooling process. In true pump-probe measurements both the excitation and

measurement are very rapid, often on the order of pico- or femtoseconds in duration. This is appropriate for reversible measurements, as the brief timescale of the measurement generally necessitates repeated measuring of the same sample state.

The “hybrid pump-probe” technique used in this work is a combination of the excitation speed of a pump probe measurement and the equilibrium probing characteristic of a conventional measurement. In this technique, a sample is rapidly heated and cooled, allowing the system to return to a metastable state or a local equilibrium. That state is then completely characterized before the sample is re-excited. This technique is well suited to measuring irreversible changes driven by intense, non-uniform excitations. The specifics of this technique as used in this work are described below.

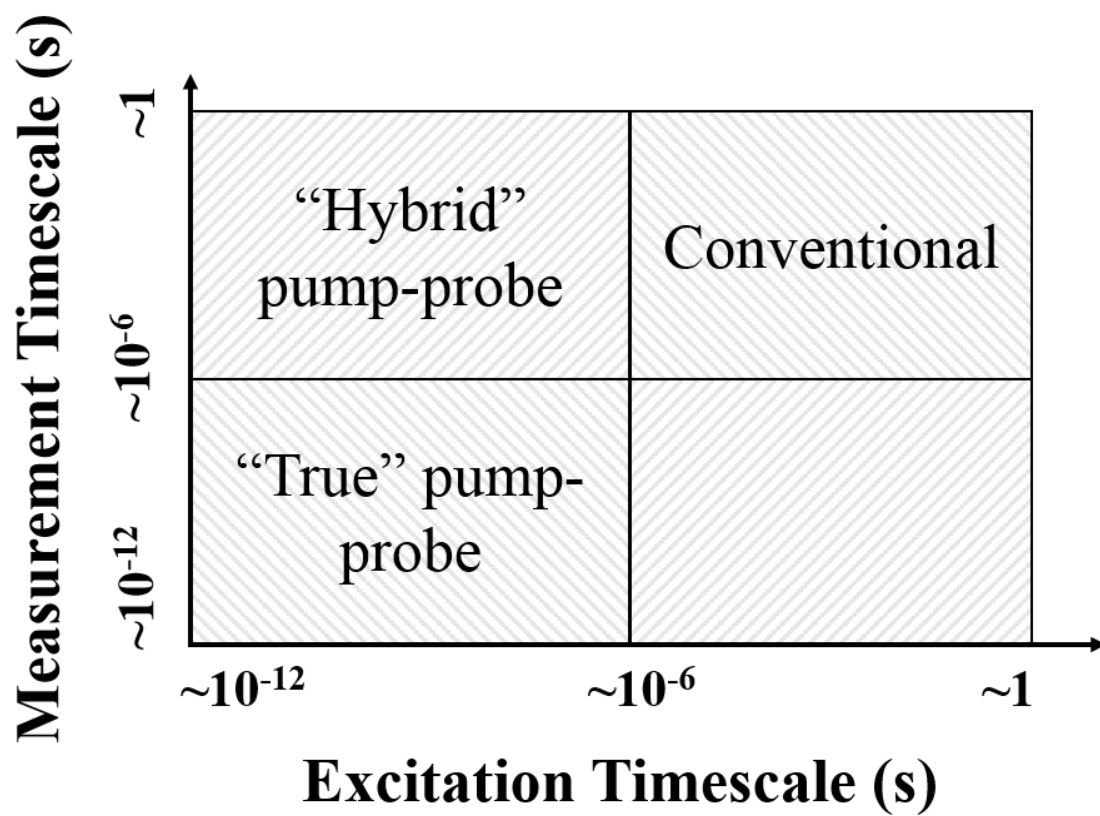


Figure 5.1: Appropriate types of experiment for sintering measurements determined by excitation and measurement time.

5.1.1 Conventional Thermal Measurements

Preliminary sintering measurements were performed on the Pt nanoparticle clusters to examine low-temperature, slow evolution of the particle size. Both the effects of different sintering temperatures at uniform time, and a constant temperature for long times were studied with this technique.

These measurements were intended as a calibration. As it was difficult to calibrate or calculate the temperatures reached in the hybrid measurements, the conventional measurements were largely used to provide context to later

measurements. To that end, a limited selection of reaction conditions were examined. To begin, samples were sintered for 10 minutes at temperatures from 100°C to 179°C. Then, the effects of sintering times up 4 hours at 122°C were studied. The changes in lattice parameter and grain size were measured for each set of experiments.

5.1.1.1 Experimental Conditions

After washing, as-prepared Pt clusters were separated from solution and re-suspended in a mixture of water and ethylene glycol. As shown in figure 5.2, by proper choice of water/EG ratio a reflux temperature between 100°C and 200°C could be selected, which allowed for sintering measurements over the full range of temperatures [75].

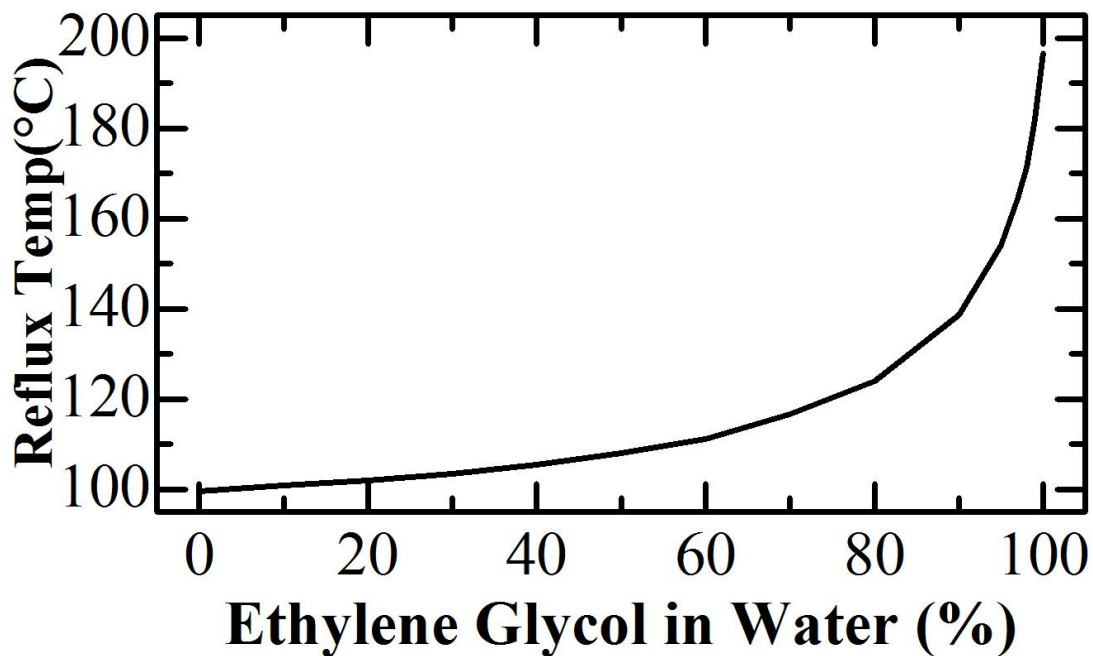


Figure 5.2: The reflux temperature of a water/ethylene glycol mixture by relative amounts of constituent liquids [75].

Measurements were performed using 100mL mixtures of EG and water in the proper ratio to target a desired reflux temperature. Of particular interest, the 122°C temperature was achieved using a 3:1 EG:H₂O ratio. No 100% EG measurements were performed, as even trace water due to the Pt synthesis process strongly suppressed the reflux temperature at small volume fractions. For consistency upon repeated measurements, a mixture of 98mL EG and 2mL H₂O was the most EG-rich solution used.

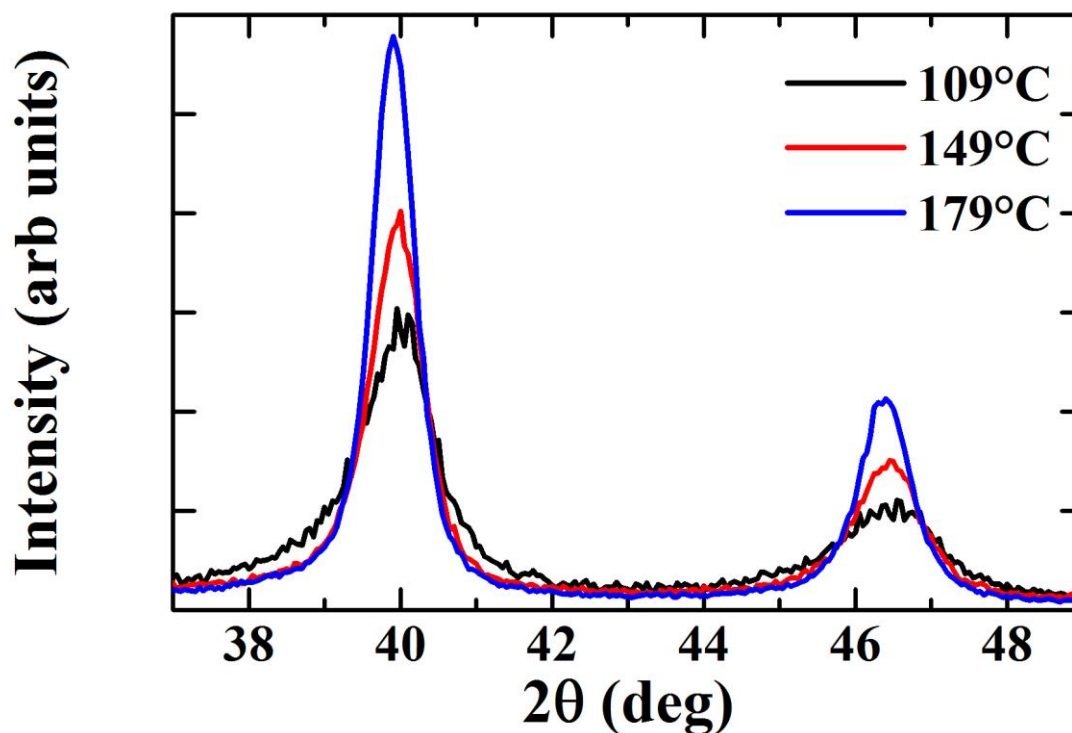


Figure 5.3: A sample comparison of XRD spectra. These patterns are the result of 10min sintering measurements at the indicated temperatures.

Particle sizes and lattice parameters were calculated via fits of XRD measurements of washed and dried samples. A selection of the XRD data collected is shown in figure 5.3. Lattice parameters and Scherrer particle sizes were calculated from the position and width of the (111) Pt peak. Due to the relative intensities of the (111) and (200) peaks, the (200) peak was not used in these calculations.

5.1.1.2 Results

Two main sequences were performed. First, a series of 10 minute reflux measurements were carried out at temperatures between 109°C (50:50 EG:H₂O) and 179°C (98:2 EG:H₂O). Summaries of the Scherrer sizes and lattice parameters calculated from the data are shown in figures 5.4 and 5.5, respectively.

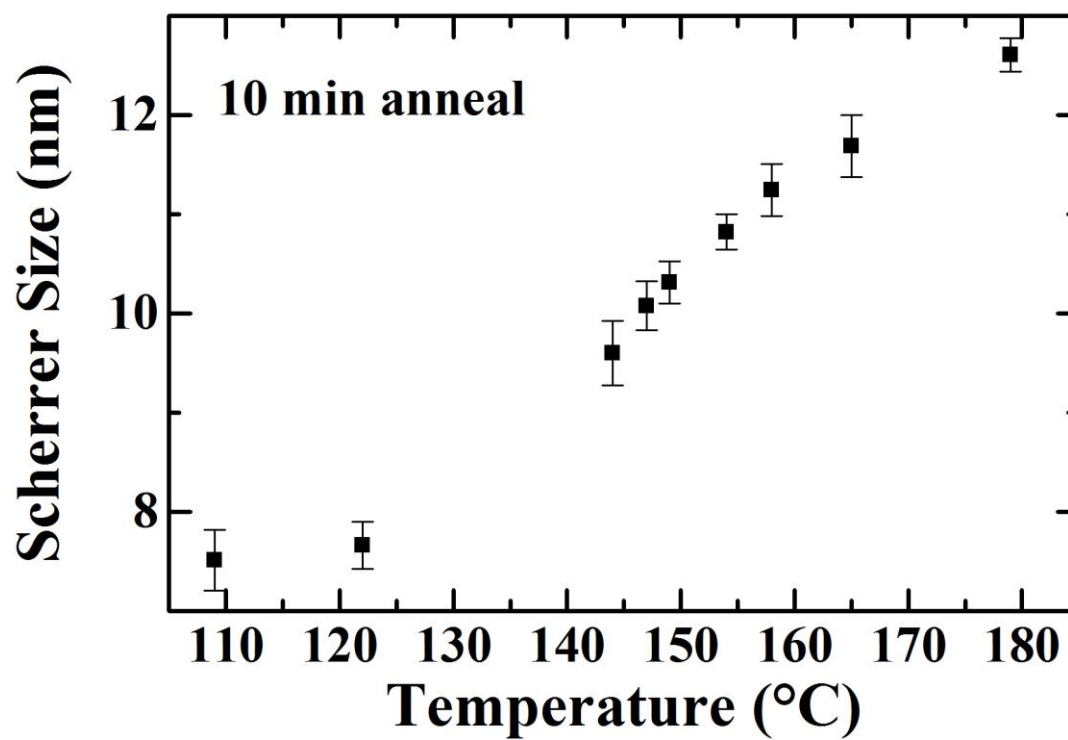


Figure 5.4: Scherrer sizes of Pt particles following 10 minute sintering measurements.

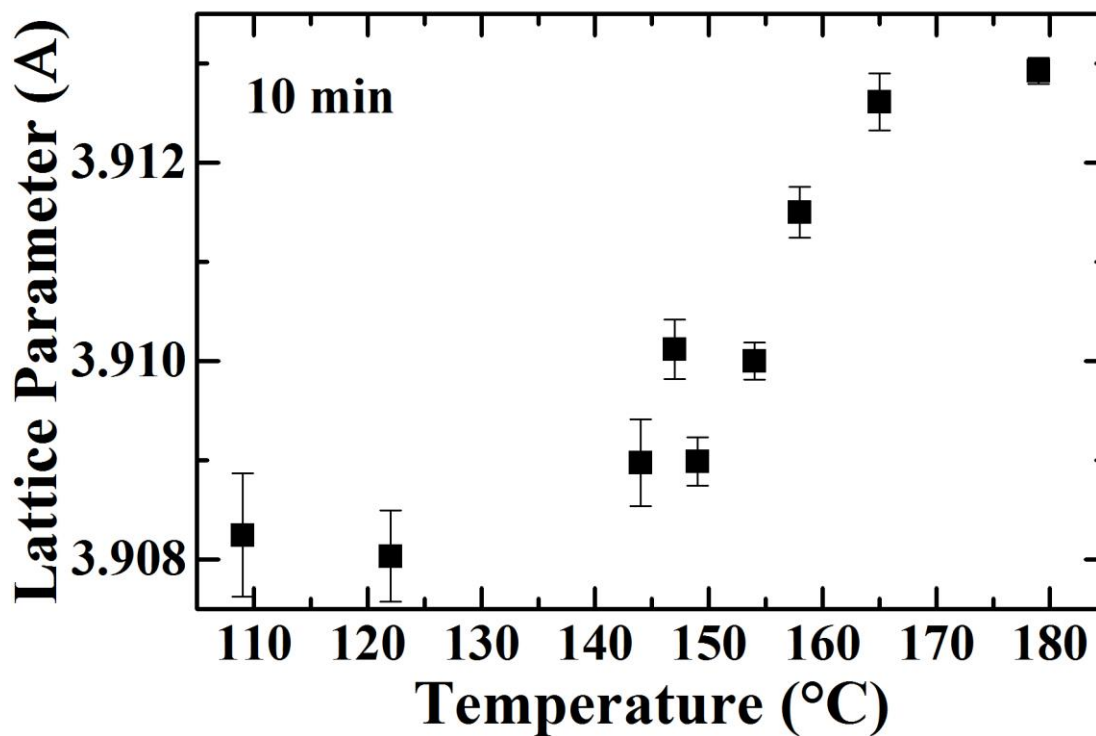


Figure 5.5: Lattice Parameter of Pt particles following 10 minute sintering measurements.

The temperature dependence of the particle size and lattice parameter of these Pt nanoparticles was monotonic, as expected, although the functional dependence looks complicated, likely due to the nonlinear nature of the energy dependence. This was compared to the time-dependence at a constant (low) temperature of 122°C. Measured Scherrer sizes and lattice parameters for this series of measurements are shown in figures 5.6 and 5.7.

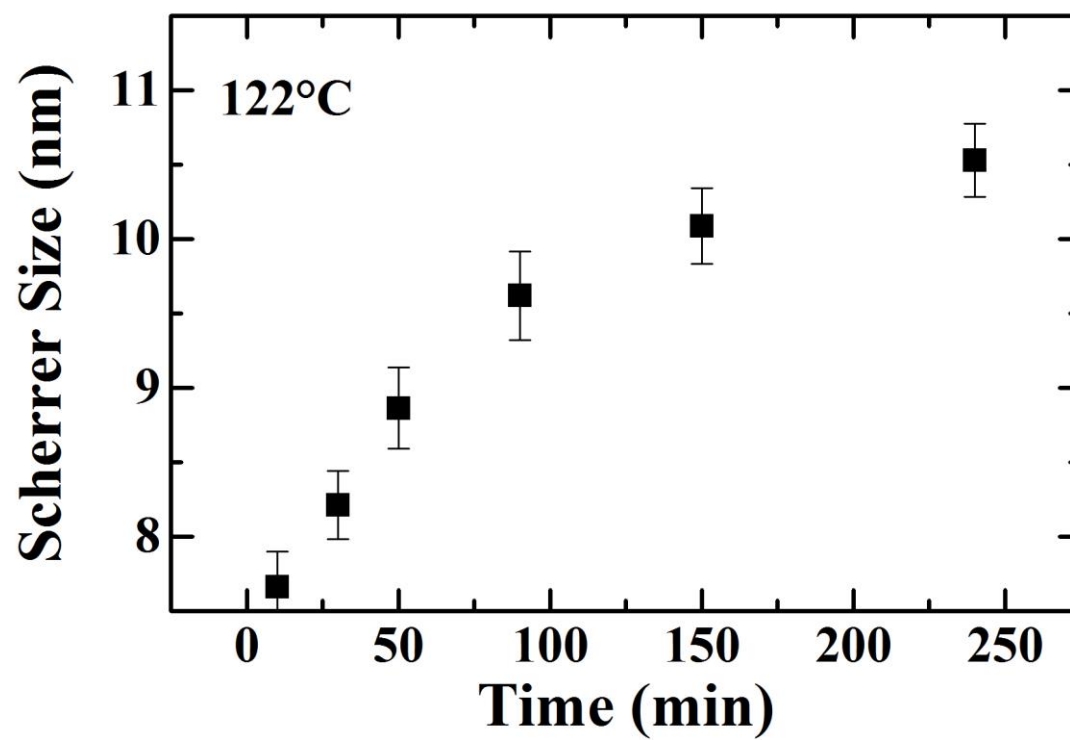


Figure 5.6: The time-dependence of Pt nanoparticle sizes annealed at 122°C.

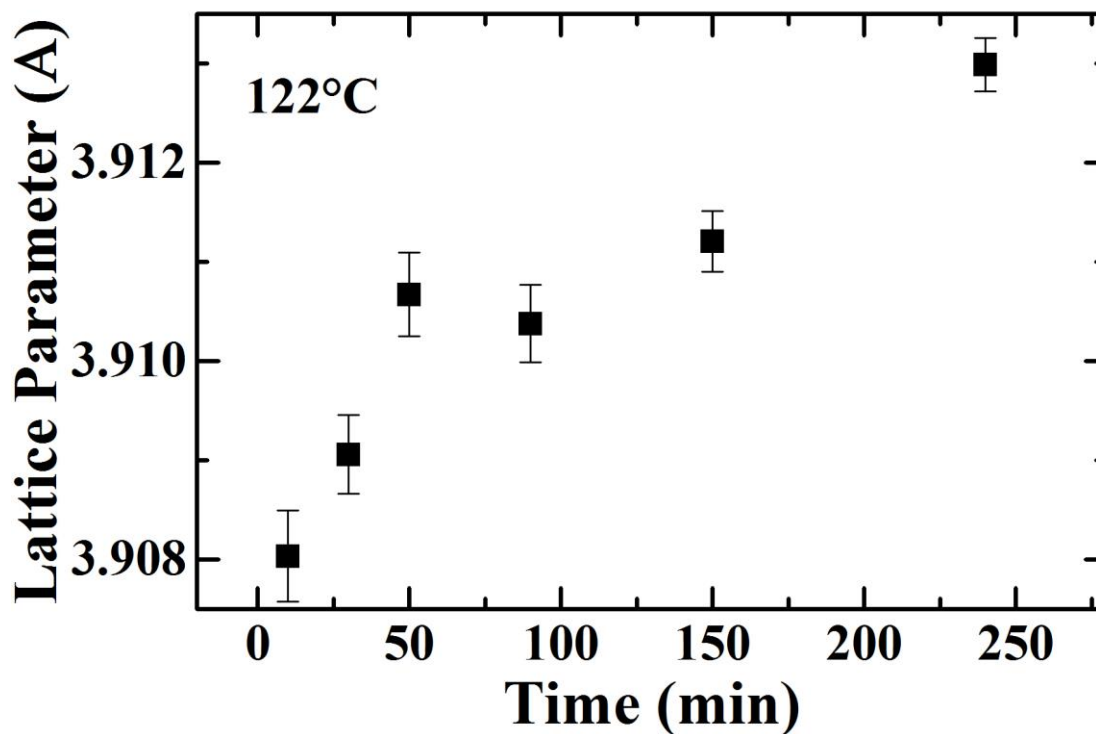


Figure 5.7: The time-dependence of Pt nanoparticle lattice parameters annealed at 122°C.

The 122°C series of sintering measurements also proceed roughly as expected, although there was a slight deviation from the monotonic behavior in the lattice parameter measurements. This is likely attributable to experimental error, and not a fundamental effect. We did not attempt to predict or fit a functional dependence to this data. Instead, we examined the relationship between the lattice parameter and the Scherrer size, shown in figure 5.8.

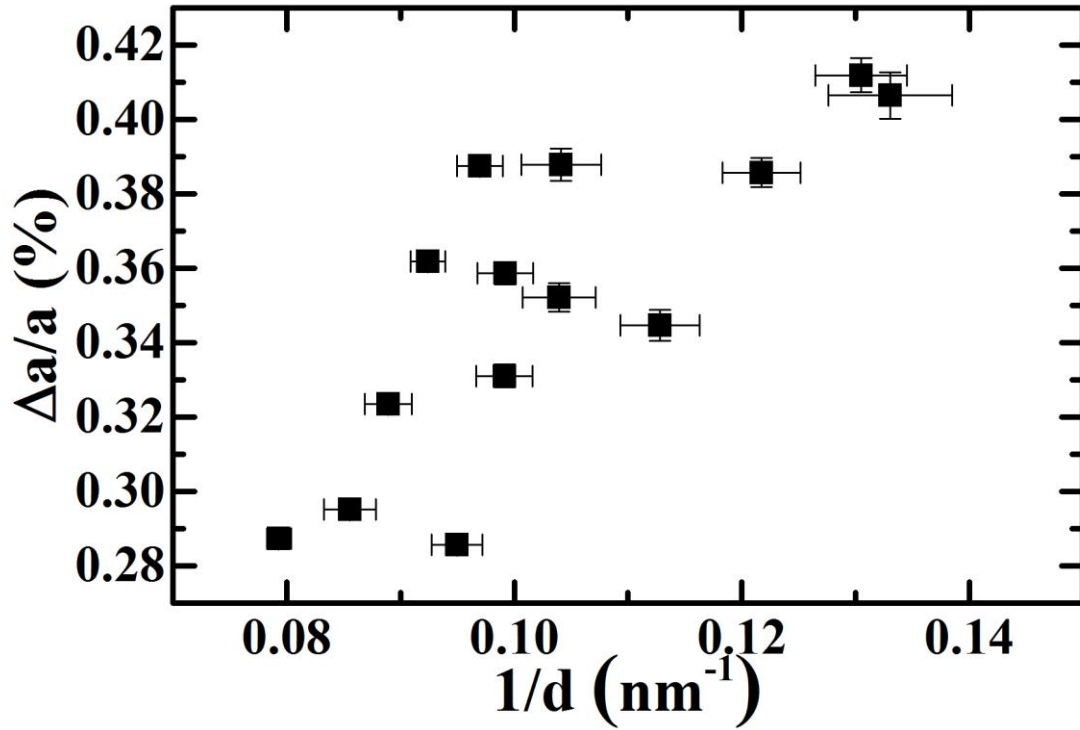


Figure 5.8: The change in lattice parameter of conventionally sintered Pt particles vs the inverse Scherrer size. The change in lattice parameter is relative to the bulk value of 3.8242\AA [76]

From the Laplace equation, the change in lattice parameter is expected to be proportional to the inverse particle size, with a proportionality constant dependent on the bulk modulus and surface stress of the particles. The quality of this data is not high enough to fit to that relationship, but that functional dependence seems plausible from this data.

5.1.2 Laser-driven Sintering Measurements

The hybrid measurements of Pt nanoparticle sintering were performed on samples in TEG. The following section presents first then experimental details of the hybrid measurement and then results for the laser-induced sintering of Pt

nanoparticles. Finally, some difficulties associated with this measurement in air and preliminary results are presented.

5.1.2.1 Sample Preparation and Measurement Parameters

For this series of measurements, the as-prepared Pt nanoparticles were suspended in TEG with trace water for shipping and storage. For measurement, the samples were mixed with a small volume of ethanol and suspended in a polycarbonate capillary tube (288 μ m ID, 360 μ m OD) by injection. A schematic of this design is shown in figure 5.9. After visually confirming the presence of some Pt in the capillary, a segment approximately two inches long was cut and very gently heated to encourage evaporation of most of the EtOH/TEG mixture. Some TEG remained in the capillary after the drying process.

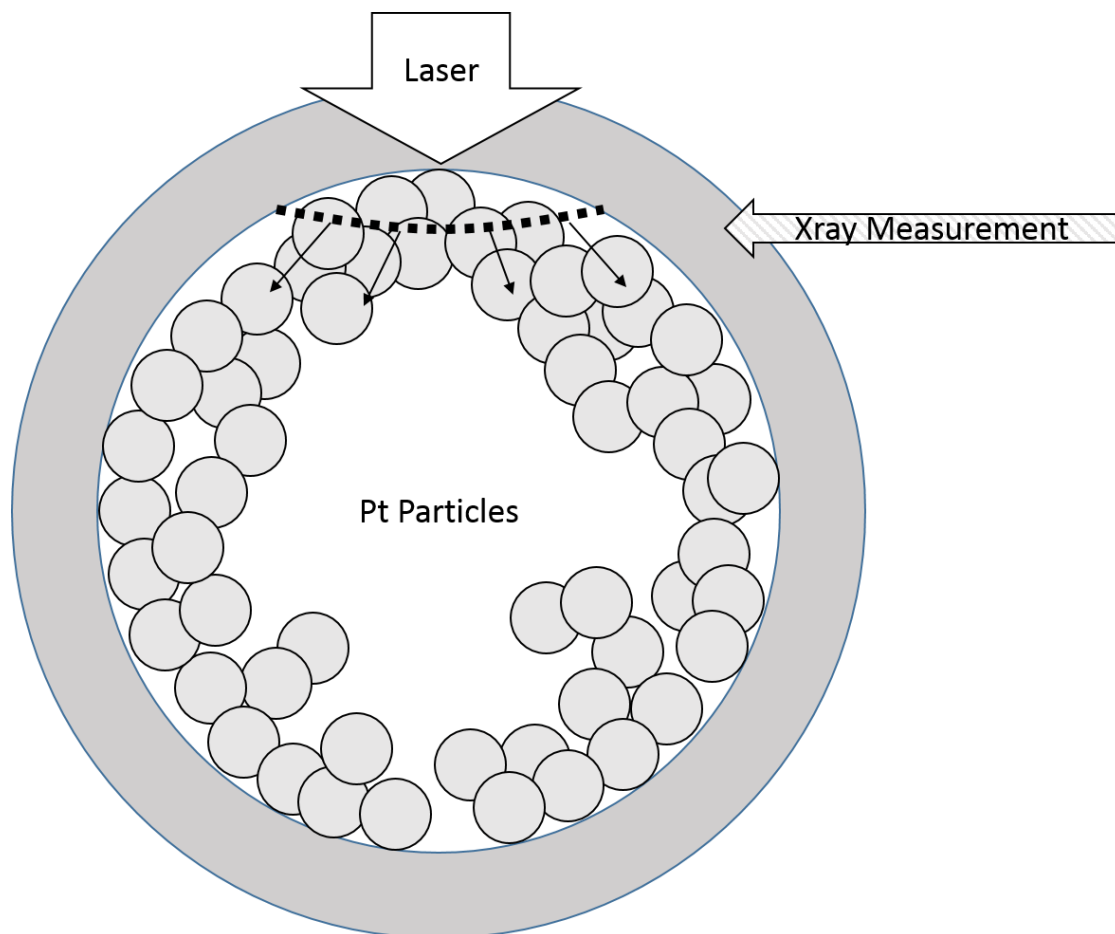


Figure 5.9: Schematic of Pt nanoparticles in a capillary tube used for hybrid measurements. Incident photons that were not scattered by the polycarbonate tubing were absorbed in the top layer of Pt particles, causing sintering. Other particles sintered by indirect heating.

The capillary was magnetically mounted on a precision goniometer in the measurement field. As directly aligning the samples in the interaction volume was not possible due to the thickness of the capillary, the top of the capillary was centered in the proper location, and then the mount was translated vertically 100 μ m to place the top of the interior of the tube in the interaction volume.

Optical excitation was performed using a variable wavelength laser set to 780nm, and the sample was probed with a 9.45keV x-ray beam. Incident laser fluences from $50\text{mJ}/\text{cm}^2$ to $87.5\text{mJ}/\text{cm}^2$ were used. The lower bound of this range was set by the rate of observable sintering, while the upper was the limit at which the sample could be irradiated without compromising the structural integrity of the capillary tube. At higher fluences there was also come evidence of vaporization in the TEG causing convective currents in the sample.

5.1.2.2 Results

The Pt nanoclusters in TEG were sintered and the peak width and position were tracked from the as-prepared state through 600-900 laser shots in 100 shot increments for the $50\text{mJ}/\text{cm}^2$, $62.5\text{mJ}/\text{cm}^2$, and $75\text{mJ}/\text{cm}^2$ fluences, and to 4000 laser shots in 1000 shot increments for the $87.5\text{mJ}/\text{cm}^2$ fluence. Integrated signals clearly showed the Pt (111) and (200) peaks, as well as a strong background signal from the polycarbonate tubing and residual TEG. Peaks were fit using a Pearson VII lineshape. This data for the (111) peak without further analysis is presented in fig. 5.10.

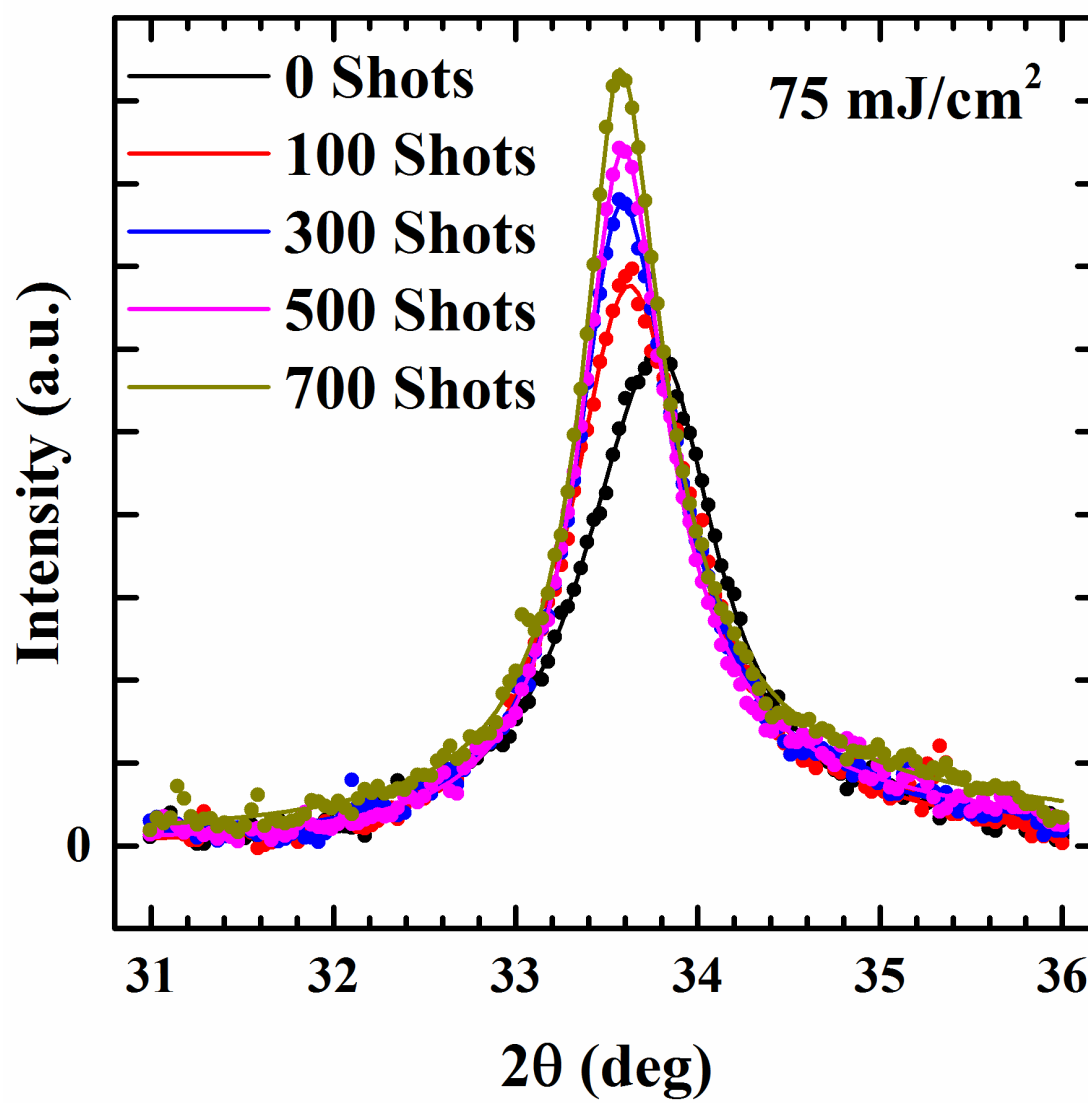


Figure 5.10: Integrated XRD data for the Pt (111) peak of select $75\text{mJ}/\text{cm}^2$ runs with fits to a Pearson VII lineshape.

Knowledge of the miller index of the peak and incident x-ray wavelength was sufficient to find the lattice parameter using Bragg's law and estimate a coherent scattering length using the Scherrer formula. The calculated lattice parameter as a function of the incident integrated laser fluence is shown in figure 5.11.

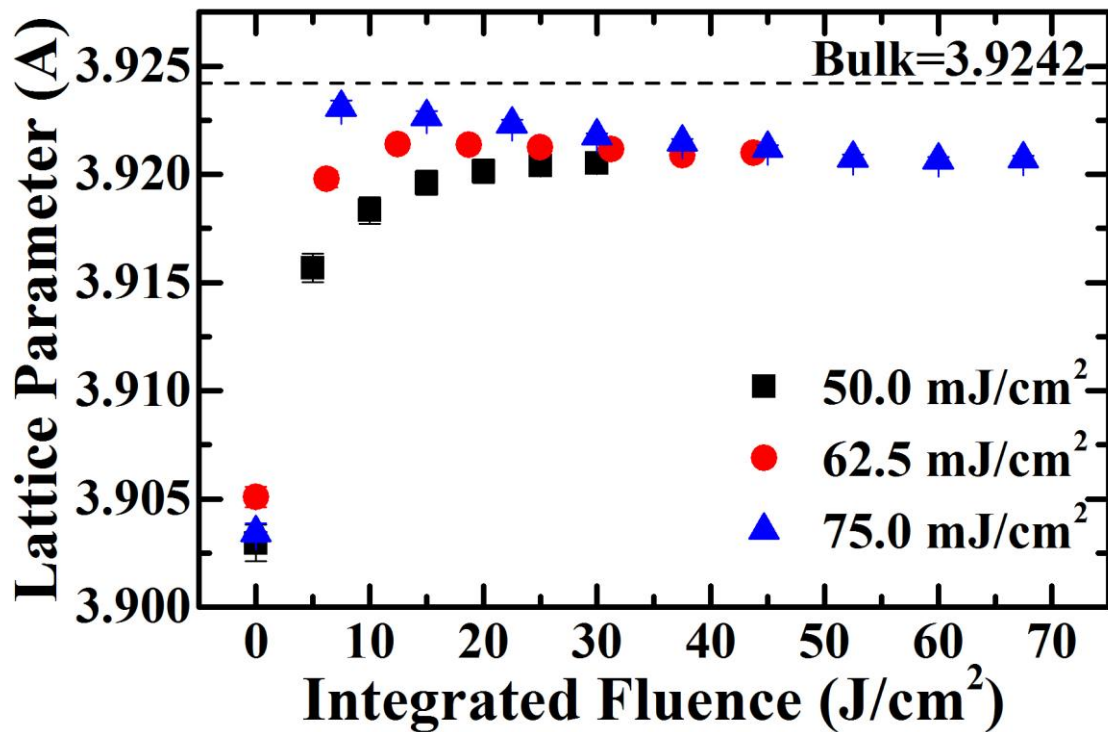


Figure 5.11: Lattice parameter evolution for Pt sintering measurements. The sample irradiated for the longest time at the highest fluence is pictured along with the energy-dependent data for the lower fluences. The size of the most-sintered sample was calculated to be approximately 30nm using the bulk lattice parameter relationship.

This relationship is clearly not what is predicted by the Laplace equation. The most obvious deviation from the expected results is that the lattice parameter is not monotonic. The lattice clearly over expands past the equilibrium in the $75\text{mJ}/\text{cm}^2$ measurement, and although the effect is not as obvious in the $62.5\text{mJ}/\text{cm}^2$ measurement it appears in that data as well. A similar comparison with particle size is shown in figure 5.12.

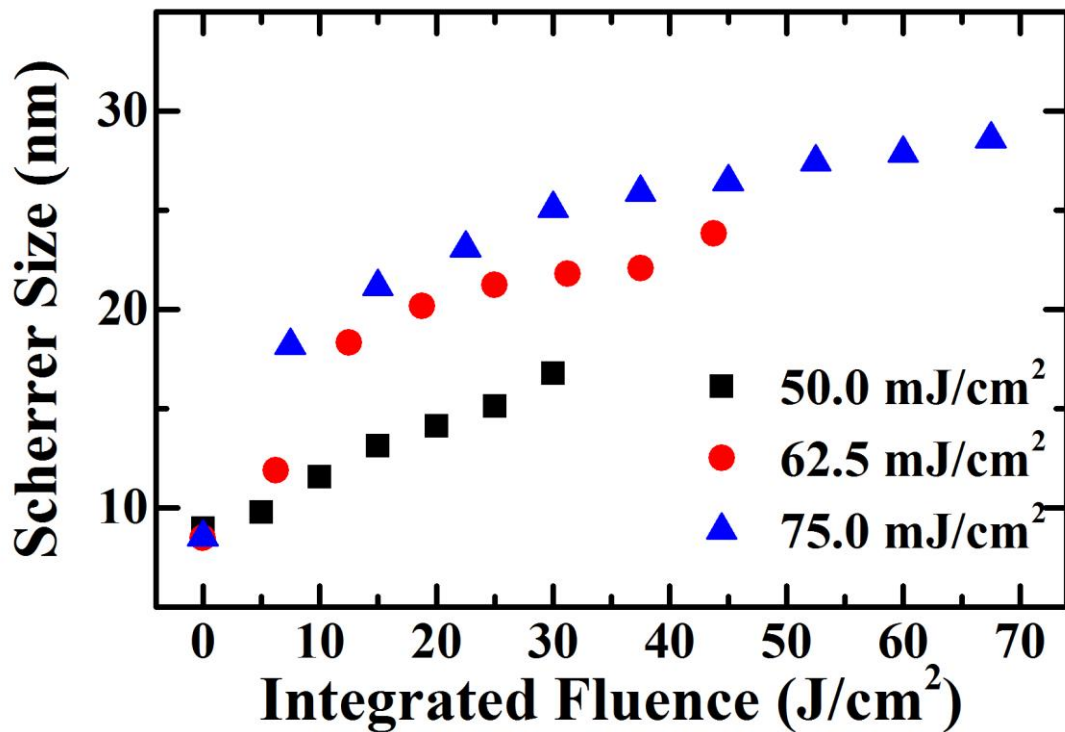


Figure 5.12: Scherrer calculated particle size for Pt sintering measurements. Although the results at each fluence are monotonic, they do not appear to follow a consistent functional form. Error bars are smaller than the symbols.

Here, the size evolution was monotonic (as expected). Although the lattice drastically expanded, the particle did not grow a corresponding amount. Figure 5.13 shows a direct comparison of the calculated Scherrer size and the lattice parameter for the 50, 62.5 and 75 mJ/cm² fluences. Not only did the size vs lattice parameter relationship depend strongly on the fluence (i.e. the rate of heating), it also did not have a consistent functional form.

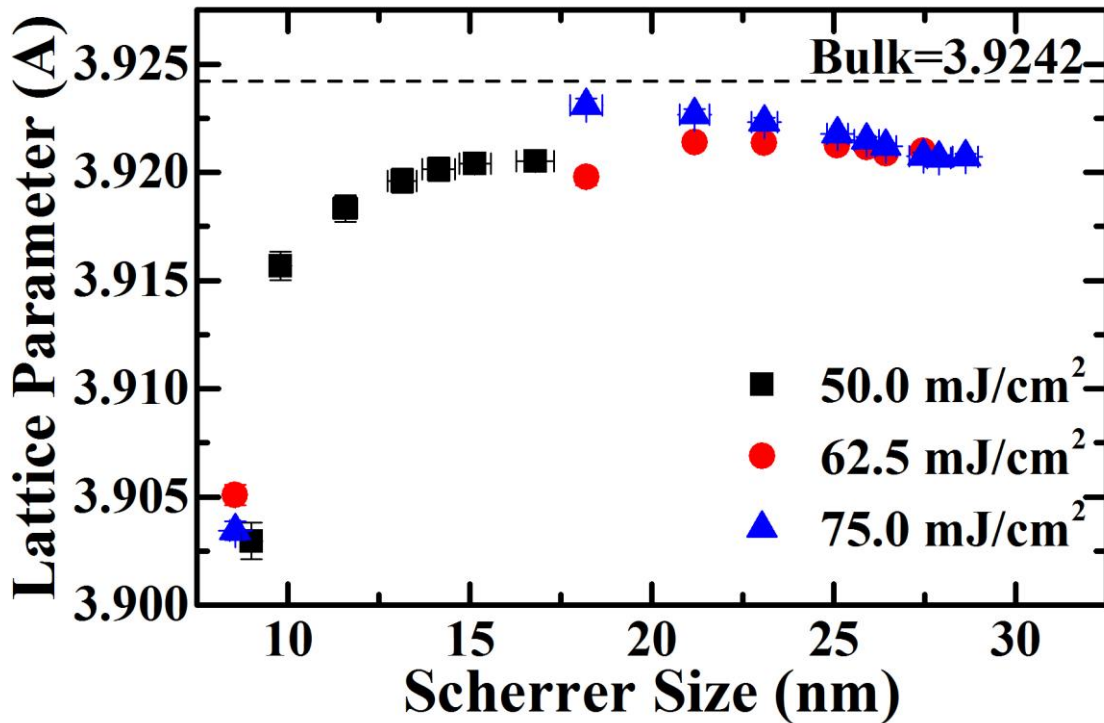


Figure 5.13: Lattice parameter vs particle size for laser-driven sintering measurements. The lattice parameter is clearly not solely a function of particle size, and there is no obvious functional dependence.

Two interesting features were present in this data. First, the relationship between the lattice parameter and particle size was not monotonic. A local maximum for the lattice parameter was clearly visible in the 75mJ/cm² data that did not correspond to the maximum size. This hinted to a complicated interaction between the surface size and the stresses on the atomic lattices in these clusters. As the size increased, the lattice seemed to over-relax, expanding beyond the expected value and being forced to contract upon further excitation. This behavior was absent at 50mJ/cm², and far less pronounced at 62.5mJ/cm² (although still visible at that fluence).

The second unexpected result was that each of the 50, 62.5 and 75mJ/cm² fluences seemed to drive the particles towards a similar lattice parameter, despite the drastically different functional forms of the lattice parameter vs incident laser shot relationships in the three cases. This value was similar to the final lattice parameter after 4000 excitations at 87.5mJ/cm², as well. Assuming a bulk lattice parameter of 3.9242Å [76], this final lattice parameter corresponded to an expected size of approximately 30nm, close to the size of a single Pt cluster.

The laser-driven measurements were also explicitly compared to the conventionally sintered particles. Although the total delivered energies were not comparable, the relationship between lattice parameter and Scherrer size is shown in figure 5.14, while the same data represented in terms of the percent change of the lattice parameter as a function of the inverse size is shown in figure 5.15. The conventional measurements do not demonstrate the initial drastic increase in lattice parameter characteristic of the hybrid measurement, and although the range of Scherrer sizes probed by the conventional technique is small the lattice parameter evolution appears monotonic with the particle size.

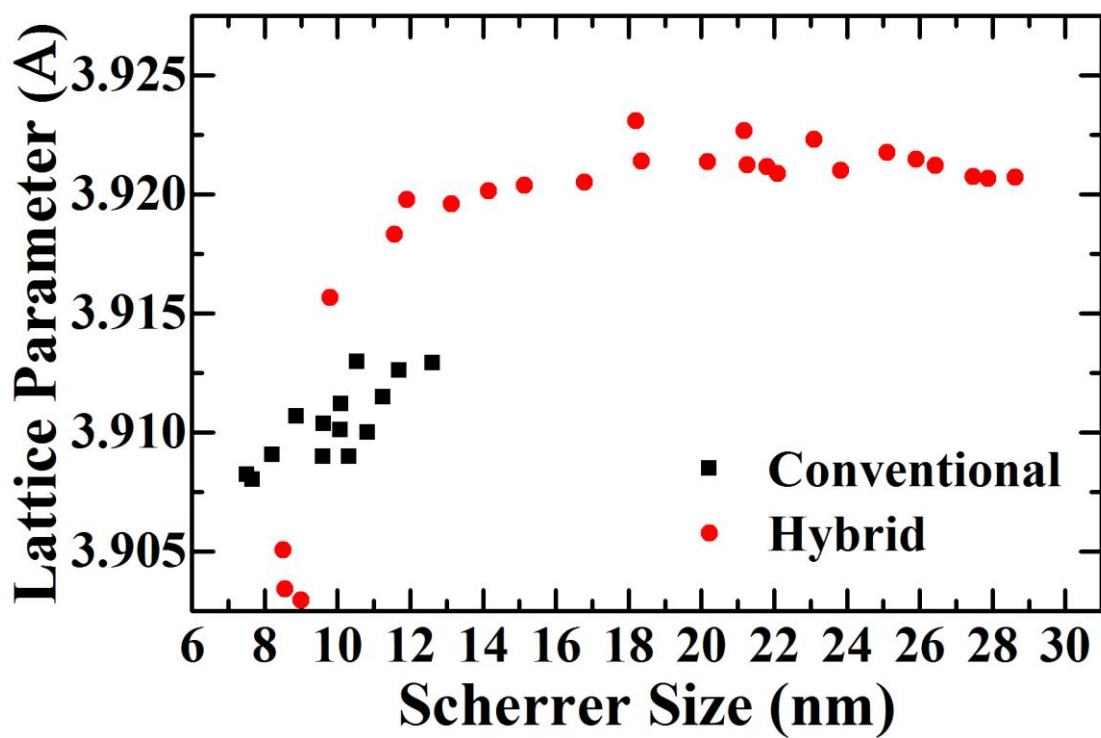


Figure 5.14: A summary of the size dependence of the Pt lattice parameter measured by conventional and hybrid techniques. In all cases, error bars are smaller than the data markers.

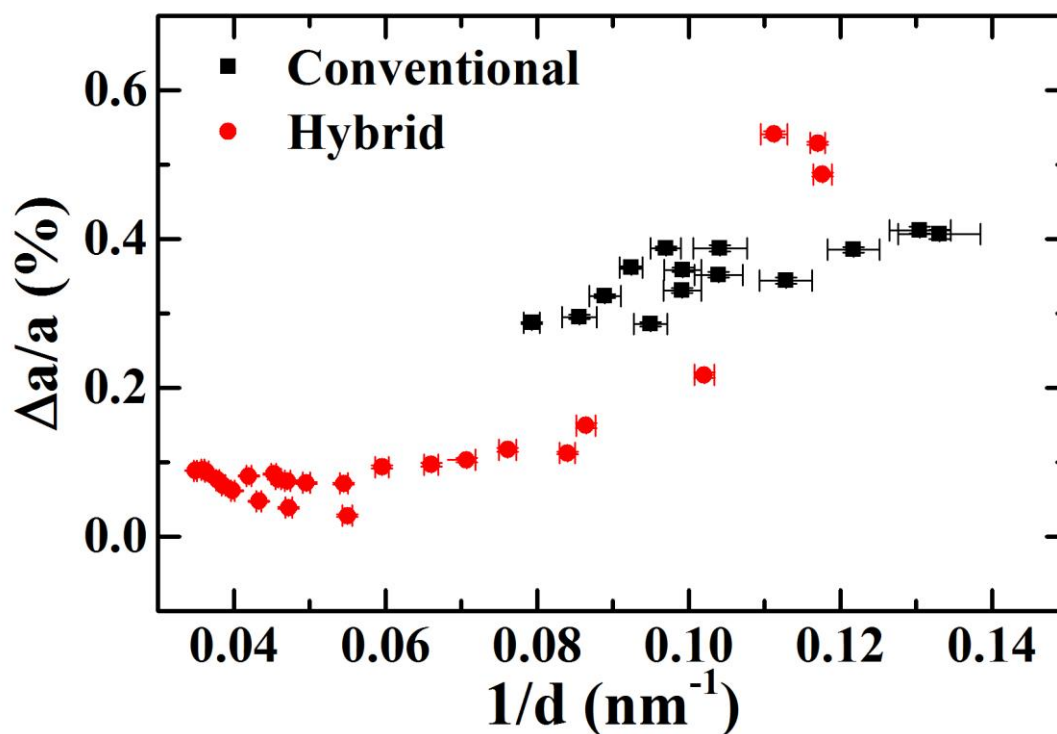


Figure 5.15: The magnitude of the change from the bulk lattice parameter as a function of the inverse particle size.

5.1.2.3 Discussion

The results of the lattice parameter and Scherrer size measurements shown above are significantly different from those of previous studies of Pt nanoparticles. For example, an expanded lattice in small Pt nanoparticles has previously been reported [77, 78], in contrast with the compressed lattice seen here in the as-prepared and conventionally sintered particles. In the cases where a compressed lattice was reported, the lattice parameter evolution was typically described by the Laplace equation [79-81]. No previous reports discuss non-monotonic lattice parameter evolutions in Pt, although the behavior has been seen in other metals [59, 60].

To examine the possible causes for this unique lattice parameter evolution, the value of surface stress in the as-prepared Pt nanoparticles was calculated using the Laplace equation. Using an initial particle size of 8nm and a bulk modulus $B=280$ GPa [82] yields a value for the surface stress of about $\sigma_s=9.5$ J/m². This value is similar to reported experimental and theoretical values [79, 81, 83], suggesting the initial Pt nanoparticles are not the cause of this behavior. Instead, the lattice parameter evolution is likely a byproduct of the laser driven sintering method. This observation is supported by the strong fluence dependence of the effect.

A TEM study of the lattice parameters of Pt nanoparticles provided additional insight into the lattice parameter evolution observed here [77]. This study revealed an expanded Pt-Pt interatomic distance arising from the formation of surface Pt-O-Pt bonds, an effect also seen in Pd nanoparticles [84]. This suggests the strong positive surface stress in the Pt nanoparticles seen here would be suppressed by oxidation of the surface, leading to a more rapid increase in the lattice parameter than is predicted by the Laplace equation with the assumption constant surface stress. This rapid oxidation could be explained by the removal of TEG coating the Pt nanoparticles during the measurement, either by absorption of an optical photon or due to the rapid heating of the Pt nanoparticles.

This explanation does not account for the non-monotonic lattice parameter evolution observed at high fluences. Such behavior could be explained by changing stress fields associated with the inclusion of defects and/or excess volume during grain growth, but no direct measurements of this have been made.

5.1.2.4 Lattice Parameter Changes in Air

A measurement of dried Pt particles followed the measurement above. Monolayers of Pt clusters were deposited on glass slides using the technique described in chapter 3, but during measurements an odd effect was observed. Namely, the lattice parameter of the dried Pt particles did not evolve during sintering, despite observable particle growth visible in XRD peak narrowing. The lattice parameter evolution is shown in figure 5.16, while the Scherrer size evolution is shown in figure 5.17.

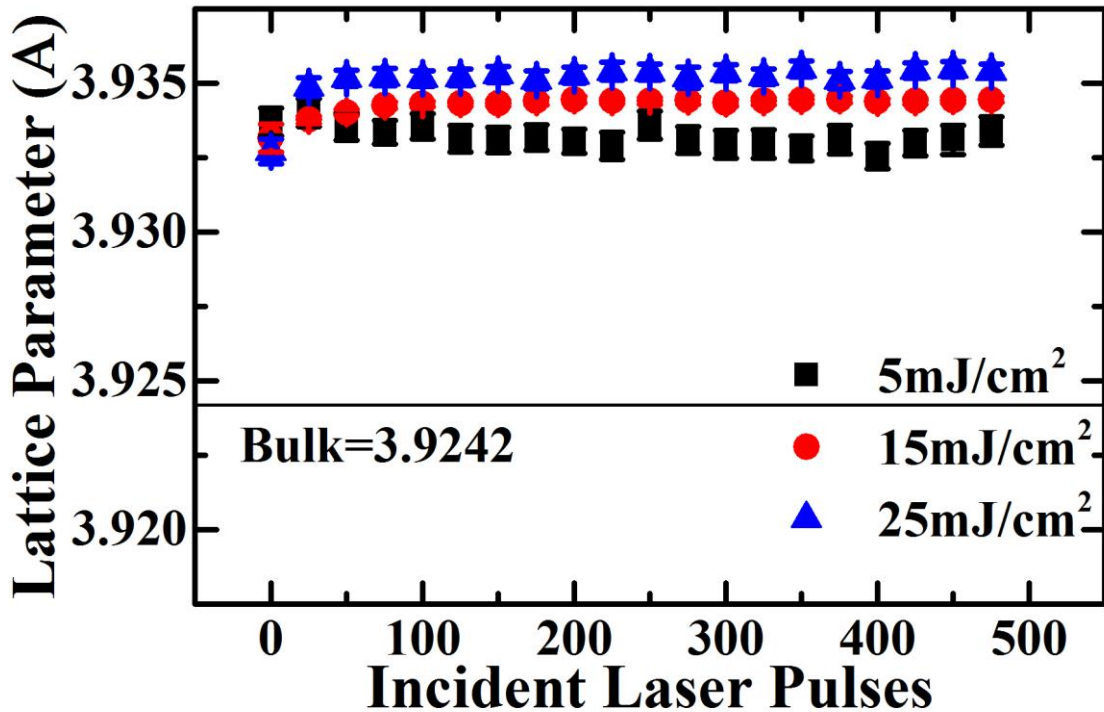


Figure 5.16: The lattice parameter evolution of monolayer Pt clusters under repeated excitation.

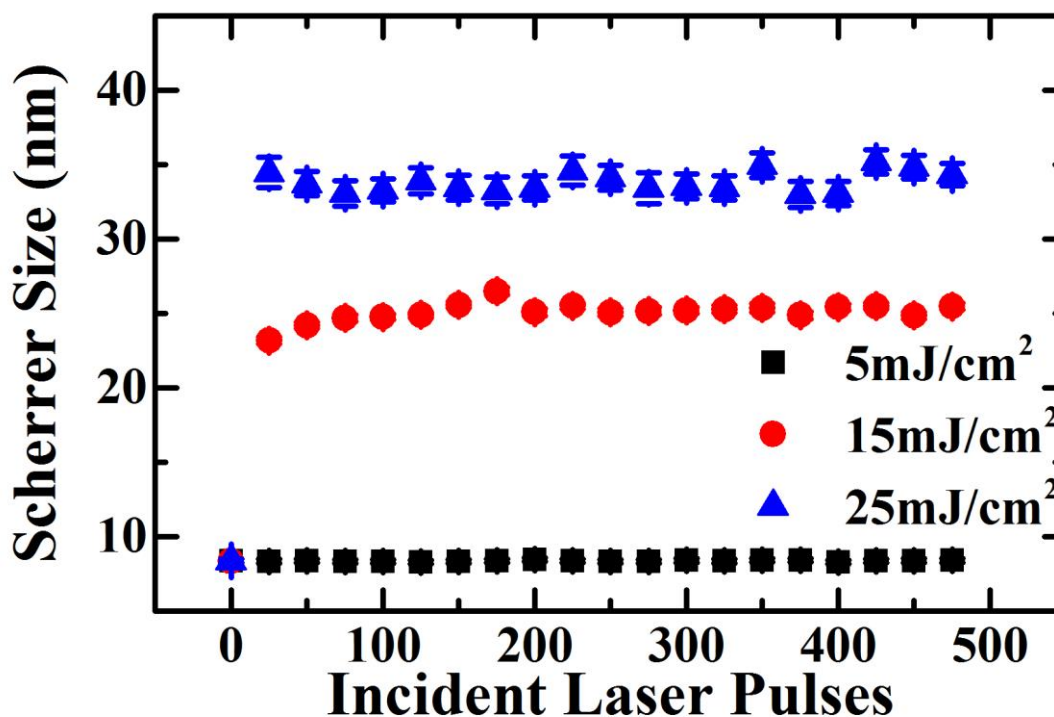


Figure 5.17: The Scherrer size evolution of monolayer Pt clusters under repeated excitation.

Clearly, despite beginning at the same size, there were significant size changes at high laser fluences that were not reflected in lattice parameter measurements. Furthermore, the lattice parameter was far larger than the bulk value, even in the as-prepared sample. The expanded as-prepared lattice suggested the nanoparticle surfaces were oxidized as described in the previous section, but the lack of progressive lattice parameter and Scherrer size evolutions on repeated excitation prompted a more in-depth study of the effects of the monolayer deposition process on the Pt clusters.

To determine the effect of the monolayer deposition process, a batch of Pt nanoparticles was synthesized and cleaned using two methods. First, a portion of the sample was washed using the standard water-based techniques described in Chapter 3.

The rest of the Pt was mixed with varying amounts of ethanol, to recreate the conditions of the monolayer synthesis. Both samples were then dried in air. Simple laboratory XRD measurements were used to measure peak widths and positions of each of these samples, and these values were tracked over several days. The lattice parameters calculated from these values are shown in figure 5.18, while Scherrer sizes are shown in figure 5.19.

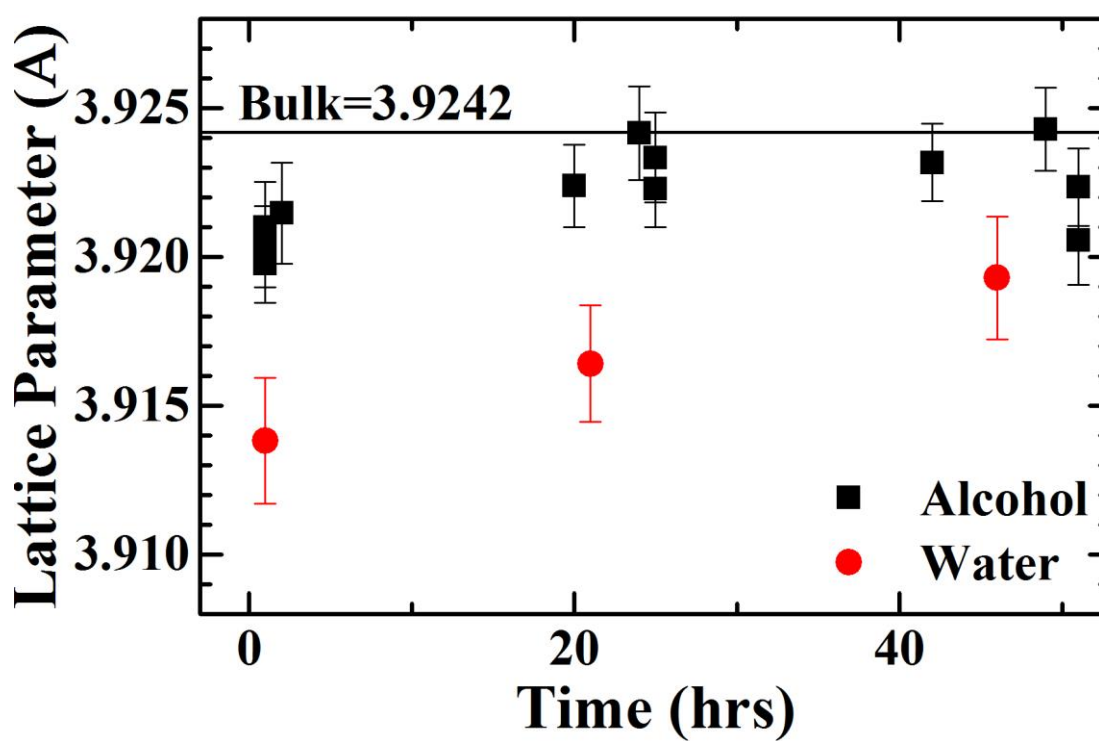


Figure 5.18: The variation in measured lattice parameter for samples stored in air after being mixed with water or ethanol as a function of time since drying.

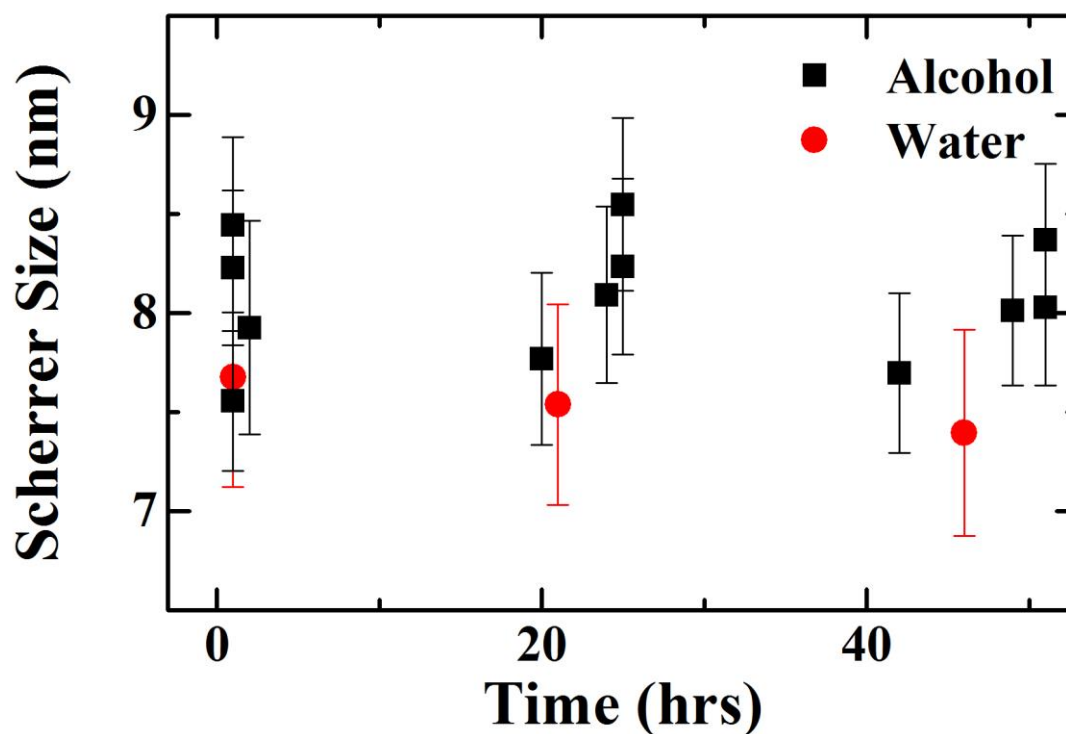


Figure 5.19: The variation in sample size over the same interval as the previous figure.

A clear effect due to the presence of ethanol is seen in this data. As-dried lattice parameters shifted by $\sim 0.005 \text{ \AA}$ after mixture with alcohol, while no change was observed in the Scherrer sizes. Over time, the lattice parameter of the sample exposed only to water also began to increase. The effect of the ethanol washing step is likely a cleaning of the surface of the Pt nanoparticles, as surface oxidation occurred far more rapidly in that system. This result signified the measured data of the dried Pt particle monolayers is not inconsistent with the data measured from Pt in TEG, but rather is due to the different chemical nature of the system. It also suggests the inconsistency between the Pt nanoparticle sintering results shown here and previously published are due to sample preparation techniques and handling, in addition to the effects of the

laser-driven sintering techniques. Further investigation into the synthesis of monolayer Pt in a form suitable for pump-probe measurement is ongoing.

5.2 Multilayer Ni/Pt diffusion

The diffusion of Pt and Ni in a highly modulated multilayer system has been studied, following the Pt sintering examinations. With the help of Dr. Yang Zhou, a multilayer structure of elemental Pt and Ni was sputtered on a Si substrate. The exact stack was 10nm of Ta as a base layer a Si wafer, followed by alternating 5nm Ni and 5nm Pt layers, with an additional 5nm Ni layer on top. The purpose of these measurements was largely exploratory. The primary goal was to confirm the viability of laser-driven diffusion in the Pt/Ni system. Preliminary data follows, while a more in-depth examination is ongoing.

These measurements were performed in a laboratory XRD system using a high-temperature stage. A series of sintering measurements were carried out at temperatures from 100°C to 400°C. Data was collected from both the low-angle and the Pt and Ni (111) Bragg peaks. Each measurement series was progressive, meaning the same sample underwent extended isotherms at each temperature of interest. As a result, the temperature profiles for these measurements were complicated, and diffusion was progressing appreciably even during the collection of the XRD spectra. A sample temperature profile is shown in figure 5.20.

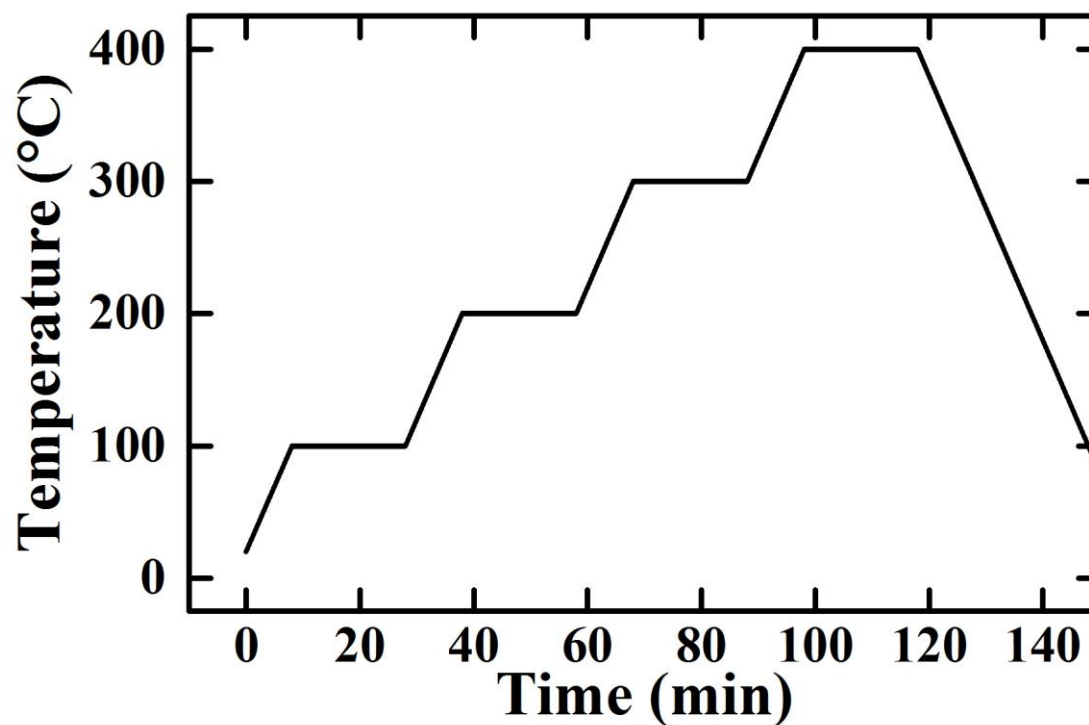


Figure 5.20: A sample temperature profile for an exploratory XRD diffusion measurement. XRD spectra were collected during the isothermal portions.

At each isothermal temperature, data was collected at angles from 2 degrees to 10 degrees 2θ for the low-angle peaks, and from 32.5 to 47.5 degrees 2θ for the Bragg peaks. The low angle data is shown in figure 5.21.

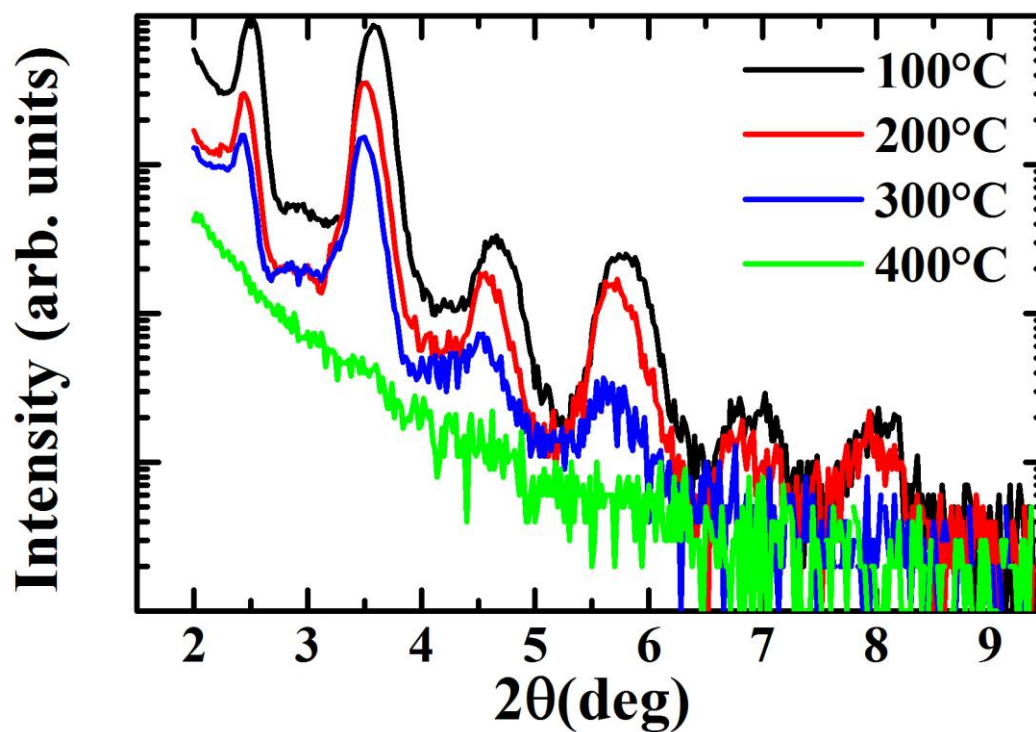


Figure 5.21: Low temperature XRD signals from the Pt-Ni multilayer system.

As mentioned in Chapter 2, these low angle signals were due to the large compositional periodicity of the multilayer. The decrease in the intensity of these peaks at temperatures as low as 200°C was evidence of diffusional mixing at that low temperature. This was compared to the measured (111) diffraction data (figure 5.22).

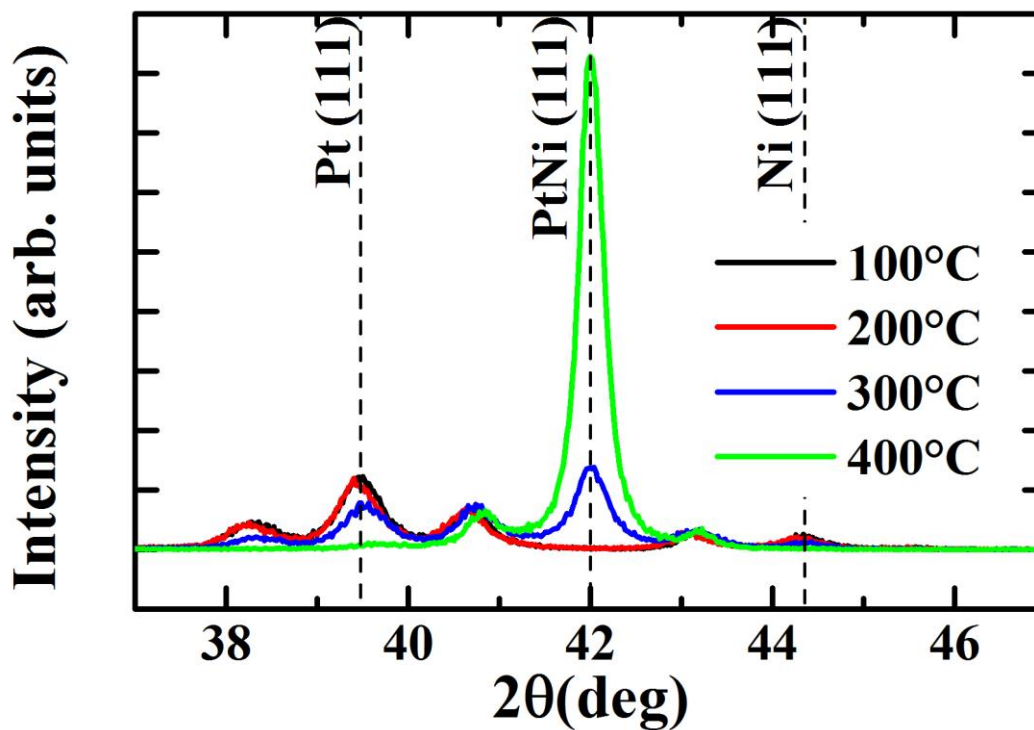


Figure 5.22: XRD signals from the Pt-Ni multilayer system around the Bragg peaks.

Changes in the Bragg peak spectrum occurred at higher temperatures. In this measurement, visible change began at approximately 300°C, although would likely have been visible at lower temperatures if a finer temperature scale had been used. Evidence of diffusion was seen at a much lower temperature in the low-angle XRD measurements, signifying a breakdown in the modulation of the multilayer structure. Sufficient diffusion to measure the Bragg peak of an alloy phase was not visible until much later.

Although exact characterizations of the amount of diffusion at a given temperature were difficult to make due to the complicated profile and the long collection time for each isotherm, measurements provided guidelines for the

temperatures required for Pt/Ni diffusion in this geometry. This system is still under examination by both pump-probe measurements and simulation.

Chapter 6

DIRECTIONS FOR CONTINUED WORK

There are a large number of obvious extensions to the work presented above, some of which have been explicitly stated in the text and some merely implied. What follows is an incomplete list of the most immediate and accessible extensions to the projects presented in this thesis.

First, the quantification of the activation energies in the reduction of Sm-Co-O to a Sm-Co metallic alloy remains unfinished. The technical limitations of the University of Delaware TGA systems do not currently allow measurement of the activation energy of the Sm₂O₃ to metallic Sm transition. An alternate measurement technique must be used to complete this research. In addition, full understanding of the activation energies of these reactions may allow renewed investigation into a one-step synthesis of nanoparticle Sm-Co hard magnetic alloys.

Several facets of the diffusion and sintering research also remain incomplete. As mentioned in chapter 5, research into the synthesis of core/shell Pt/Ni particles, as well as core/shell Ni/Pt is ongoing. Specifically, the synthesis of well-defined core/shell structures has still not been achieved. Experimentation with surfactants, alternate precursors, different sample environments or additional reducing agents may be required to synthesize isolated core/shell structures.

Similarly, research into the diffusion of the bimetallic Pt/Ni system is still in an early stage. There are a number of measurements still to perform on this system, such as a more careful examination of diffusion as a function of sintering temperature in a conventional setup as well as in a pump-probe style of experiment. In addition, simulation techniques are still under development to aid in the reconstruction of the

composition profile of a bimetallic multilayer from the XRD diffraction pattern. Once that technique is completed, a full description of two-dimensional diffusion in bimetallic multilayers should be achievable.

The bimetallic multilayer system also shows signs of strong stress effects, revealed by x-ray diffraction using an area detector. Preliminary multilayer diffusion measurements revealed significant variations between the in-plane crystalline lattice spacing and the out of plane spacing, which decreased upon diffusion. This signifies a breaking of the fcc symmetry of the Pt/Ni multilayer system, and should be quantifiable using the data already collected. A closer examination of this and related data may lead to a greater understanding of the effects of stress fields on diffusion in this family of systems.

Finally, each of these projects could naturally be extended to different materials. In particular, the motivation behind examining Pt nanoparticles applies equally to Au, Ag, Fe, Ni, and more. Each of these systems presents with unique synthesis and characterization challenges, but each would benefit from the increased understanding of the size-dependent properties of the materials.

REFERENCES

1. P. Alivisatos, *Nature Biotechnology* **22**, 47 (2004).
2. V. P. Torchilin, *European Journal of Pharmaceutical Sciences* **11**, S81 (2000).
3. H. T. Song, J. S. Choi, Y. M. Huh, S. Kim, Y. W. Jun, J. S. Suh, and J. Cheon, *Journal of the American Chemical Society* **127**, 9992 (2005).
4. B. Bonnemain, *Journal of Drug Targeting* **6**, 167 (1998).
5. U. I. Tromsdorf, N. C. Bigall, M. G. Kaul, O. T. Bruns, M. S. Nikolic, B. Mollwitz, R. A. Sperling, R. Reimer, H. Hohenberg, W. J. Parak, S. Forster, U. Beisiegel, G. Adam, and H. Weller, *Nano Letters* **7**, 2422 (2007).
6. P. K. Gupta, C. T. Hung, F. C. Lam, and D. G. Perrier, *International Journal of Pharmaceutics* **43**, 167 (1988).
7. E. Reddington, A. Sapienza, B. Gurau, R. Viswanathan, S. Sarangapani, E. S. Smotkin, and T. E. Mallouk, *Science* **280**, 1735 (1998).
8. C. Chappert, A. Fert, and F. N. Van Dau, *Nature Materials* **6**, 813 (2007).
9. C. Ross, *Annual Review of Materials Research* **31**, 203 (2001).
10. D. E. Speliotis, *Journal of Magnetism and Magnetic Materials* **193**, 29 (1999).
11. A. P. Alivisatos, *Science* **271**, 933 (1996).
12. S. H. Sun, C. B. Murray, D. Weller, L. Folks, and A. Moser, *Science* **287**, 1989 (2000).
13. R. Shenhar and V. M. Rotello, *Accounts of Chemical Research* **36**, 549 (2003).
14. D. J. Sellmyer, *Nature* **420**, 374 (2002).
15. J. T. Hu, T. W. Odom, and C. M. Lieber, *Accounts of Chemical Research* **32**, 435 (1999).
16. R. Narayanan and M. A. El-Sayed, *Nano Letters* **4**, 1343 (2004).

17. C. Burda, X. B. Chen, R. Narayanan, and M. A. El-Sayed, *Chemical Reviews* **105**, 1025 (2005).
18. M. P. Pileni, *Accounts of Chemical Research* **40**, 685 (2007).
19. R. Thiruvengadathan, V. Korampally, A. Ghosh, N. Chanda, K. Gangopadhyay, and S. Gangopadhyay, *Reports on Progress in Physics* **76** (2013).
20. C. B. Murray, C. R. Kagan, and M. G. Bawendi, *Annual Review of Materials Science* **30**, 545 (2000).
21. T. Hyeon, Y. Chung, J. Park, S. S. Lee, Y. W. Kim, and B. H. Park, *Journal of Physical Chemistry B* **106**, 6831 (2002).
22. T. Hyeon, *Chemical Communications*, **927** (2003).
23. S. H. Sun and C. B. Murray, *Journal of Applied Physics* **85**, 4325 (1999).
24. C. Petit, V. Russier, and M. P. Pileni, *Journal of Physical Chemistry B* **107**, 10333 (2003).
25. M. P. Pileni, *Journal of Physical Chemistry B* **105**, 3358 (2001).
26. V. Russier, C. Petit, J. Legrand, and M. P. Pileni, *Physical Review B* **62**, 3910 (2000).
27. J. M. D. Coey, *Journal of Magnetism and Magnetic Materials* **248**, 441 (2002).
28. R. Skomski and J. M. D. Coey, *Physical Review B* **48**, 15812 (1993).
29. K. J. Strnat and R. M. W. Strnat, *Journal of Magnetism and Magnetic Materials* **100**, 38 (1991).
30. C. B. Jiang and S. Z. An, *Rare Metals* **32**, 431 (2013).
31. A. M. Gabay, M. Marinescu, J. F. Liu, and G. C. Hadjipanayis, *Ieee Transactions on Magnetism* **44**, 4218 (2008).
32. W. F. Li, H. Sepehri-Amin, L. Y. Zheng, B. Z. Cui, A. M. Gabay, K. Hono, W. J. Huang, C. Ni, and G. C. Hadjipanayis, *Acta Materialia* **60**, 6685 (2012).

33. S. H. He, Y. Jing, and J. P. Wang, *Journal of Applied Physics* **113**, 4 (2013).
34. R. M. Liu, M. Yue, D. T. Zhang, W. Q. Liu, and J. X. Zhang, *Acta Metallurgica Sinica* **48**, 475 (2012).
35. S. A. Majetich, K. M. Chowdary, and E. M. Kirkpatrick, *Ieee Transactions on Magnetics* **34**, 985 (1998).
36. B. G. Kelly and K. M. Unruh, *Ieee Transactions on Magnetics* **49**, 3349 (2013).
37. T. Thomson, M. F. Toney, S. Raoux, S. L. Lee, S. Sun, C. B. Murray, and B. D. Terris, *Journal of Applied Physics* **96**, 1197 (2004).
38. N. T. Q. Hoa, V. D. Dao, and H. S. Choi, *Journal of Materials Science* **49**, 4973 (2014).
39. G. Wan and P. R. Sahn, *Acta Metallurgica Et Materialia* **38**, 2367.
40. J. A. Warren and B. T. Murray, *Modelling and Simulation in Materials Science and Engineering* **4**, 215 (1996).
41. M. A. Asoro, D. Kovar, Y. Shao-Horn, L. F. Allard, and P. J. Ferreira, *Nanotechnology* **21**, 6 (2010).
42. D. D. Beck and C. J. Carr, *Journal of Catalysis* **110**, 285 (1988).
43. Z. Z. Fang and H. Wang, *International Materials Reviews* **53**, 326 (2008).
44. J. Matos, L. K. Ono, F. Behafarid, J. R. Croy, S. Mostafa, A. T. DeLaRiva, A. K. Datye, A. I. Frenkel, and B. R. Cuenya, *Physical Chemistry Chemical Physics* **14**, 11457 (2012).
45. S. B. Simonsen, I. Chorkendorff, S. Dahl, M. Skoglundh, J. Sehested, and S. Helveg, *Journal of the American Chemical Society* **132**, 7968 (2010).
46. F. Behafarid and B. R. Cuenya, *Surface Science* **606**, 908 (2012).
47. F. Behafarid and B. R. Cuenya, *Topics in Catalysis* **56**, 1542 (2013).
48. C. G. Granqvist and R. A. Buhrman, *Journal of Catalysis* **42**, 477 (1976).

49. A. K. Datye, Q. Xu, K. C. Kharas, and J. M. McCarty, *Catalysis Today* **111**, 59 (2006).
50. T. W. Hansen, A. T. Delariva, S. R. Challa, and A. K. Datye, *Accounts of Chemical Research* **46**, 1720 (2013).
51. G. K. Rane, U. Welzel, and E. J. Mittemeijer, *Acta Materialia* **60**, 7011 (2012).
52. S. C. Parker and C. T. Campbell, *Topics in Catalysis* **44**, 3 (2007).
53. Reif, F., *Fundamentals of Statistical and Thermal Physics*. (McGraw Hill, New York, 1965) p. 483.
54. C. Solliard and M. Flueli, *Sur. Sci.* **156**, 487 (1985).
55. R. Dingreville, J. Qu, and M. Cherkaoui, *J. Mech. Phys. Solids* **53**, 1927 (2005).
56. Z. Huang, P. Thomson, and S. Di, *J. Phys. Chem. Solids* **68**, 530 (2007).
57. W.G. Wolfer, *Acta Mater.* **59**, 7736 (2011).
58. R. Birringer and P. Zimmer, *Acta Mater.* **57**, 1703 (2009).
59. G. K. Rane, U. Welzel, S. R. Meka, and E. J. Mittemeijer, *Acta Materialia* **61**, 4524 (2013).
60. J. Sheng, C. Rane, U. Welzel, and E. J. Mittemeijer, *Physica E-Low-Dimensional Systems & Nanostructures* **43**, 1155 (2011).
61. A. L. Greer and F. Spaepen, *Synthetic Modulated Structures*, ed. L. L. Chang and B. C. Giessen (Academic Press, Florida, 1985) p. 419.
62. N. C. Bigall, T. Hartling, M. Klose, P. Simon, L. M. Eng, and A. Eychemuller, *Nano Letters* **8**, 4588 (2008).
63. E. Bellido, N. Domingo, I. Ojea-Jimenez, and D. Ruiz-Molina, *Small* **8**, 1465 (2012).
64. T. P. Bigioni, X. M. Lin, T. T. Nguyen, E. I. Corwin, T. A. Witten, and H. M. Jaeger, *Nature Materials* **5**, 265 (2006).

65. K. Chokprasombat, C. Sirisathitkul, and P. Ratphonsan, *Surface Science* **621**, 162 (2014).
66. B. Mukherjee and N. Ravishankar, *Nanotechnology* **18**, 9 (2007).
67. F. Reincke, S. G. Hickey, W. K. Kegel, and D. Vanmaekelbergh, *Angewandte Chemie-International Edition* **43**, 458 (2004).
68. L. F. Hu, M. Chen, X. S. Fang, and L. M. Wu, *Chemical Society Reviews* **41**, 1350 (2012).
69. C. Liu, Y. J. Li, M. H. Wang, Y. He, and E. S. Yeung, *Nanotechnology* **20**, 6 (2009).
70. Y. K. Park and S. Park, *Chemistry of Materials* **20**, 2388 (2008).
71. D. P. Macwan, P. N. Dave, and S. Chaturvedi, *Journal of Materials Science* **46**, 3669 (2011).
72. H. Chander, *Materials Science & Engineering R-Reports* **49**, 113 (2005).
73. I. Ali, M. U. Islam, M. S. Awan, and M. Ahmad, *Journal of Materials Engineering and Performance* **22**, 2104 (2013).
74. J. A. Bustnes, D. U. Sichen, and S. Seetharaman, *Metallurgical and Materials Transactions B-Process Metallurgy and Materials Processing Science* **26**, 547 (1995).
75. H. M. Trimble and W. Potts, *Industrial and Engineering Chemistry* **27**, 66 (1935).
76. *Pearson's Handbook of Crystallographic Data for Intermetallic Phases*, ed. P. Villars and L.D. Calvert (American Society for Metals, Metals Park, OH).
77. K. Du, F. Emst, M. C. Pelsozy, J. Barthel, and K. Tillmann, *Acta Materialia* **58**, 836 (2010).
78. J. R. Gallagher, T. Li, H. Y. Zhao, J. J. Liu, Y. Lei, X. Y. Zhang, Y. Ren, J. W. Elam, R. J. Meyer, R. E. Winans, and J. T. Miller, *Catalysis Science & Technology* **4**, 3053 (2014).
79. H. J. Wasserman and J. S. Vermaak, *Surface Science* **32**, 168 (1972).

80. I. N. Leontyev, A. B. Kuriganova, N. G. Leontyev, L. Hennem, A. Rakhmatullin, N. V. Smirnova, and V. Dmitriev, *Rsc Advances* **4**, 35959 (2014).
81. C. Solliard and M. Flueli, *Surface Science* **156**, 487 (1985).
82. S. M. Collard and R. B. McLellan, *Acta Metallurgica Et Materialia* **40**, 699 (1992).
83. W. H. Qi, B. Y. Huang, M. P. Wang, Z. M. Yin, and J. Li, *Journal of Nanoparticle Research* **11**, 575 (2009).
84. J. W. M. Jacobs and D. Schryvers, *Journal of Catalysis* **103**, 436 (1987).